# WETTING BEHAVIOUR OF ALUMINUM ALLOYS ON CERAMIC SUBSTRATES AND ITS EFFECT ON THE STABILITY OF ALUMINUM FOAMS

– THESIS –

Submitted by Dipl.-Ing. Andreas Klinter (McGill ID: 260 196 502)

to the Department of Mining, and Materials Engineering at

McGill

McGill University, Montréal (Canada)

on December 8th, 2009

in partial fulfillment of the requirements of the degree of Doctor of Philosophy

# ABSTRACT

Early empirical publications on metal foam production have shown that ceramic particles are required in the alloy in order to produce stable aluminum foams. Following a commonly accepted theory, it is believed that the wetting behaviour of the alloy on the particles is the main factor causing the stabilizing effect of the particles. The connection between wetting and metal foamability, however, has not yet been proven. The present work is a systematic study of the wetting behaviour of synthetic aluminum alloys on ceramic substrates under high vacuum conditions rounded off by foaming tests with several of these alloy / ceramic particle systems.

The wetting experiments were conducted in a horizontal tube furnace, which allows for high precision contact angle measurements; foaming tests were carried out in an expandometer. From the wetting behaviour and accompanying foam expansion and quality results, the common foam stabilization theory was evaluated.

Based on analyses of wetting experiments, it was found that certain alloying elements can reduce the contact angle of aluminum on $Al_2O_3$ and SiC, and that even wetting systems that are commonly considered non-reactive are in fact highly affected by chemical reactions occurring at the interface.

The foaming results showed that while it appears that the stabilization theory linking wetting behaviour and foam quality is generally correct, wetting experiments under idealized (almost oxygen-free) conditions are unsuitable to predict foam stability based on these models, as in-situ wetting behaviour during foaming seems to be significantly different from that observed during the wetting experiments.



# RÉSUMÉ

Les premières publications empiriques portant sur la production de mousses métalliques montrent que la présence de particules de céramique dans la composition d'un alliage est nécessaire afin d'assurer la production de mousses d'aluminium stables. Selon une théorie communément acceptée, il est établi que le facteur à l'origine de l'effet de stabilisation apporté par les particules provient du comportement au mouillage de l'alliage sur les particules. Cependant, aucune connexion entre les caractéristiques de mouillage et de moussabilité du métal n'a encore été établie. Le présent ouvrage propose une investigation systématique sur les comportements au mouillage d'alliages synthétiques d'aluminium sur des substrats de céramique et dans des conditions de vide poussé, corroborée par des essais de moussage avec plusieurs de ces systèmes alliage/particules.

Les expériences de mouillage ont été réalisées dans un four à tube horizontal permettant des mesures d'angle de contact de haute précision; les tests de moussage ont été effectués dans un expandomètre. La corrélation entre le comportement au mouillage des alliages et les résultats d'expansion et de qualité des mousses correspondantes a permis d'évaluer la théorie de stabilisation des mousses métalliques.

A partir des analyses effectuées sur les expériences de mouillage, il a été montré d'une part que la présence de certains éléments dans la composition de l'alliage peut engendrer une réduction de l'angle de contact de l'alliage d'aluminium sur des substrats de céramiques tels que $Al_2O_3$ et SiC; d'autre part, il a été défini que les systèmes de mouillage, bien que généralement considérés inertes, se trouvaient en

réalité amplement affectés par l'incidence de réactions chimiques au niveau de l'interface alliage/céramique.

Si les résultats des expériences de moussabilité ont montré de façon générale une bonne corrélation avec la théorie de stabilisation des mousses qui relie le comportement au mouillage de l'alliage et la qualité de la mousse, en revanche les résultats des expériences de mouillage dans des conditions idéales (sous atmosphère très pauvre en oxygène) n'ont pas suivi les prédictions de stabilité des mousses établies par les modèles théoriques. En effet, le comportement au mouillage in-situ de l'alliage, au cours de la formation de la mousse, semble différer de façon significative du comportement observé au cours des expériences de mouillage.



# ACKNOWLEDGMENTS

For financing this research project, I would like to thank General Motors of Canada, the Fond de Recherche sur la Nature et les Technologies Québec (FQRNT), and the Natural Sciences and Engineering Research Council of Canada (NSERC). I would like to give special thanks to the Antje Graupe Pryor Foundation and the FQRNT for awarding me the Werner Graupe International Fellowship and the Quebec Merit Scholarship for Foreign Students, respectively, and only thereby making my studies at McGill University possible. Furthermore, the McGill Principal's Graduate Fellowship as well as the McGill International Doctoral Award are highly appreciated.

Sincere thanks to Prof. Robin A.L. Drew for offering me this challenging topic as well as to Prof. Carlos A. Leon (Instituto de Investigaciones Metalurgicas, Universidad Michoacana) and Dr. Guillermo Mendoza-Suarez for helpful support, hints and suggestions. I would like to acknowledge the resourceful advice and help of Prof. In-Ho Jung with thermodynamic modelling, and the patient training at the SEM by Helen Campbell and at the AFM by Lang Shi, as well as the help of Dr. Jean-Philippe Massé (École Polytechnique), and Camille Probst with TEM work. My thanks go to Suzie Poulin (École Polytechnique) for help with XPS analyses, to Monique Riendeau and Ranjan Roy with chemical analyses, to Pierre Vermette with alloy casting, Sheryl Mercier (IMI-NRC) with oxygen analyzes and particularly to Barbara Hanley for advice and help with all organizational things throughout my time at McGill. I lastly but certainly not least would like to express my deep appreciation for the helping hands, suggestions, fruitful discussions, and friendship of my group members and / or colleagues Pantcho P. Stoyanov, Cécile Charbonneau, Paula M. Proa-Flores, Dr.

Phuong Vo, Raymond Langlois, Renaud Daenzer, Umugaba Seminari, Prof. Mathieu Brochu, Ryan Cunningham, Patrick Blonde, Rebecca Payant, Lydia J. Aguirre-Perales, Ramona R. Vintila, Mert Celikin, Sean Cadney, and Dr. Dominique Poirier.



# TABLE OF CONTENTS

# TABLE OF FIGURES

# TABLE OF TABLES

# 1 INTRODUCTION

Over almost two decades, cellular metals and metal foams have enjoyed thriving popularity due to their very interesting set of properties, combining high stiffness with very low specific weight, good impact absorption and acoustic insulation; thermal conductivity or good thermal insulation is attainable depending on the foam structure. Open porous cellular metals have proved to be advantageous as catalyst substrates due to their large internal surface area, and the ease with which active surfaces can be applied. Aluminum is currently the most important metal in foam manufacture due to its low bulk density of 2.7 $^{g}/_{cm^3}$, its foamability, and low cost.[1]

Over the last few years, metal foams have been through a significant quality improvement, mainly due to new fabrication processes; nevertheless, non-uniformity and foam collapse remain important issues that need to be addressed before a larger scale industrial use of these materials is feasible.[2] The exact factors, however, which promote or mitigate foam stability and thereby foam quality are not yet clarified.[3]

It seems that in order to improve foam quality, it is important to understand the wetting behaviour of aluminum melts on ceramic particles, as this appears to play a role in foam stabilization.[4-12] Unfortunately, most data presented in literature[13-17] refers to measurements of the contact angle of aluminum surrounded by an oxide layer. The obtained values are consequently of limited significance as the oxide layer drastically alters the wetting behaviour of aluminum.[4]



The objective of this project was to investigate, without an interfering oxide layer, the wetting behaviour of aluminum, and several of its alloys on alumina, sapphire, and silicon carbide substrates under high vacuum and at varying temperatures. The obtained information about the wetting behaviour of the different systems was then correlated to expansion curves and pore morphology results obtained during foaming. This allows for an evaluation of stabilization mechanisms proposed and discussed in literature.[2,4-6,8,10,18] The investigation focused on aluminum alloys containing silicon, magnesium, copper and combinations thereof.

# 2 LITERATURE REVIEW

## 2.1 METAL FOAMS – CELLULAR MATERIALS

The term *foam* for a group of materials, even though commonly used, might be misleading. In materials sciences and engineering, it describes a material containing a gas phase in a very significant volume fraction dispersed in a solid phase, despite the original meaning of *foam* describing a gaseous phase entrapped in a liquid. Hence, terms like 'cellular materials' or 'solid foams' would be more suitable; however, following common terminology[1], in the present thesis, the term *foam* is expanded in meaning to cover solid cellular materials.

### 2.1.1 Production Methods of Metal Foams

Today, a variety of production processes for metal foams have been developed. Some are similar to techniques used for foaming polymers or aqueous solutions, whilst others are uniquely designed to produce metal foams.

According to the state the metal is processed in, four families of production-processes can be distinguished: melt processes, powdered metal processes, vapour deposition processes, and metal ion deposition processes. *BANHART*[1] provides a complete compilation of the various techniques.

### 2.1.1.1 Liquid Metal Foaming

Liquid metal foaming, as a very important approach to foaming metals, involves melting the metal or alloy. The most important liquid state foam production method used in larger scale industrial production is the direct foaming method, currently employed by *CYMAT CORPORATION* (Canada)[a]; hence, this process is often referred to as the *CYMAT*-process. It has been shown to be one of the most economically feasible processes as it is possible to semi-continuously produce large quantities of aluminum foam of reasonable quality at comparatively low cost.

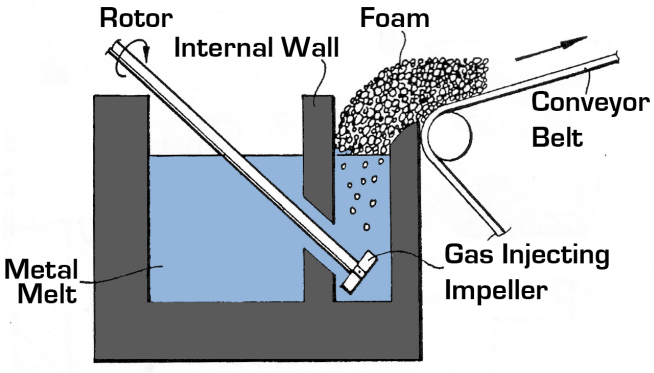


Figure 2.1: Direct foaming of metal melts by gas injection

In the first step of the direct foaming process, ceramic particles such as alumina or silicon carbide are added into the aluminum melt (typically 5 to 15vol.%[19,20]). In the case of *CYMAT*, metal matrix composite (MMC) material is purchased from *RIOTINTO ALCAN* (Australia / Canada), which leaves this first step being outsourced. In the second step, depicted in Figure 2.1[20], the liquid metal is foamed by injecting gases such as air, nitrogen, or argon through an impeller in order to create fine and uniformly distributed gas bubbles in the melt. The bubbles float to the surface of the melt where excess liquid from the films between the bubbles drains out. A conveyor belt pulls the reasonably dry foam off the surface of the melt, thereby allowing a

[a] In 2001, *CYMAT* acquired the metal foam division of *HYDRO ALUMINIUM* (Norway), which was *CYMAT*'s only serious competitor in the aluminum foam market and employed a very similar liquid foaming process.

semi-continuous production process; on the belt, the foam cools and solidifies.[1,20] (Figure 2.2[21])

Like in metal matrix composites, the ceramic particles are added to the aluminum melt to control its viscosity. It has been found empirically that the ceramic particles also have a stabilizing effect on the foam. Also like in MMC production, difficulties arise with homogeneously distributing the particles in the melt as they tend to coagulate, to float to the melt surface or to settle.[1,4,5,19,20,22]

Figure 2.2: *CYMAT* foam sample

A modification of this direct foaming process has been suggested by mixing solid particles of a suitable blowing agent (such as metal hydrides[23] or elemental calcium[24]) into the melt instead of blowing gas into it. Under the influence of the heat, the blowing agent decomposes and releases a gas, propelling the foaming process. However, difficulties with inhomogeneous distribution of not only the ceramic particles but also the blowing agent in the melt make this a rarely used process.[1]

#### 2.1.1.2 Powdered Metal Foaming

A group of processes similar to the production of ceramic materials employs powdered metal as starting material. In one variation, gas is deliberately entrapped while consolidating the metal powder into a green compact. A subsequent heat-treatment at a temperature below the melting point of the metal leads to sintering of the metal powder, during which the entrapped gas expands; a foamed sinter metal product forms. Such foams typically have closed porosity with relatively thick cell walls and

high density, as the entrapped gas tends to escape through cracks in the compact during heating.

Alternative methods include mixing the metal powder with polymeric space holder particles or wood chips prior to compaction. The subsequent sintering process causes disintegration of the space holders, leaving voids in the matrix. These processes also result in foams with rather thick cell walls and comparably low, but uniform, and very controllable porosity.[1]

As the uniformity of foams produced via the *CYMAT*-process or the gas-entrapment method is problematic, and since it is advantageous to produce near net-shape foams in order to avoid machining, recent efforts have concentrated on the improvement of the powder metallurgical fabrication process (PM technique); Figure 2.3 (after *BANHART*[1]) depicts a flow chart of the process. In this method, the starting materials are a metal powder and a blowing agent (and in some cases ceramic particles) which are mixed and consolidated to a foamable green compact with close to theoretical density. This leaves the blowing agent embedded in a gas-tight metal matrix. Subsequent heat-treatment of these precursors, around or little above the melting temperature of the matrix metal causes the blowing agent to decompose and

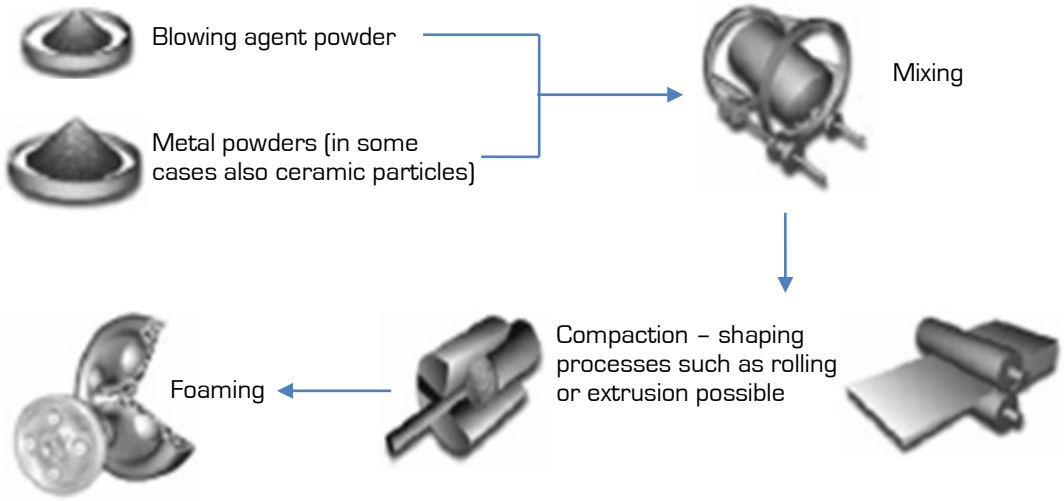


Figure 2.3: Process flow chart of the powder metallurgy method of metal foam production

release gas (usually hydrogen). The gas forces the compacted and at least partially molten precursor to expand and develop into a foam with a closed cell morphology.[1,25] Currently, much research is being undertaken to improve the gas-releasing properties of blowing agents.[26]

Figure 2.4: Steel profile filled with aluminum foam made via the PM method

For this process, aluminum cast alloys such as Al-7Si-Mg, Al-12Si, and Al-6Si-Cu are frequently used, since their low melting point is close to the decomposition temperatures of common blowing agents such as $TiH_2$, $ZrH_2$, and $HfH_2$.[25] Other matrix metals are pure aluminum and wrought aluminum alloys such as the 2xxx or the 6xxx series.[27]

#### 2.1.1.3 Foam Formation by Vapour Deposition

Metal foams can also be manufactured from a metal vapour, or a gas phase containing metallic compounds. For this, an open porous solid precursor is required that defines the geometry of the cellular material to be produced. In general, polymeric cellular structures are used for this purpose. Employing standard chemical or physical vapour deposition techniques, a coating of the desired metal is deposited on the surface of the precursor, forming a negative replica of its structure. Once a sufficient coating thickness is achieved, the polymer precursor is removed by a thermal or chemical treatment,

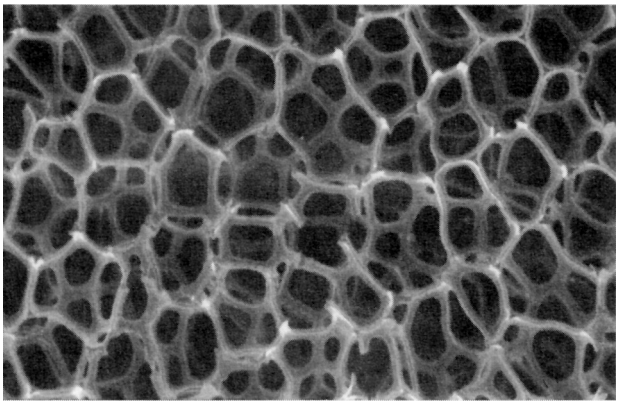

Figure 2.5: Nickel cellular material, manufactured using an open porous polymeric precursor and chemical vapour deposition



leaving behind a web-like structure of hollow struts. A nickel foam produced using chemical vapour deposition is depicted in Figure 2.5[1].

#### 2.1.1.4 Foam Formation by Electrochemical Deposition

Electrochemical deposition of metal ions is a method of production of cellular metallic materials similar to the vapour deposition method, resulting in open porosity. A conductive precursor foam with open porosity (usually a polymer) is inserted into an electrolyte containing ions of the desired metal or metals and charged with a negative bias. This causes the metal ions to deposit on the precursor surface. After a sufficient coating thickness is achieved, the polymer is chemically or thermally removed, and a framework of hollow struts of the metal remains.[1]

Vapour and electrochemical deposition foams usually have extremely low densities. However, they tend to be characterized by issues with non-uniform metal deposition thickness and comparatively high production costs as these processes are slow.

### 2.1.2 Properties of Metal Foams

Cellular metals and metal foams enjoy thriving popularity due to their unique combination of properties. Their characteristics are best summarized by describing the metal the foam is made of, stating whether it has closed or open porosity, and by its relative density

$$\rho/\rho_s, \qquad \text{Eq. 2.1}$$

where $\rho$ is the foam density and $\rho_s$ is the density of the solid metal the cell walls consist of.[28]

### 2.1.2.1 Mechanical Properties

The mechanical properties of metal foams depend on those of the bulk metal; however, they still span a wide range depending on the foam morphology. It is important to understand that foams do not behave as homogeneously as solid metals. The largely variable cell size and shape, as well as the cell wall thickness have significant effects on the mechanical behaviour. This is one of the attractive aspects of foam materials, since it allows the mechanical behaviour to be tailor to a desired properties profile; however, if they remain uncontrolled, the resulting properties are variable and therefore problematic. Moreover, morphological defects such as missing cell walls are the reason why commercially available metal foams do not achieve the theoretically predicted mechanical properties.[28,29]

The stress-strain behaviour of a metal foam differs from that of a solid material as depicted in Figure 2.6[28]. Initial loading appears to be elastic, however the initial loading curve is commonly not straight, and its slope is often less than the true modulus since some cells yield at very low loads. The real *YOUNG*'s modulus is best determined by loading the foam into the plastic range, then unloading it and measuring the unloading slope. Once the stress is sufficiently high to cause all cells to yield, the stress does not rise until the foam is densified and starts to behave like the bulk metal, causing the stress-strain curve to rise steeply.

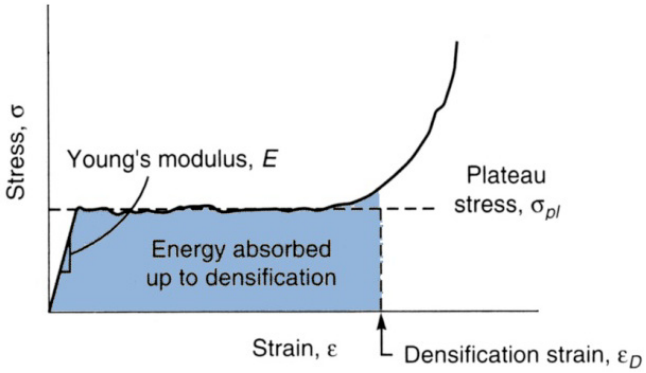


Figure 2.6: Schematic stress-strain curve of metal foams

The theoretical mechanical properties such as the *YOUNG*'s modulus $E$, the shear modulus $G$, or *POISSON*'s ratio $\nu$ of metal foams are determined by scaling the properties of the solid metal by the density ratio:[28]



$$E \approx \alpha \cdot E_s \left(\frac{\rho}{\rho_s}\right)^n \quad \text{Eq. 2.2}$$

$$G \approx \frac{3}{8}\alpha \cdot G_s \left(\frac{\rho}{\rho_s}\right)^n \quad \text{Eq. 2.3}$$

$$\nu \approx 0.3 \quad \text{Eq. 2.4}$$

where $n$ and $\alpha$ are constants with values between 1.8 and 2.2, and 0.1 and 4, respectively, depending on the structure of the foam. It is important to know that the compressive modulus $E$ and the tensile modulus $E_t$ are not equal; the tensile modulus is typically 10% greater. This is because the stress-strain behaviour of a foam under tension differs from that under compression: in tension the slope of the stress-strain curve before general yield is less than $E$, implying noticeable microplasticity, even at very small strains. Beyond yield, metal foams harden up to the ultimate tensile strength, after which they fail typically in a brittle manner.[28,30]

In shear loading, metallic cellular materials usually behave brittle. Cracks initiate at the core of the specimen and propagate parallel to the load axis through the sample length. Foams subjected to torsion experience the typical spiral fracture observed with solid samples.[28,30]

Finite element analyses have shown that the notch sensitivity of metal foams is low and that holes, cracks, or diameter changes do not noticeably affect their tensile strength properties.[31] Hence, foam-based structures are more damage tolerant and the failure behaviour is less catastrophic than that of a solid metal.[1]

Another particularly interesting property related to the mechanical behaviour under compression is the enormous energy dissipation capacity of metal foams (compare Figure 2.6). The compressive deformation of metallic cellular materials is not a purely ductile process; fracture takes place very early in bands horizontal to the applied load. Foam crushing proceeds through formation, multiplication, and propagation of

strain bands localized throughout the specimen, which results in high energy absorption during non-elastic deformation.[30]

Moreover, the elastic rebound after the load is taken off a plastically deformed metal foam is significantly smaller than what is observed from polymer foams, for instance in helmets.[28] The latter can prevent brain injuries by absorbing the impact energy; however, they tend to cause neck injuries due to the elastic rebound of the polymer foam immediately after the impact.

#### 2.1.2.2 Thermal and Electrical Properties

The melting point of metal foams is the same as that of the metal they are made of. The specific heat is a function of both the metal and the entrapped gas phase; the thermal expansion coefficient depends largely on the structure of the foam. The thermal conductivity of foamed metals is reduced in comparison to that of the corresponding solid metal and is similar to the mechanical properties scaled by the density ratio:[28]

$$\lambda \approx \lambda_s \left(\frac{\rho}{\rho_s}\right)^q \qquad \text{Eq. 2.5}$$

with $q$ being a constant varying between 1.65 and 1.8 depending on the foam morphology.[28]

In close relation to the *Wiedeman-Franz*-law[32], relating electrical and thermal conductivities in metals, the electrical properties of metal foams behave similarly to the thermal properties; the electrical resistivity of a metallic foam again scales with the density ratio:[28]

$$R \approx R_s \left(\frac{\rho}{\rho_s}\right)^{-r} \qquad \text{Eq. 2.6}$$



with $r$ being a parameter varying between 1 and 1.85 depending on the foam morphology.[28]

#### 2.1.2.3 Sound Absorption and Vibration Suppression

The sound absorption capacity of metal foams is not as good as that of materials designed specifically for sound absorption, such as glass wool; however, metal foams can reach sound absorption coefficients of up to 99% at certain frequencies. The sound absorption strongly depends on the foam morphology, and is usually better in open porous foams than in foams with closed porosity. This can be understood, considering the reflection, absorption, and transmission of sound waves at interfaces. It is obvious that a sound wave that strikes a cell wall perpendicularly will be mostly reflected, whereas a wave that strikes the cell wall of an open porous foam at an acute angle transfers most of its energy into the cell wall. The wave amplitude in the cell walls is reduced with increasing distance traveled in the foam, due to destructive interference of the surface waves and damping due to mechanical hysteresis.[28,33]

This mechanical hysteresis is also the reason for the mechanical damping of cellular materials and the consequent suppression of vibration; the energy loss factor of foams is approximately 10 times higher than that of the solid metal. The resonance frequency of a metal foam structure is, in general, shifted towards lower frequencies in comparison to a conventional structure, since the *YOUNG*'s modulus and the density of metal foam are lower than that of the solid metal.[28,34,35]

### 2.1.3 Applications

The suitability of a metal foam for a given application is determined by the property profile needed. Among the most important considerations involved in materials selection are physical properties, porosity (type, amount, size, total internal surface area), possibilities for shaping the foam or for manufacturing composites of foam and

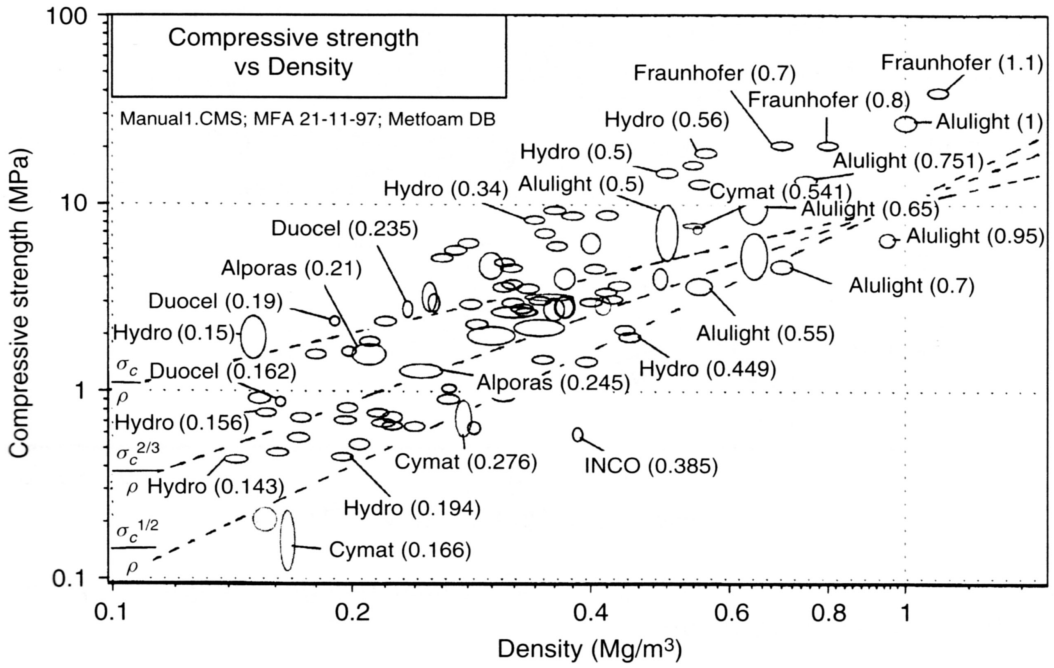


Figure 2.7: Material property chart of compressive strength vs. density. The value in parentheses is the density ratio (of foam and solid material)

conventional sheets or profiles, cost issues like suitability for large volume production, and metallurgical considerations (if age-hardening is required). Material property charts such as the one depicted in Figure 2.7[28] for various foams, are typically involved in this material selection process.

In general, structural applications require closed cell foams, while open porosities are more advantageous for functional applications.

#### 2.1.3.1 Automotive Applications – Lightweight Construction

Light-stiff constructions to lower fuel consumption without compromising safety are an important issue among others in the automotive industry. Aluminum foams combine both advantages: they possess low density with a high stiffness to weight ratio, and are capable of absorbing large quantities of energy even at high strain rates. This makes them particularly interesting for car crash boxes to improve the safety of passengers in the event of an accident. The additional advantages of sound absorp-



tion and vibration suppression create possibilities for making vehicles more comfortable by employing metallic foam materials. Hence, aluminum foams offer promising solutions to overcome a variety of current challenges in the automotive industry.[28,33,36,37]

In order to solve problems with joining metal foams, car manufacturers such as *KARMANN* (Germany)[1,38] or *RENAULT* (France)[39] are experimenting with aluminum foam sandwich structures for crash boxes, for instance, as they outperform conventional honeycomb panels; *BMW* (Germany) has presented prototypes of aluminum foam filled engine mounting brackets (Figure 2.8[36]). Furthermore, aluminum foams appear to have potential for the introduction of new construction principles for the vehicle, reducing the number of components needed in the car and thereby decreasing fabrication costs.[40]

Figure 2.8: *BMW* engine mounting bracket prototype, before aluminum foam filling (left), after foam filling (middle) and sectioned (right)

#### 2.1.3.2 Aerospace Industry

The lightweight construction requirements in the aerospace industry are similar if not more stringent to those in the automotive industry. *BOEING* (USA), for instance, has evaluated the use of titanium and aluminum foam sandwich parts for the tail booms of helicopters. In this context it could be advantageous that it is easier to produce metal foam sandwich panels with curvature and 3D shape than it is to manufacture honeycomb components with such geometry.[1]

Other possible applications include structural parts in turbines, where the enhanced stiffness in conjunction with increased damping is advantageous. In space technol-

ogy, aluminum foams have been evaluated for their use as energy absorbing crash elements in space vehicle landing pads.[1]

#### 2.1.3.3 Machine Construction

In stationary drilling, milling, or printing machines, stiff foamed parts or foam-filled columns with reduced inertia and improved damping capabilities could replace axles, rolls, or platforms currently made from conventional solid materials. [1]

Structural applications in the ship building or railway industries, the construction industry, and in sports and biomedical equipment have been evaluated.[1] Functional applications for open porous metal foams include filtration and separation units, as well as heat exchangers, and cooling machines. Furthermore, it is likely that metal foams prevail as support for catalysts, as lubricant storing bearing supports, fluid flow controls, dampers, silencers, or battery electrodes.[1]

Over the past few years, particularly *CYMAT* has incurred research in the potential application of metal foams in the field of blast mitigation, again exploiting the low density as well as the impact absorption capacity of these materials. The company's strongest commercial products currently are architectural facade panels from aluminum foams.[41]

## 2.2 PHYSICS OF INTERFACES

Interfaces and the physics which characterize them, have significant influence on a wide range of engineering areas, such as semiconductor science, thin film technology, tribology and coatings, microscopy, biology, electrochemistry, corrosion, and wetting.[42-45] When considering the latter, it is very important to understand that

wetting is not a material property of the liquid or the solid, but is characteristic of a system consisting of the liquid, the substrate (independent of whether it is liquid or solid) and the vapour phase surrounding the two (if present).

### 2.2.1 Non-Reactive Wetting

Non-reactive wetting, the simplest case of wetting, refers to the study of how a liquid that has been deposited on a substrate spreads out without chemical inter-actions taking place between the liquid and the substrate. A common method of classification between different types of wetting behaviour is the differentiation into total and partial wetting. The parameter that differentiates the two is the spreading parameter $S$; a metric of the difference in surface energy per unit area of the dry and the wet substrate:[46]

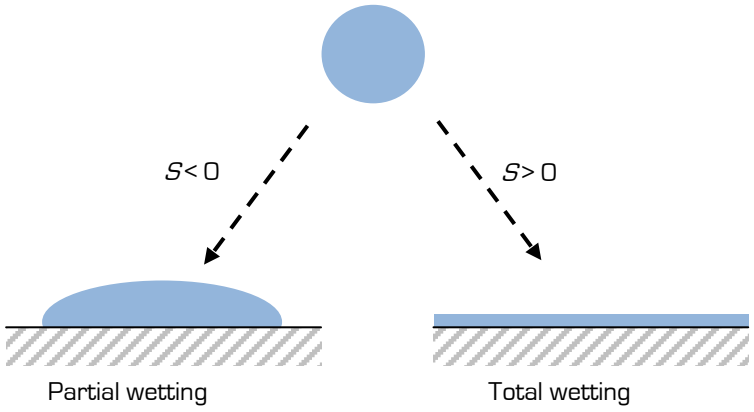


Figure 2.9: A sessile drop on a surface in the two wetting regimes of partial and total wetting

$$S = E^{\text{dry}}_{\text{Substrate}} - E^{\text{wet}}_{\text{Substrate}} \qquad \text{Eq. 2.7}$$

This can be rewritten in the more common form:

$$S = \sigma_{\text{SV}} - (\sigma_{\text{SL}} + \sigma_{\text{LV}}) \qquad \text{Eq. 2.8}$$

The surface energies of the solid-vapour, the solid-liquid, and the liquid-vapour interfaces are represented by $\sigma_{\text{SV}}$, $\sigma_{\text{SL}}$, and $\sigma_{\text{LV}}$, respectively. If $S$ is positive, the liquid has strong affinity to the solid and readily spreads out over the solid in order to lower its surface energy. This is referred to as total wetting. In the case of partial wetting, the affinity between liquid and solid is low and the liquid does not readily spread out

upon contacting the solid. Instead, the drop of liquid forms a spherical cap, once equilibrium is reached (Figure 2.9[46]).

The contact angle $\theta$ is defined as the angle enclosed by the vectors of the surface tension of the solid-liquid interface, $\gamma_{SL}$, and that of the liquid-vapour surface, $\gamma_{LV}$. It equals 0° for total wetting and is less than 180° for partial wetting.[b] The case of $\theta = 180°$ is referred to as non-wetting.[46]

The *YOUNG-DUPRÉ* equation results from tallying up the three surface tensions acting at the line of contact between substrate, liquid and the surrounding vapour (as shown in Figure 2.10), and equating the sum to zero:[47]

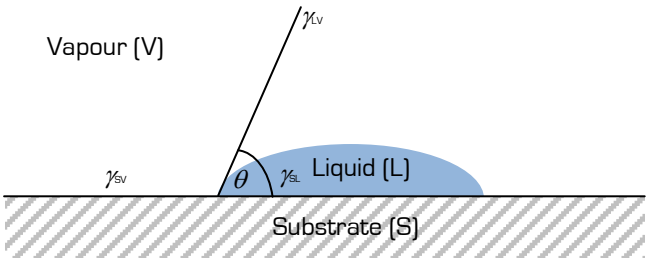

Figure 2.10: Contact angle in a sessile drop experiment

$$\gamma_{LV} \cdot \cos\theta = \gamma_{SV} - \gamma_{SL} \qquad \text{Eq. 2.9}$$

From Equations 2.8 and 2.9, it follows that the contact angle $\theta$ is only defined if the spreading parameter $S$ is negative. The contact angle $\theta$ is the most commonly used metric of wetting behaviour, as it is easy to measure and is as representative for the wetting behaviour as the spreading parameter $S$ itself.

[b] Other references differentiate wetting behaviour in four categories rather than two: total wetting for $\theta = 0°$, partial wetting for $0° < \theta \leq 90°$, partial non-wetting for $90° < \theta \leq 180°$, and total non-wetting for $\theta = 180°$. It can be understood that total wetting and total non-wetting are boundary conditions that are only of theoretical meaning.



### 2.2.2 Reactive Wetting

The case where the liquid not only wets the substrate in the above described purely physically manner but also chemically interacts with it is referred to as reactive wetting. A chemical agent in the liquid or the liquid itself attacks the substrate's surface or attaches itself to it, which alters the interface and causes either increasing or decreasing wettability over time.[46]

### 2.2.3 Wetting at Elevated Temperatures

As the wetting behaviour of liquid metals on ceramics strongly influences various processes like the production of metal-ceramic composites or the mechanical performance of metal-ceramic joints, it has attracted considerable research interest over many years.[48-52] However, wetting experiments at elevated temperatures are somewhat more difficult to control than at room temperature, as the surface properties of nearly all metals and many ceramics at high temperatures are very sensitive to impurities contained in the furnace atmosphere (mainly oxygen). Moreover, many liquid-solid couples are far from chemical equilibrium and the resulting interfacial reactions can strongly alter the chemistry, structure, and topography of the interfaces.[53]

### 2.2.4 The Sessile Drop Experiment

The sessile drop experiment (depicted in Figure 2.11) is, in principle, relatively simple and is therefore the most commonly used method to study the wetting behaviour of

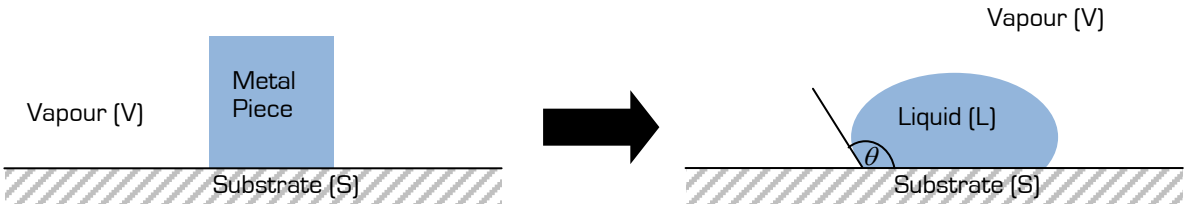


Figure 2.11: Standard sessile drop experiment; a piece of metal is placed onto a substrate prior to heating. During the heating process, the metal melts and forms a drop of liquid that spreads out over the surface. The contact angle $\theta$ can be measured as shown.

both chemically inert and reactive systems. It allows a drop of liquid to spread over a horizontal, solid surface until an equilibrium configuration is reached. Once in capillary equilibrium, the angle at which the droplet touches the surface can be measured as the contact angle $\theta$.[53]

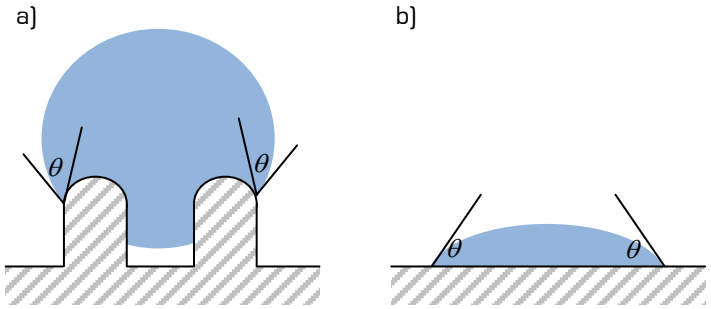


Figure 2.12: a) Schematic of the effect of roughness: Even though the droplet does not touch the actual surface, the same contact angle $\theta$ between the droplet and the protrusions is apparent as on the flat surface. b) Shows the wetting behaviour of a water droplet on a flat surface of the material of a lotus leaf.

As for all wetting systems, the surface quality of the substrate has a significant impact on the wetting behaviour of the system. This can be understood easily, considering the commonly known lotus effect: due to controlled and very high surface roughness, a water droplet does not wet the surface of a lotus plant leaf, but only the tips of the protrusions on the surface (Figure 2.12(a)[54]). This means that the contact angle measured between the drop and the leaf's apparent surface (180°) does not represent the true contact angle. The true contact angle, however, appears where the droplet contacts the protrusion. Similarly, surface pro- or intrusions can pin the triple line of the liquid, solid, and vapour phases in a wetting experiment and prevent a drop from spreading or receding, thereby preventing the true contact angle to establish.

Thus, it is important for the reproducibility and the reliability of the measured wetting behaviour to conduct the experiment using a perfectly flat substrate, or at least a substrate with controlled roughness.[55]



### 2.2.5 Wetting Behaviour of Aluminum and its Alloys

The strong affinity of pure metals for oxygen, even at room temperature, causes many metals to have an oxide surface layer. In the case of aluminum, this affinity for oxygen is strong enough that chemically pure aluminum instantaneously forms an oxide layer when it is exposed to air. In a standard sessile drop experiment, as depicted in Figure 2.11, where a metal particle is placed on a substrate prior to heating it above the metal's melting point, this surface oxide layer interferes with a true metal / substrate interface, as the oxide does not disappear when the metal melts. This leads to a wide range of reported results, which are dependent (to a certain degree) on the thickness of the surface layer. Whilst thick layers can inhibit any movement of the triple line, thin layers can easily deform, allowing the drop to have a smooth and round appearance.[53] In either case, however, the liquid metal does not contact the substrate. A contact angle measured under such conditions is obviously not representative of the actual wetting system.

Table 2.1 compiles contact angles of aluminum on sapphire measured by different research groups. Besides the fact that the contact angles at 700°C vary from over 165° to less than 90°, it also shows a significant change in contact angle between 700°C and 1000°C. For various wetting systems involving aluminum, this change occurs over several minutes and is explained by a reaction of the aluminum oxide skin on the surface of the aluminum drop with the drop itself at elevated temperatures and low oxygen partial pressure:[15,53,56,57]

$$4\,Al_{(l)} + Al_2O_{3\,(skin)} \leftrightarrows 3\,Al_2O_{(g)}\uparrow \qquad \text{Eq. 2.10}$$

The reduction of the oxide skin surrounding the molten metal results in the observed contact angle change between 700°C and 1000°C. The event is dependent on both the oxygen partial pressure in the furnace and the temperature, and occurs for an

Table 2.1: Comparison of contact angles of aluminum on sapphire, measured by different research groups

| Reference | Atmosphere | 700°C | 1000°C | Remark |
|---|---|---|---|---|
| *WOLF* et al.[17] | $1.3 \cdot 10^{-4}$mbar | 167° | 98° | |
| *BRENNAN* et al.[13] | $3.8 \cdot 10^{-5}$mbar | 120° | 88° | |
| *NAIDICH* et al. [58] | Unknown | 90° | 78° | Fresh drop method (unknown setup) |
| *JOHN* et. al.[14] | Zr crucible / argon flow | 90° | – | |
| *LAURENT* et. al.[15] | $5 \cdot 10^{-7}$mbar | 101° | 86° | |
| *WANG* et al.[59] | $1.2 \cdot 10^{-6}$mbar with getter | 90° | – | Fresh drop method (vertical setup) |
| *HO* et al.[60] | $1.2 \cdot 10^{-6}$mbar with getter | 90° | – | Fresh drop method (vertical setup) |
| *SHEN* et al.[61] | Argon | 128° | 110° | Fresh drop method (vertical setup) |

oxygen partial pressure of $p(O_2) = 10^{-12}$mbar at 827 °C.[53] Therefore, the majority of published wetting data involving liquid aluminum covers the temperature range above 800 °C.

While the wetting behaviour of pure metals, including aluminum, on the various ceramics at high temperatures has been studied fairly extensively, wetting of aluminum alloys on ceramic substrates has received less interest. Based mostly on tin-aluminum alloys on sapphire, *LI* et al.[62,63], using a monolayer approximation, developed a model predicting contact angle, $\theta$, and work of adhesion[c][64], $W_a$, isotherms for binary alloys on ionocovalent oxide ceramics (such as $Al_2O_3$).

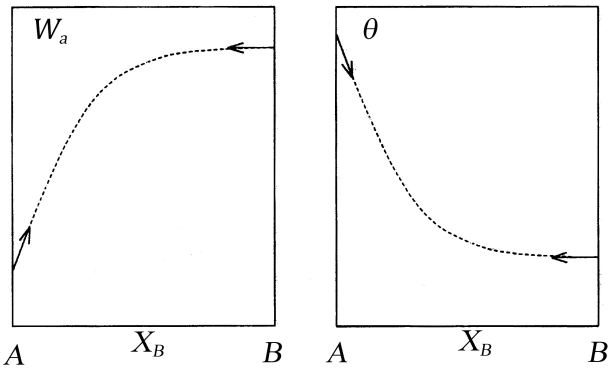


Figure 2.13: Typical $W_a(X_B)$ and $\theta(X_B)$ isotherms for systems like Cu-Al alloys on $Al_2O_3$ with component A being Cu and component B being Al.

[c] Work of adhesion is the reversible work required, per unit area, to separate the liquid from the solid. $W_a = \gamma_{LV} \cdot (1 + \cos\theta)$



For an alloy, in which element B is tensioactive[d] at an A-based alloy / oxide ceramic interface as well as (though to lesser extent) at the surface of the A-based alloy, this model predicts the behaviour of contact angle and work of adhesion isotherms to act as depicted in Figure 2.13[63].

Since aluminum is tensioactive in a liquid predominantly copper containing copper-aluminum alloy, the model predicts that $W_a$ increases while $\theta$ decreases upon small additions of aluminum to the alloy. In contrast, small copper additions to aluminum have hardly any effect on either parameter according to the model.[63]

#### 2.2.5.1 Experimental Setups removing the Aluminum Oxide Layer

Even though it is possible to remove the natural oxide layer surrounding aluminum if the chosen experimental temperature is high and the oxygen partial pressure is maintained sufficiently low, the standard sessile drop experiment bears the important problem that an experimental start time is hard to define. This is due to the fact that, even if one can determine the exact temperature of the metal, and thereby the moment when it melts, it is close to impossible to pinpoint the exact moment at which the oxide layer is removed. Hence, the time at which the true liquid metal / ceramic substrate interface is being established and the wetting experiment actually commences cannot be detected. Furthermore, placement of the metal, with or without its oxide layer, onto the substrate always occurs well in advance of the experimental temperature being reached. This means that the wetting experiment actually starts before the experimental temperature is reached. The effects thereof are difficult to determine.

[d] A substance is called tensioactive in a liquid if it reduces the surface or interface energy of that liquid.

Besides conducting a standard sessile drop experiment at temperatures and under vacuum conditions under which the surface oxide layer on the metal becomes unstable, there are three approaches mentioned in literature that avoid the presence of the oxide skin during the wetting experiments.

*2.2.5.1.1 Cleaning by Ion-Sputtering*

*Levi* et al.[65,66] have utilized a method in which they sputter all six faces of metal cubes with argon ions in an ultra-high vacuum system to remove the oxide. Immediately after this cleaning step, and without breaking the vacuum, the aluminum cubes are placed on the substrate and melted. This technique avoids issues with the oxide layer interfering with a true liquid metal / substrate contact; however, it does not solve the problem that the liquid metal / ceramic substrate contact is established before the experimental temperature is reached.

*2.2.5.1.2 Dewetting Experiments with Deposited Layers*

Several research groups[67-69] report wetting data involving various metals that is obtained in dewetting experiments: in a first step, the substrate, covered with a random piece of material of equal or larger size, is placed inside an electron gun evaporation or molecular beam epitaxy chamber. After the chamber is evacuated, a comparatively thick layer of aluminum is deposited. The elemental aluminum reacts immediately with the residual oxygen inside the chamber and thereby reduces the residual oxygen partial pressure to a level lower than that required to oxidize aluminum at the temperature at which the coating is conducted. Immediately after, the material used to cover the substrate is removed and a thin (100 to 500nm thick) layer of the metal of choice is deposited on the substrate. During the actual experiment then, the coated substrate is heated to the experimental temperature. Once the layer melts, it breaks up and the metal melt retracts into micron-size droplets in order to reach equilibrium.



This very sophisticated method allows extremely low oxygen partial pressures to be reached at least while the metal to be investigated is deposited on the substrate. However, like the standard sessile drop setup or the argon sputtering technique, it does not allow the wetting experiment to be started at a specific temperature, since wetting commences as soon as the metal melts. Moreover, it is particularly difficult to measure the wetting behaviour of the respective system while it is at the experimental temperature, as it is governed by chance whether or not one obtains an unobstructed view of a droplet in profile. Therefore, most commonly when this technique is employed, the contact angle measurements are conducted once the droplets have solidified following the experiment and once the sample can be sectioned. Conducting contact angle measurements on a solidified drop, however, is not necessarily representative of the conditions while the drop is at experimental temperature, as the contact angle may change during cooling and before the metal solidifies. Additionally, if the thermal expansion between substrate and metal is sufficiently different, plastic deformation can introduce changes in the apparent contact angle, which are not representative of the wetting system.

*2.2.5.1.3 Dispensed Drop Method*

*NAIDICH* et al.[58] first suggested another variation of the standard sessile drop experiment: The idea is to melt the metal in an inert syringe, which is not wetted by the metal, within a vacuum furnace arrangement. Once the designated experimental temperature (above the melting point of the metal) is reached, the melt in the syringe is forced through the small orifice in the syringe onto the substrate. This mechanically strips the oxide layer off the surface of the liquid metal. (Figure 2.14[53])

While this method produces a clean drop / substrate interface, given that the furnace atmosphere is clean enough to prevent significant re-oxidation while the drop is being dispensed, it furthermore allows wetting experiments with contact angle measurements to be conducted at specific experimental temperatures.

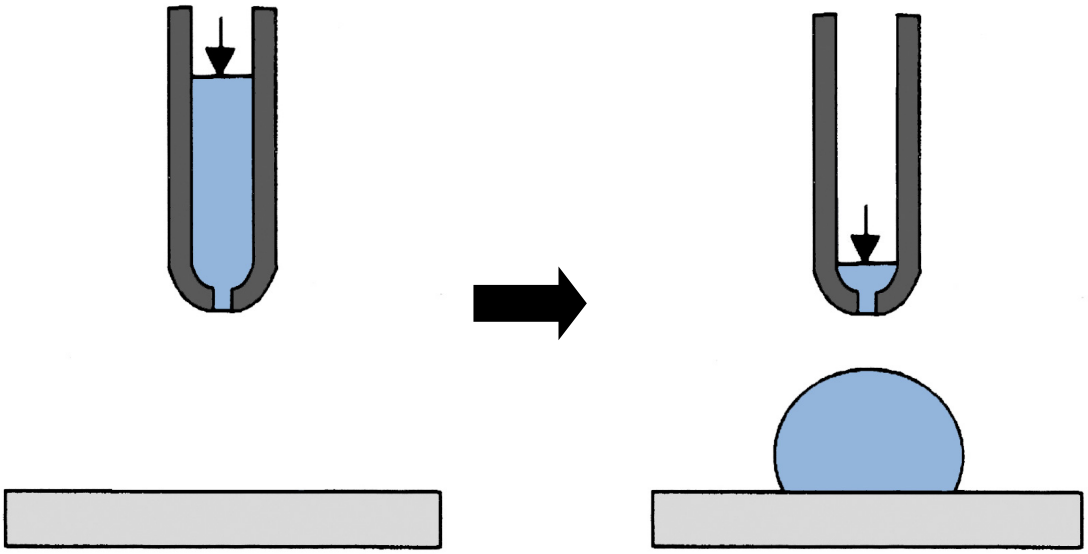

Figure 2.14: Dispensed drop method – modified sessile drop experiment to suit measurements of systems involving highly oxidizing metals. The metal is placed in a syringe prior to heating. During the heating process, the metal melts but remains in the syringe. Once experimental conditions are reached, the melt is forced through the orifice in the syringe onto the substrate, physically stripping the oxide layer off the metal. A clean drop forms that spreads out over the surface.

#### 2.2.5.2 Reactive vs. Non-Reactive Wetting at Elevated Temperatures

At elevated temperatures, the reactivity of most elements and compounds is significantly increased. It is, therefore, that wetting experiments involving many metal / ceramic systems cannot be considered non-reactive. In a first approximation, the decision regarding the reactive or non-reactive character of wetting can be based upon the spreading kinetics: a non-reactive system usually reaches capillary equilibrium within less than 0.1 seconds. Reaching equilibrium more slowly is thus generally considered an indication that spreading of the drop is controlled by interfacial reactions such as atoms of the liquid going into solid solution, atoms of the ceramic being dissolved by the metal, or a reaction layer forming between the liquid metal and the substrate.[53]

A more precise differentiation between reactive and non-reactive systems involving oxide ceramics, $A_nO_m$, considers the dissolution of the substrate in the metal melt,



for which the dissolved mole fraction of oxygen in the liquid metal, $X_O$, is the metric.[70,71] It is given by:

$$X_O = \left(\frac{m}{n}\right)^{\frac{n}{n+m}} \cdot e^{\frac{\Delta G_R^*}{(n+m)RT}} \qquad \text{Eq. 2.11}$$

where $\Delta G_R^*$ is the standard Gibbs reaction energy per mole of dissolving oxide ceramic, $R$ is the ideal gas constant, and $T$ is the absolute temperature in Kelvin. According to *EUSTATHOPOULOS* et al.[53], contact angles, $\theta$, can be assumed to be constant over time, if $X_O$ is smaller than $10^{-6}$; such systems are considered non-reactive. For larger values of $X_O$, the reactivity increases noticeably and the system must be treated as reactive.

Furthermore, *EUSTATHOPOULOS* et al.[53] claim that the contact angle remains unaffected by a residual oxygen partial pressure in the furnace atmosphere[e] in systems that show $X_O$ values well in the non-reactive regime. In systems with oxygen mole fractions around $10^{-6}$ or higher, however, a significant impact of the residual oxygen in the atmosphere on the contact angle must be expected.[53] It is therefore commonly accepted that wetting systems such as Al / $Al_2O_3$ or Cu / $Al_2O_3$, are considered non-reactive as their respective oxygen mole fractions have been reported as $3 \cdot 10^{-6}$ and approximately $10^{-8}$.[72]

In contrast to this classification several researchers reported the formation of a reaction product at the interface for both wetting systems; $Al_2O_3$ in the case of the pure aluminum / $Al_2O_3$[65] and $CuAlO_2$ for the pure copper / $Al_2O_3$ systems.[73] While such reaction products close to the triple line (between the solid-liquid, liquid-vapour, and solid-vapour interfaces) can be explained by residual oxygen from the furnace

[e] In high vacuum or in reducing atmospheres, the oxygen partial pressure is typically lower than $10^{-7}$mbar.

atmosphere reacting with the liquid metal, the same explanation becomes doubtful for such reaction products found at the Al / $Al_2O_3$ interface far from the triple line. According to *Levi* et al.[65,66], aluminum is continuously oxidized at the interface due to an unexpectedly high oxygen activity along that interface. The exact nature and origin of this oxygen activity, however, is still somewhat unclear. [65,66,69,73]

As the reaction products in the Al / $Al_2O_3$ and Cu / $Al_2O_3$ systems are not caused by dissolution and re-precipitation of the substrate in the liquid metal but by continuous oxidation, the formation of these reaction products at the interface does not contradict the abovementioned classification as non-reactive wetting systems based on the dissolved oxygen mole fraction, $X_O$. Instead, the formation of $Al_2O_3$ and $CuAlO_2$ as reported has been explained by the non-equilibrium character of these systems.

Although the oxygen mole fraction approach is, in general, valid for non-oxide ceramics as well, their behaviour is still very different. This is because many of these non-oxide ceramics themselves show a strong tendency to oxidize and the presence of an oxide layer dramatically changes their wettability by liquid metals.[53]

The wetting behaviour of pure aluminum on silicon carbide is a reactive system as the contact angle is strongly affected by reactions occurring between silicon carbide and aluminum. At temperatures around 800 °C, the contact angle between liquid and substrate has been reported to continuously change over a range of several hours. At higher temperatures, the reaction between silicon carbide and aluminum (forming $Al_4C_3$ that precipitates, and silicon that is dissolved by the aluminum droplet) is so pronounced that the contact angle resembles instead that of the aluminum / aluminum carbide system.[74,75]

At even higher temperatures, it has been reported that the surface of SiC changes. While the ceramic is oxidized below approximately 1050 °C (depending on the vacuum), above it graphitizes, releasing volatile SiO and CO compounds. The graphitized

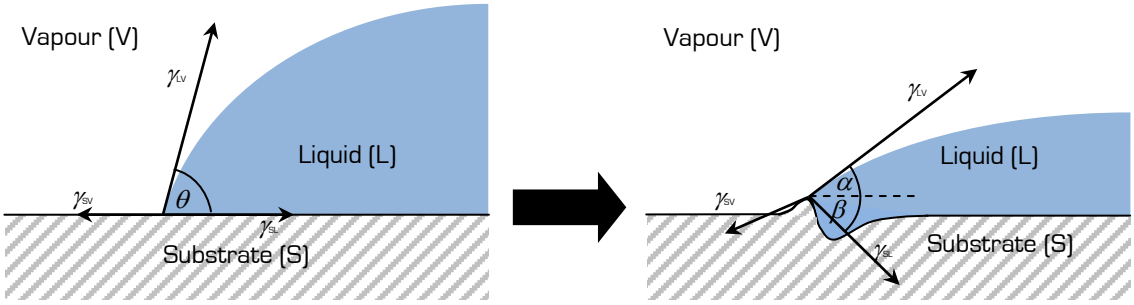


Figure 2.15: Deformation of the substrate and subsequent change of the apparent contact angle (exaggerated); $\alpha + \beta$ is equal to the true contact angle $\theta$

surface is considered the reason that Cu / SiC wetting systems, though considered reactive as well, have contact angles of 138° reported above 1200°C, while silicon of the substrate is still dissolved in the liquid drop.[76]

### 2.2.6 Additional Considerations

If the chosen experimental temperature is high enough for local self-diffusion to become noticeable in the substrate, the latter can no longer be considered perfectly rigid (for ceramics this is generally deemed to be the case at temperatures in the area of 0.4 to 0.5 of the melting temperature)[77]. For $Al_2O_3$ substrates this means that above about 1000°C diffusion processes within the substrate occur, allowing the system to reduce its free surface energies. This will result in the smoothing of light scratches on the surface, but also the deepening of grain boundary grooves. At the triple line the three phases in contact aim to reach an energy minimum, resulting in deformation of the original ceramic surface and the formation of a ridge and/or a trough close to the triple line, following the action of the three surface energies (Figure 2.15).[65,67,68,77-81]

During high temperature experiments, formation of such a ridge along the triple line and a trough underneath the drop in close vicinity to the triple line causes the validity of the standard *YOUNG*'s equation to be questionable, since the apparent contact

angle $\alpha$ alone is not representative for the wetting situation as it disregards the changed direction of $\gamma_{SL}$.[68,77]

Moreover, *Saiz* et al.[77] found that the diffusion processes that cause grain boundary grooving on polycrystalline alumina are more pronounced underneath the sessile drop than at a solid-vapour surface. According to the non-reactive character of both wetting systems,[53] substrate atoms should not be properly dissolved in the liquid. Nevertheless, interfacial diffusion has been identified as the rate-limiting atomic transport mechanism. This means that the movement of atoms along the interface is significantly accelerated by the presence of the liquid metal in comparison to surface diffusion along the solid-vapour surface and remains somewhat in contradiction with the non-reactive classification of the two wetting systems, suggesting that dissolution and re-precipitation of the substrate are virtually inexistent.

## 2.3 Effect of Ceramic Particles on Foam Stability

In the discussion about foam stability, it is important to understand that foams, by nature of their high surface free energy state, are thermodynamically unstable structures. Hence, the term *foam stability* only refers to kinetic stabilization due to retarded foam collapse. In addition, it has been found to be impossible to foam single component liquids because of insufficient bubble stability. Bubbles in liquids like sparkling water or pure aluminum rupture immediately upon arrival at the surface.[3,46,82]

In order to better present the current state of knowledge with respect to metal foam stability, the physics of aqueous foams will be addressed first.

### 2.3.1 Stability of Aqueous Foams

Liquid foams are two phase systems consisting of gas cells enclosed by liquid. Most aqueous foams owe their existence solely to the presence of constituents, which are surface active and concentrated in surfaces and films of the liquid. These constituents are called surfactants. Most surfactants are organic, amphiphillic molecules that consist of a polar *head* and a non-polar *tail*, thereby showing hydrophilic behaviour at the one end and hydrophobic behaviour at the other.

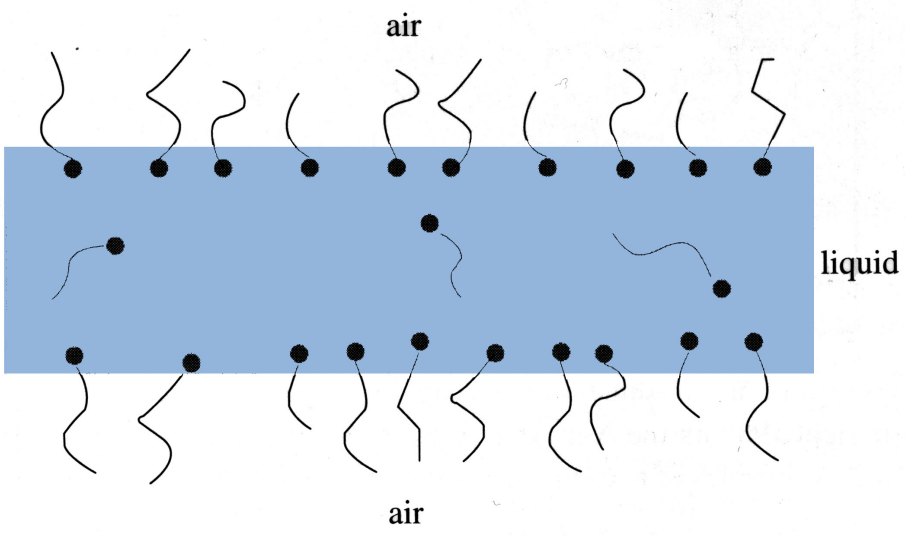


Figure 2.16: Surface active molecules aligned along the liquid-gas interface; predominantly, the polar molecule "head" is submerged in the aqueous liquid, while the non-polar "tail" protrudes into the gas (in this case air).

The stabilizing effect of surfactants (such as detergents or long-chained alcohols) on cell walls in aqueous foams is twofold: on the one hand the surfactants align in a monomolecular arrangement at the liquid-gas interface (Figure 2.16[3]); this increases the elasticity of the film. As a result, the surface energy of the film is reduced and film rupture retarded. On the other hand, the regular, monomolecular alignment of surfactant molecules with the polar heads in the liquid induces an electrostatic field, which causes two liquid-gas interfaces to repel each other. This leads to an increase in cell wall thickness and more liquid being retained within the walls. In addition, the repul-

sive forces between liquid-gas interfaces stabilize the bubbles during the rise to the surface of the liquid and prevent coalescence.[46,47]

In the field of mineral processing, more specifically in flotation, it has been found that not only amphiphillic surfactants stabilize the froth in flotation cells, but that the mineral particles that are to be separated by this process can, under certain conditions, aide stabilizing the froth and particularly the rising bubble.[83,84]

The liquid phase in a foam is mostly found along the triple junctions where three foam cells meet; these junctions are called *PLATEAU* borders. Because the radius of curvature of the cell wall at the *PLATEAU* border is smaller than that in between such triple junctions, capillary forces continuously draw liquid from the films between two cells into the *PLATEAU* borders, causing the films to thin. The decrease in cell wall thickness eventually results in such severe instability of the film that it barely withstands the pressure difference, $\Delta p$, across the interface. Under such circumstances, sound waves, mechanical vibrations, or even thermal fluctuations can cause the film to rupture and the two adjacent bubbles to coalesce.[3]

### 2.3.2 Stability of Metal Foams

As with aqueous foams, for the production of metal foams, specific effort must be invested into stabilizing the foam against drainage, pore coalescence, and collapse due to film rupture. In foams produced via the *CYMAT*-process, an increase in foam stability has been obtained by adding ceramic particles of micron size (such as alumina, silicon carbide, or titanium boride) into the melt prior to foaming.[20] The stability of foams fabricated via the powder metallurgical route is believed to be due to the presence of oxide frameworks originating from the oxide layers of the metal powder particles.[6] Nevertheless, *KENNEDY* and *ASAVAVISITHCHAI*[9,11] showed that, also via the PM route, an increase in liquid foam stability can be obtained by adding ceramic particles to the powder mixture.



It is important to understand that these particles do not behave like amphiphillic surfactants in aqueous foams. This is not only because ceramic particles are not amphiphillic, but also because the electrostatic fields that are responsible for the rejection of two double layers in aqueous solutions would be shielded in liquid metals.[8]

The mechanisms, which are believed to cause the positive effect of ceramic particles on foam stability, are an increase in bulk and surface viscosity and predominantly the generation of a separating force. For aluminum foams produced from powder compacts, the critical film thickness before rupture has been found to range between 40 and 100µm[85]; similar values have been obtained for foams produced via the *CYMAT*-process.[86]

#### 2.3.2.1 Increase in Viscosity

Like in aqueous foams, film thinning occurs immediately after the foam starts to develop. Capillary forces draw liquid into the *PLATEAU* borders from where gravity drains the metal out of the foam.[87,88]

Even though the foam does not become thermodynamically stable with increasing viscosity of the liquid, it can be understood that a decreased flow rate of liquid from the *PLATEAU* borders decreases the capillary draw of the borders on the cell walls and hence increases its lifetime. Thus, the foam suffers less coarsening during the time of solidification.

#### 2.3.2.2 Generation of a Separating Force

In producing metal foams via the *CYMAT*-process, it has been found empirically that bubbles created in the melt are stabilized by ceramic particles preventing bubbles from coalescing.[22] This mechanism seems similar to the effect of two double layers of surfactants in aqueous foams repelling each other.

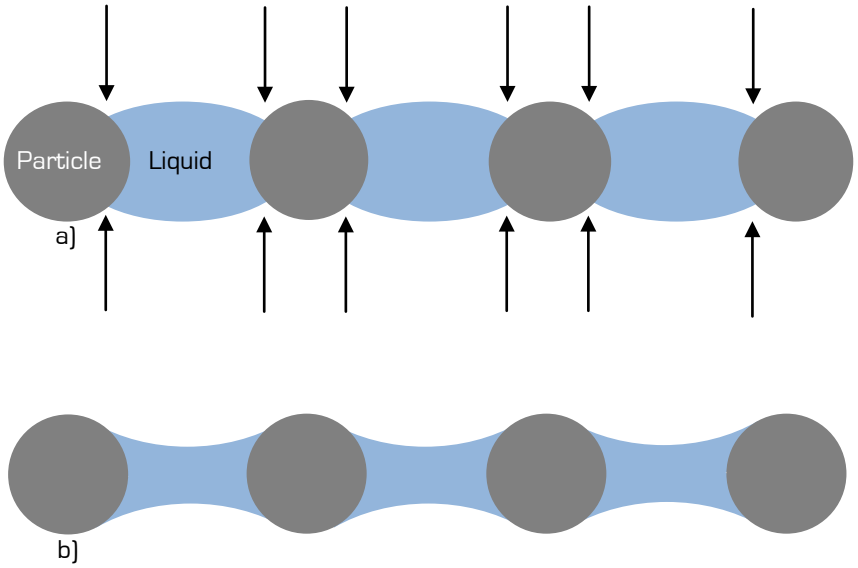


Figure 2.17: Simplified model to illustrate the effect of particle wettability on film stability. Model assumes a mono layer of particles aligned within the film between two cells; a) liquid metal wets particles poorly, inducing predetermined rupture origins (arrows); b) liquid metal wets particles well, allowing the remaining liquid to be to retained within the film

A simplified model of liquid-gas interface stabilization proposed by *KAPTAY*[4] assuming a one-particle thick layer surrounding the entire bubble was developed based on this observation. From this model, in order for the particles to stabilize the bubble, *KAPTAY* suggested a contact angle between the liquid metal and the added ceramic particles in the range of 20° to 90°.

This can be better understood considering the sketch in Figure 2.17[82]: Once film thinning causes the thickness of the cell walls to approach the diameter of the solid particles, partially wetted particles tend to sustain the liquid within the film and prolong the onset of rupture (Figure 2.17 b)). In contrast, poorly wetted particles (i.e. contact angles above 90°) cause the liquid to retract around the particles (Figure 2.17 a)). The interfaces between liquid and particles then behave like predetermined rupture origins and the film will collapse more rapidly. A theory by *MINTO* et al.[89] explains that particles can have a stabilizing effect on foams only if the liquid does not totally wet the particle, i.e. the contact angle between the particle and the liquid is

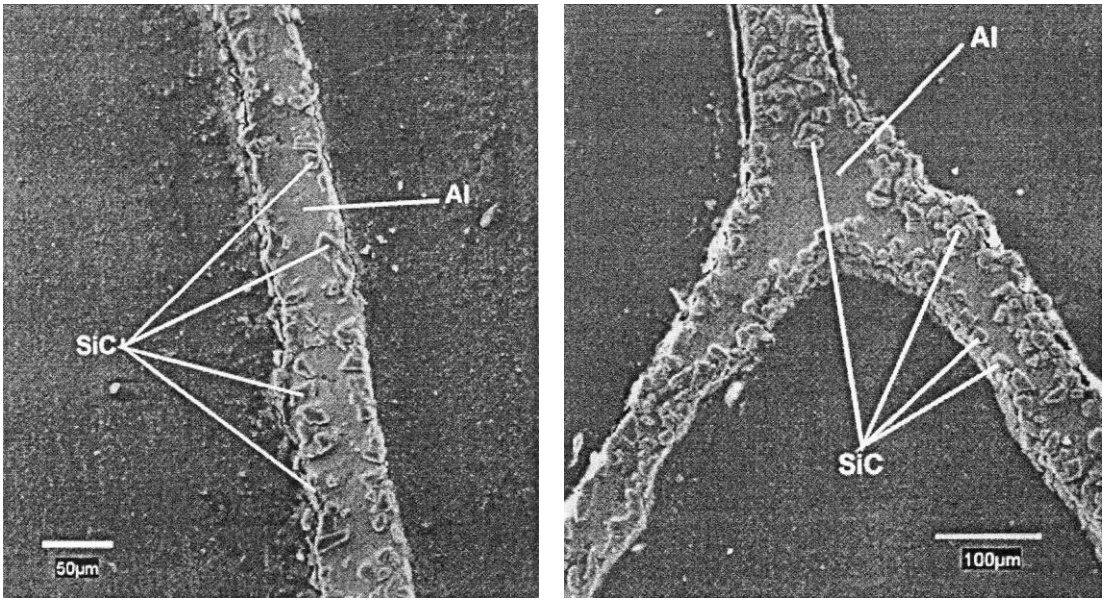


Figure 2.18: a) SEM micrograph of an aluminum foam cell wall; b) SEM micrograph of a *PLATEAU* border region in an aluminum foam. Both micrographs show distinct arrangement of the SiC particles at the liquid gas interface.

greater than zero, as such particles would be entirely immersed in the liquid and not further protrude the interface into the bubble.

Figure 2.18[82] shows two SEM micrographs of the alignment of silicon carbide particles in the cell walls of an aluminum foam. From these, it is obvious that the model[4] derived by *KAPTAY*, is not entirely correct, as it assumes a mono-layer of spherical particles of uniform size. Moreover, additional experimental results by *LEITLMEIER* et al.[18] and *IP* et al.[82] suggest that complete particle coverage of the bubble surface is not required in order to obtain stable foams.

Incorporating these findings, *KAPTAY* presented a very complex and theoretical derivation[12], which shows that depending on different particle arrangements at the liquid-gas interface, different wetting behaviours are most beneficial. It has been shown that for a closely packed single layer of particles, the optimum contact angle is 70°, while for a closely packed double layer at the interface 86° is ideal. In the case of 3D networks of particles along the liquid-gas interface surrounding the bubble, *KAPTAY*

further showed that these networks can stabilize the foam even if the wetting behaviour between the liquid and the particles is below 50° and above 129°. *KAPTAY* concludes that contact angles in the range of 70° to 86° are ideal for metal foam stabilization, as closely packed single or double layers are most likely to occur.

The models also show that solid particles, whether they are mixed into a metallic melt or an aqueous liquid, generate a separating force similar to the disjoining pressure of amphiphillic molecules in aqueous foams.

Based on these models, *SUN* et al.[5] performed an experimental simulation in which a surfactant free water-ethanol solution mimicked the liquid metal, and inert plastic particles acted as the ceramic particles. By varying the ethanol content in the solution the wetting behaviour between liquid and plastic particles was altered. From this simulation, an optimal contact angle interval of 75° to 85° was experimentally determined. This is supported by similar experiments by *NAKAE* and *KOTA*[90], who, using ceramic particles to stabilize aqueous, surfactant-free foams, reported comparable values. Both studies match *KAPTAY*'s stabilization theory[12] closely.

By producing metal foams in a reduced gravity environment during parabolic flights *WÜBBEN* et al.[6] were able to essentially eliminate drainage of the liquid from the foam. The finding that the pore size distribution of such foams was not significantly better than that of foams produced under normal gravity drainage conditions led to the conclusion that viscosity must be assigned secondary importance in stabilizing foams.

#### 2.3.2.3 Particle Size Effect

*E*xperimental results by *IP* et al.[82] show that foam stability of both aqueous and metal foams increases with decreasing particle size. It is unclear, however, if this is a true effect of particle size or an indirect effect of surface area, as smaller particles result in a larger surface area if the particle weight fraction remains constant. *JIN* et



al.[19] explain that reduction of the particle size is advantageous only to a certain extent, since the increasing tendency for agglomeration of small particles causes difficulties with mixing the particles into the melt.

In this context, it should be noted that, particularly in the *CYMAT*-process, not only does the potential for agglomeration cause difficulties regarding the homogeneous distribution and suspension of particles in the melt, but also higher particle volume fractions. Significant differences in density between melt and particles further cause the particles to either float to the surface of the melt or settle towards the bottom.

It should be mentioned that an alternative approach to increase stability, especially of aluminum foams, is the deliberate use of oxidizing foaming gases or agents. In this way, oxide layers forming at the liquid-gas interfaces of the bubbles are created in-situ during the foaming process. This provides a significantly higher stability of the foam cell walls,[86] as these oxide layers help to prevent cell coalescence, although particle arrangement at the liquid-gas interface is worsened. However, oxidizing blowing gases cannot replace the presence of stabilizing particles in the melt.[7] Even though it is not explicitly mentioned, such positive effects of oxidizing blowing gases are implied in *ALCAN*'s patents[19,20], in which, amongst others, air is used.

# 3 RESEARCH OBJECTIVE

The primary objective of the present project was to measure *correct* wetting data of aluminum and several of its alloys on different ceramics. As has been explained previously in section 2.2.5, it is important in this context to avoid errors caused by the native oxide layer on the metal or the surface roughness of the substrates.

The second focus of the present work was the acquisition of metal foam expansion and stability data of the same alloy / ceramic combinations in order to evaluate the reported link[5,12] between wetting behaviour and foam morphology based on the obtained wetting and foaming results.

Conclusions are drawn regarding the validity of selecting alloy / ceramic particle combinations for metal foam production based on results from wetting experiments.



# 4 EXPERIMENTAL METHODOLOGY

For the purpose of the current project, two sets of fundamentally different experiments were conducted: wetting tests and foaming tests. Both trials required prior lab work such as alloy casting, or powder mixing and compaction, respectively. Several analysis methods were employed to aid the interpretation of the results.

For the wetting experiments temperature and substrate were varied: as substrates, polycrystalline silicon carbide ($\alpha$-SiC), polycrystalline aluminum oxide (hereafter referred to as alumina), as well as single-crystalline aluminum oxide (hereafter referred to as sapphire) were tested. The experimental temperatures were 700°C, 730°C, 750°C, and 800°C, as well as 10°C above the liquidus temperature or the melting point of each individual metal or alloy. The wetting tests were carried out under high vacuum. Experiments under inert gas atmosphere, such as argon, which have been investigated in several publications[14,61] were not considered in the experimental matrix as they should yield the same wetting behaviour given that the vapour pressure of the metal under the experimental conditions is the same as under vacuum and the oxygen partial pressure is similar.[53]

## 4.1 ALLOY PREPARATION

The investigated alloys were pure aluminum (Al-99.99), the binary alloys Al-11.5Si, Al-7Cu, and Al-1Mg, as well as the ternary and quaternary alloys Al-7Si-Mg (A356) and Al-1Mg-0.5Si-Cu (AA6061) as they have been suggested in literature[19,20,27] to be suitable alloys for metal foam production. In order to better understand certain

phenomena observed during the wetting experiments additional aluminum-copper alloys were investigated regarding their wetting behaviour.

The alloys were prepared from high purity elements (aluminum, copper, magnesium, and silicon). The base metal aluminum was melted under normal atmosphere in an induction furnace within a fireclay crucible. The use of an induction furnace allowed for a quick melting process and for effective stirring. Once the aluminum was molten, the alloying elements were added. The alloys were cast into a copper mould to obtain coupons of approximately 5cm diameter and 1.5cm height. Subsequent to casting, all coupons were heat-treated for 18 hours at 500 °C[91] in order to homogenize the alloy and remove the cast microstructure.

## 4.2 Chemical Analyses

The chemical analysis of pure aluminum was obtained using atomic absorption spectroscopy on a *Varian* AA240FS. The alloys were analysed using inductively coupled plasma (ICP) spectroscopy (on a *Thermo* Autoscan featuring a mini-crossflow nebulizer with a baffled cyclonic spray chamber) with standards for aluminum, copper, magnesium, and silicon.

## 4.3 Differential Scanning Calorimetry

A small sample of approximately 30mg of each alloy was analysed in a *Setaram* Setsys Evolution differential scanning calorimeter (DSC). The obtained DSC curves provide information about endo- and exothermic processes occurring in the sample during temperature rise or fall, such as melting or crystallization. Using this information, the melting point, $T_m$, as well as liquidus and solidus temperatures, $T_{liq}$ and $T_{solid}$, can be determined: $T_m$ as the temperature at the endothermic peak of the DSC curve during heating of a pure element or stoichiometric compound, and $T_{liq}$ as the tem-



perature at which the heat flow returns to the baseline during heating after the melting peak of a non-stoichiometric compound.[92] A standard 10 $^{\circ C}/_{min}$ heating rate was chosen.

## 4.4 Substrate Preparation

The polycrystalline alumina was purchased from *Superior Technical Ceramics* in the form of tiles with a purity of 99.6wt.% $Al_2O_3$. The polycrystalline silicon carbide tiles (Hexoloy SA SiC) were provided by *Saint-Gobain Ceramics* and also have purity of 99.6wt.% SiC. Since both materials were thinner at the center of the tiles than along the edges, extensive polishing with coarse diamond paste was necessary to achieve flatness. The final polishing step used 1µm diamond paste on a vibro-polisher. The polishing procedure yielded surface roughnesses, $R_{ms}$, of 6.5nm and 14.2nm, respectively overall, and of 3.6nm and 4.2nm, respectively, excluding craters generated by grains that were pulled out of the surface during polishing. The sapphire (EFG Saphikon) material was purchased in the form of thin sheets from *Saint-Gobain Crystals* as A-plane terminated material (i.e. the $(11\bar{2}0)$ plane constituted its surface). The sapphire sheets had a surface roughness, $R_{ms}$, of 3.6nm in the as-purchased condition; a polishing step was therefore not required. The ceramic materials were sectioned into square tiles of approximately 20mm by 20mm. In the case of silicon carbide, the tiles were left on the vibro-polisher until immediately before transferring into the wetting furnace.

## 4.5 WETTING EXPERIMENTS

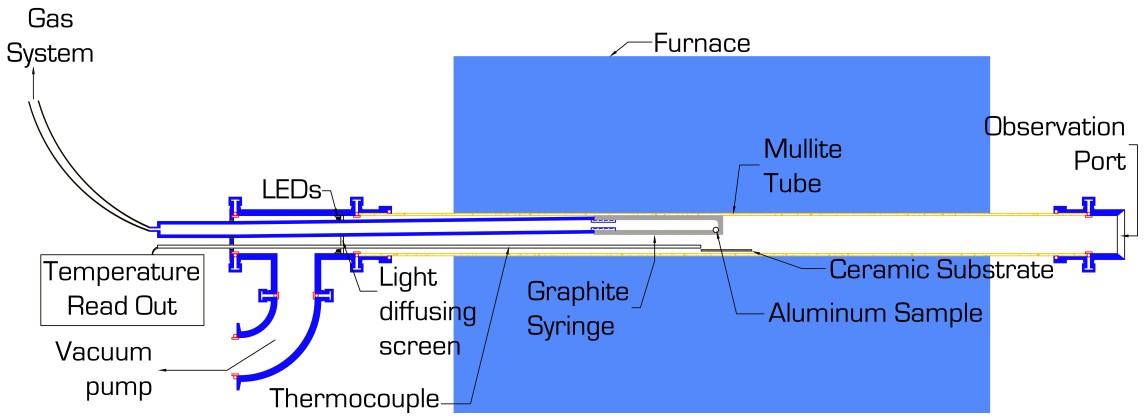


Figure 4.1: Schematic of the vacuum tube furnace setup used for the wetting experiments

In order to investigate the wetting behaviour of the different metals on the ceramic substrates, contact angles were measured in profile using a modified dispensed drop method, following *NAIDICH*'s[58] theory for providing a clean metal / substrate interface.

The tube furnace equipment (Figure 4.1) employed for the wetting experiments is described in detail in Appendix A.

For a wetting experiment the substrate was placed inside the tube in the hot-zone of the furnace with its surface horizontally level. An approximately spherical piece of metal or alloy of roughly 150mg was inserted into the graphite syringe, before the latter was connected to the steel pipe and the vacuum system was closed.

The chamber was then evacuated and heated to approximately 180°C for 10 minutes in order to remove any moisture adsorbed inside the vacuum tube. Then the tube furnace was purged through the syringe with argon and re-evacuated several times. Once a vacuum of at least $2 \cdot 10^{-6}$mbar was reached, the furnace was heated to approximately 850°C. The furnace was held at this temperature for 15 minutes

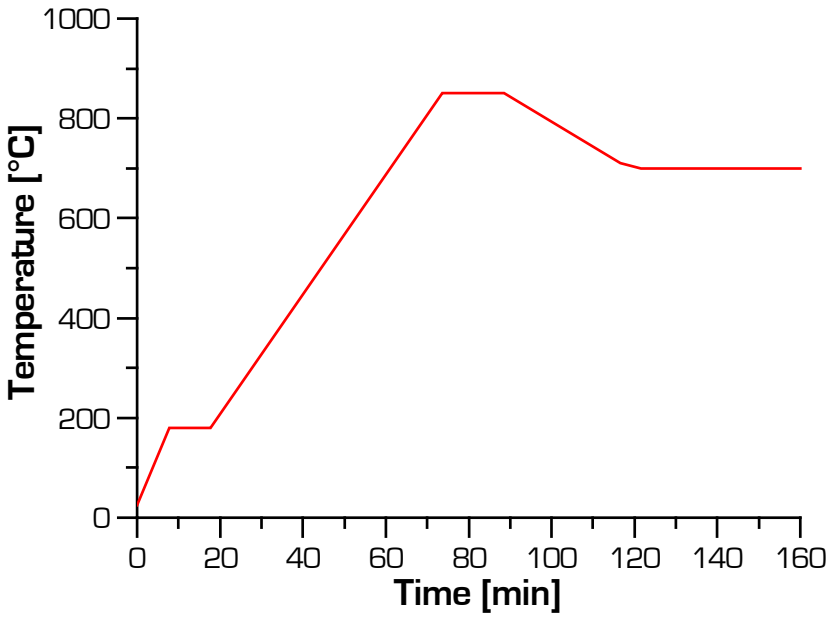


Figure 4.2: Temperature profile for wetting experiments. The experiment was started once the furnace reached the desired temperature. The heating/cooling rates were as follows: Ramp 1: 20 °C/min, Ramp 2: 12 °C/min, Ramp 3: 5 °C/min, Ramp 4: 2 °C/min. Ramp 4 started 10°C above the experimental temperature (which in this case is 700°C).

before the program slowly approached the experimental temperature from above (Figure 4.2). This procedure had two reasons:

- heating the sample to 850°C ensured that the aluminum alloy was entirely melted prior to the experiment, and
- the vacuum pump is able to reach a higher vacuum at a given temperature if this temperature is approached from above rather than from below, since $p \cdot V = n \cdot \mathrm{R} \cdot T$, assuming the behaviour of an ideal gas and that there are no major leaks in the vacuum system.

The experiments were conducted under vacuums better than $10^{-6}$mbar. Titanium sponge granules were placed between the substrate and the observation port, to absorb oxygen that might leak into the tube through the connection of the observation port to the vacuum system.

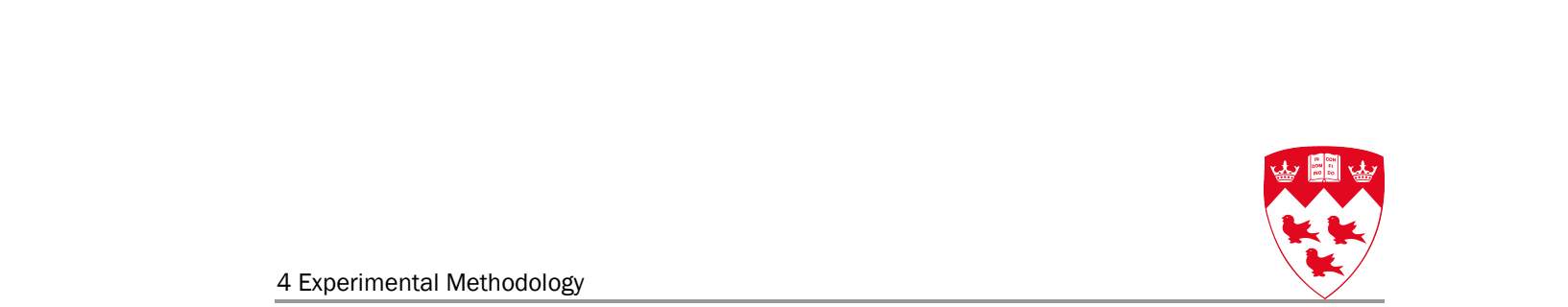

The reservoir in the gas line was sufficiently pressurized with argon to ensure that the melted particle sitting in the intrusion around the orifice in the syringe is only just forced through the pinhole without splattering.

Immediately after injection, pictures of the profile of the sessile drop sitting on the ceramic substrate were taken through the observation port with a high-resolution digital camera (*KONICAMINOLTA* Dimage A200) every 15 seconds over 15 minutes (Figure 4.3). The contact angles on both sides of the drop's profile were measured automatically using *ADOBE* Photoshop CS3 after the tangents of the liquid-vapour interface at the line of contact between the drop and the substrate were identified manually. The average of the two was then plotted over the experimental time at which the photograph was taken. Considering repeatability and angle measurement, this procedure allows a precision of ±3° or better.

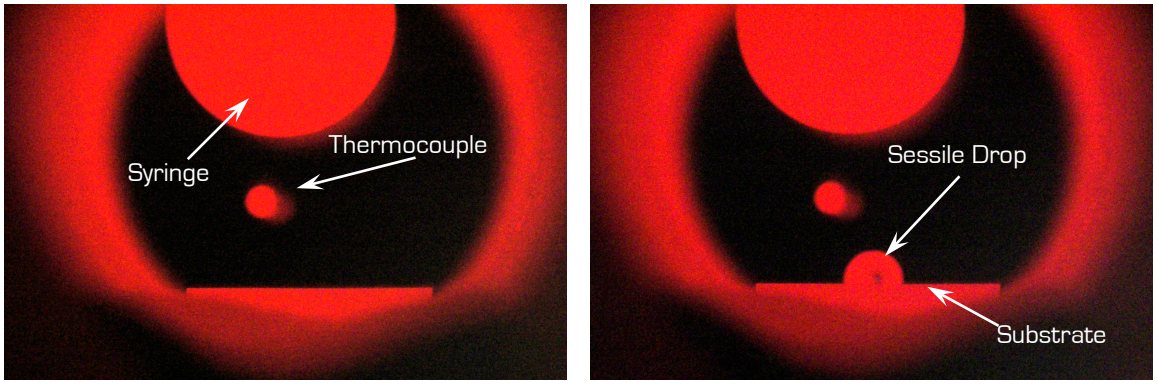


Figure 4.3: Images of the profile of the wetting experiment immediately before (left) and after (right) the injection, taken through the observation port



## 4.6 FOAMING EXPERIMENTS

For reasons of simplicity and the possibility to work with small samples sizes, the powder metallurgical route of metal foam preparation was chosen in the present work. It consists of two main stages: powder mixing and compaction, and foaming of the compacts.

### 4.6.1 Powder Mixing and Compacting

Commercial powders of –325mesh particle size pure aluminum, pure copper, Al-12Si, and Al-50Mg, as well as high purity alumina (sub 5µm particle size), silicon carbide ($d_{50}$ = 5µm particle size), and titanium hydride ($TiH_2$) (–345mesh) were used to prepare powder mixture. $TiH_2$ was chosen as blowing agent following common practice in current aluminum foam research.[9,11,25,26,93,94] The powders were weighed in, to obtain the same compositions as the alloys used for the wetting experiments: pure aluminum, Al-7Cu, Al-1Mg, Al-11.5Si, A356, and AA6061, each with 1wt.% $TiH_2$. In order to maintain constant ceramic particle additions, 8vol.% alumina or silicon carbide were added to the mixtures of metal and blowing agent.

In order to obtain even distribution of the different components in the mixtures, approximately 300g of the powders were weighed into cylindrical 1000ml *NALGENE* containers. 600g of alumina milling balls of 2 to 3mm diameter were added to the mixtures, and the containers were closed and placed on a rolling mill for 30 to 45 minutes. Afterwards, the milling balls were separated from the powders by sieving through a relatively large-mesh sieve.

Foamable precursors were then prepared with a diameter of 30mm in a (with lithium stearate) lubricated die using a two stage compaction process: 1 hour at 350°C and 3500MPa in a hot press, immediately followed by 7 minutes at 4200MPa in a cold press, while the die was still hot. 28g to 32g of powder mixture was weighed-in

depending on the composition, in order to yield constant compact heights of 15mm ± 0.5mm for all mixtures. This procedure achieved theoretical densities of the compacts of 92% to 93% for the Al-7Cu and Al-11.5Si mixtures and above 98% for the Al-99.99, Al-1Mg, A356, and AA6061 mixtures. Higher hot-compaction temperatures, which would have yielded higher compaction in the cases of the aluminum-silicon and aluminum-copper compositions, were not possible, as premature decomposition of the blowing agent had to be avoided.

In a final step immediately before a foaming test, the top and bottom surfaces of the compacts were ground to remove the flash, which formed during powder compaction.

### 4.6.2 Foaming of the Compacts

The foaming experiments were conducted in an expandometer (Figure 4.4), the design of which is explained in detail in Appendix B.

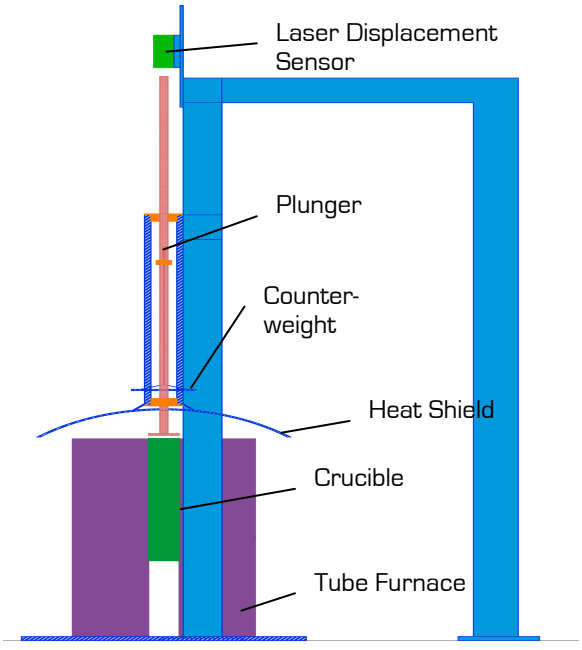


Figure 4.4: Schematic of the expandometer used for foaming experiments.

Prior to a foaming experiment, the plunger was fully immersed into the empty crucible. Once the thermocouple showed the experimental temperature without significant fluctuation, a test was started by withdrawing the plunger from the crucible, dropping a compact into the latter, and replacing the plunger on top of the compact. The data acquisition system subsequently recorded the plunger's displacement with a 1Hz frequency via the laser displacement sensor at the top of the setup.



Foaming experiments were conducted for each powder composition at 90°C and 140°C above the melting point or the liquidus temperature of the metal. Expansion curves were recorded over 20 minutes. Additional experiments were interrupted in order to achieve maximum expansion and to determine the foam stability without the load exerted by the plunger. For the maximum expansion tests, the plunger was retracted at the foaming time at which half of maximum expansion was recorded according to the obtained expansion curves, the crucible was immediately removed from the furnace, and the foam was cooled at room temperature. Similarly, for the foam stability experiments, the plunger was withdrawn from the crucible at the experiment time corresponding to half-maximum expansion; however, the crucible with the sample remained in the furnace for another 5 minutes before it was removed and cooled.

### 4.6.3 Ceramic Powder Analyses

The oxygen and nitrogen contents of the silicon carbide powder were analyzed by inert gas fusion using a *LECO* TCH-600 analyzer. Particle size analyses of the alumina and silicon carbide powders were performed using a *MALVERN* Mastersizer 2000.

## 4.7 MICROSCOPY

Several analysis techniques were employed for the present research, including field-emission scanning electron microscopy (FE-SEM), high-resolution transmission electron microscopy (HRTEM), atomic force microscopy (AFM), as well as X-ray photoelectron spectroscopy (XPS).

### 4.7.1 Scanning Electron Microscopy

From wetting experiment samples, sections approximately through the equatorial plane of solidified alloy drops on the ceramic substrates were prepared using a slow-

speed diamond-wheel cut-off saw. The sections were then mounted in conductive Bakelite, polished to a 1µm surface finish and examined in a *HITACHI* S4700 FE-SEM, featuring an *OXFORD* Inca energy dispersive x-ray spectroscopy (EDS) system, to determine the microstructure and composition of both the interface between the alloy drop and the substrate, as well as the drop itself. To prevent excessive charging of the ceramic substrate materials, accelerating voltages were generally chosen below 5kV.

SEM work on longitudinal metal foam sections was conducted using the same microscope, with lower accelerating voltages and longer working distance.

### 4.7.2 Electron Probe Microanalysis

Some of the wetting samples prepared for SEM work were further examined by electron probe microanalysis (EPMA) using a JEOL 8900 electron microprobe featuring wavelength dispersive spectroscopy (WDS) in order to obtain compositional analyses of some solidified alloy drops after the experiment.

### 4.7.3 Transmission Electron Microscopy

From a number of equatorial sections through solidified alloy drops on substrates that were prepared for SEM analysis, electron translucent slices of the interface region were milled using a focused ion beam microscope (FIB, *HITACHI* FB2000A using 30kV accelerated $Ga^{3+}$ ions). Immediately after ion milling, these specimens were directly transferred to the HRTEM (*JEOL* 2100F) to avoid excessive oxidation.

### 4.7.4 Atomic Force Microscopy

AFM samples of wetting experiments were prepared by chemically removing the solidified drop from the substrate using a 20wt.% NaOH in water solution. This solution completely removes pure aluminum as well as aluminum-based alloys without



attacking or altering the alumina, sapphire, or silicon carbide substrates. After the metal was removed from the substrate, the sample was briefly ultrasonically cleaned in ethanol. Using an NCR tip, the samples were then scanned in a *DIMENSION* 3100 scanning probe microscope in tapping mode (60µm by 60µm areas, scan speed varying between 0.8Hz and 1Hz). The mean surface roughness, $R_{ms}$, was used as the metric to compare the different samples.

### 4.7.5 X-Ray Photoelectron Spectroscopy

The same sample preparation method that was employed to generate AFM samples was used to prepare specimens for compositional interface analysis. The XPS work was performed on a *THERMO ELECTRON CORPORATION* VG ESCAlab-250. The spectra acquisition was carried out in ultra-high vacuum using a 300W $AlK_{\alpha}$ source ($E_{acc}$=15kV, $I_e$=20mA). The analyzed surface was 2mm by 3mm in area and, given the perpendicular take-off angle, the depth sampled was approximately 60 to 100Å.

## 4.8 THERMODYNAMIC MODELLING

Thermodynamic modelling was carried out using *FACTSAGE* 5.5 (2007)[95,96] with the objective to simulate the results to be expected from certain wetting experiments. The obtained thermodynamic data was then further processed using *MICROSOFT* Excel 2007 and *ORIGINLABS* Origin Pro 8.0 in order to give meaningful information with respect to the modelled experimental conditions.

# 5 RESULTS & DISCUSSION

The results and discussion chapter will follow a thematic order: After the presentation of chemical analyses of the metals used for the wetting experiments, DSC curves of the metals are reviewed. Subsequently, the wetting behaviour of the metals on the different substrates will be discussed including thermodynamic simulations and microscopy findings, before foaming results of the various alloy / ceramic particle systems are covered. Lastly, the results will be put in context with *KAPTAY*'s stabilization theory.[4,8,12]

## 5.1 CHEMICAL ANALYSES

The chemical analysis of pure aluminum is presented in Table 5.1; the compositions of the alloys are presented in Table 5.2. As magnesium is known to be volatile when liquid and hence is known to evaporate during alloying in the liquid phase, more magnesium was weighed-in during alloy preparation than the nominal composition.

The chemical analyses show that the compositions of the different alloys reproduce the nominal compositions reasonably well.

Table 5.1: Chemical composition of pure aluminum obtained using atomic absorption spectroscopy

| Element | Al | Si | Cu | Mg | Fe | Mn | Ti | Zn |
|---|---|---|---|---|---|---|---|---|
| wt.% | 99.9947 | 0.0006 | 0.0013 | 0.0021 | 0.0007 | 0.0001 | 0.0001 | 0.0002 |



Table 5.2: Chemical composition of the alloys obtained using inductively coupled plasma spectroscopy

| | Al [wt.%] | Si [wt.%] | Cu [wt.%] | Mg [wt.%] | Fe [wt.%] |
|---|---|---|---|---|---|
| **Al-11.5Si** | 88.50 | 11.48 | – | – | 0.02 |
| **Al-1Mg** | 98.86 | 0.01 | – | 1.13 | – |
| **A356** | 92.97 | 6.66 | – | 0.34 | 0.03 |
| **AA-6061** | 97.99 | 0.43 | 0.18 | 1.38 | 0.02 |
| **Al-4Cu** | 95.96 | 0.03 | 3.98 | – | 0.03 |
| **Al-7Cu** | 92.80 | 0.02 | 7.18 | – | – |
| **Al-11Cu** | 88.70 | 0.02 | 11.27 | – | 0.01 |
| **Al-33Cu** | 68.06 | 0.27 | 31.59 | – | 0.07 |
| **$CuAl_2$** | 46.94 | 0.06 | 52.94 | – | 0.05 |

## 5.2 Differential Scanning Calorimetry

The DSC curves of pure aluminum, as well as Al-11.5Si, Al-1Mg, A356, and AA6061 are presented in Figure 5.1. Similarly, Figure 5.2 shows the DSC curves of the aluminum-copper alloys.

It can be seen that all tested alloys with the exception of the eutectic composition Al-33Cu and the stoichiometric compound $CuAl_2$ show either asymmetrical melting

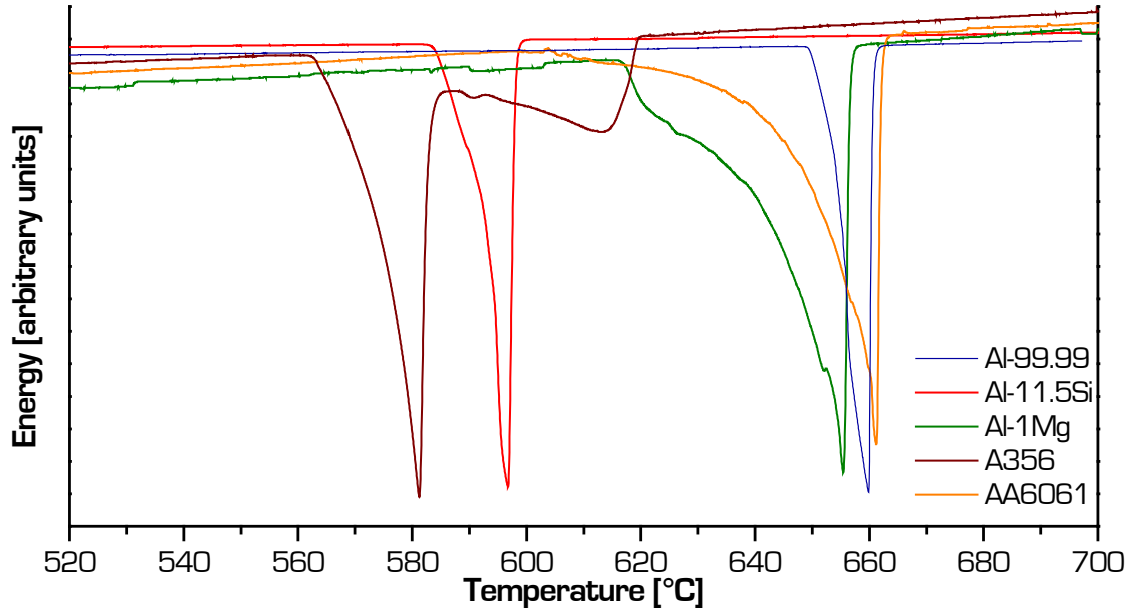


Figure 5.1: DSC curves of Al-99.99, Al-11.5Si, Al-1Mg, A356, and AA6061

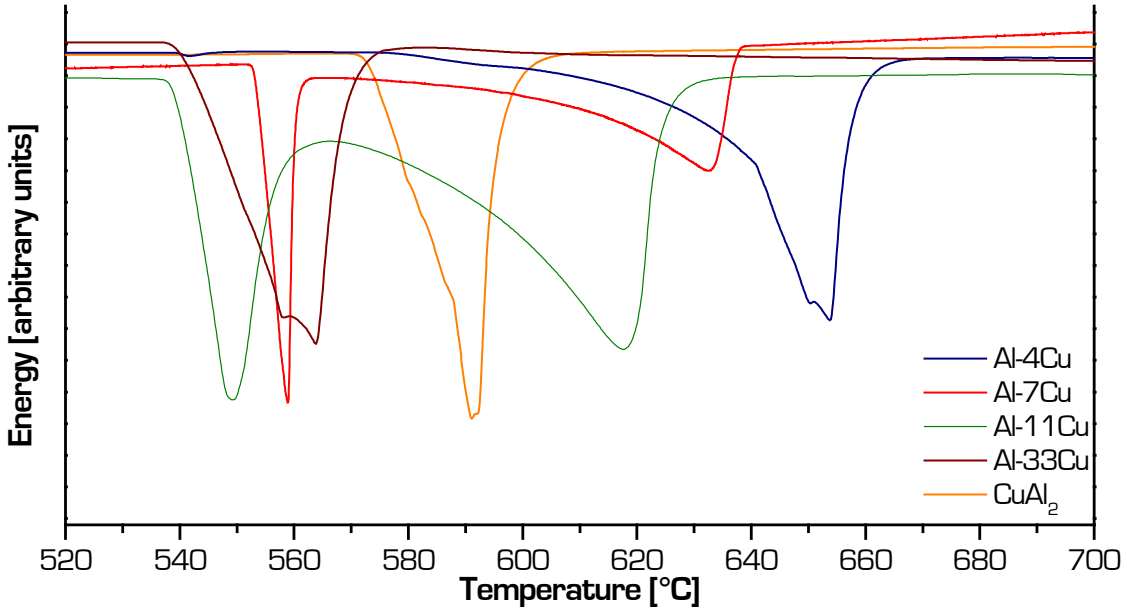


Figure 5.2: DSC curves of Al-4Cu, Al-7Cu, Al-11Cu, Al-33Cu, and $CuAl_2$

peaks or double peaks, which is typical of two-phase melting regions or near eutectic compositions, respectively.[92] $CuAl_2$ and pure aluminum show distinctive single-phase melting behaviour, while Al-33Cu, which should show an equally narrow and symmetrical melting peak, shows a slight double peak. This is evidence of the composition being just over 1wt.% hypo-eutectic.

Because Al-33Cu does not melt like a pure eutectic, the liquidus temperature is determined following the procedure for two-phase melting alloys described in section 4.3. From the DSC curves in Figures 5.1 and 5.2, the liquidus temperatures presented in Table 5.3 can be measured. For pure aluminum and for $CuAl_2$ respective melting temperatures of 660 °C and 591 °C were verified.

Table 5.3: Liquidus temperature of the investigated non-stoichiometric compositions

| Alloy | Al-11.5Si | Al-1Mg | A356 | AA6061 | Al-4Cu | Al-7Cu | Al-11Cu | Al-33Cu |
|---|---|---|---|---|---|---|---|---|
| $T_{liq}$ [°C] | 598 | 658 | 624 | 664 | 657 | 639 | 635 | 568 |

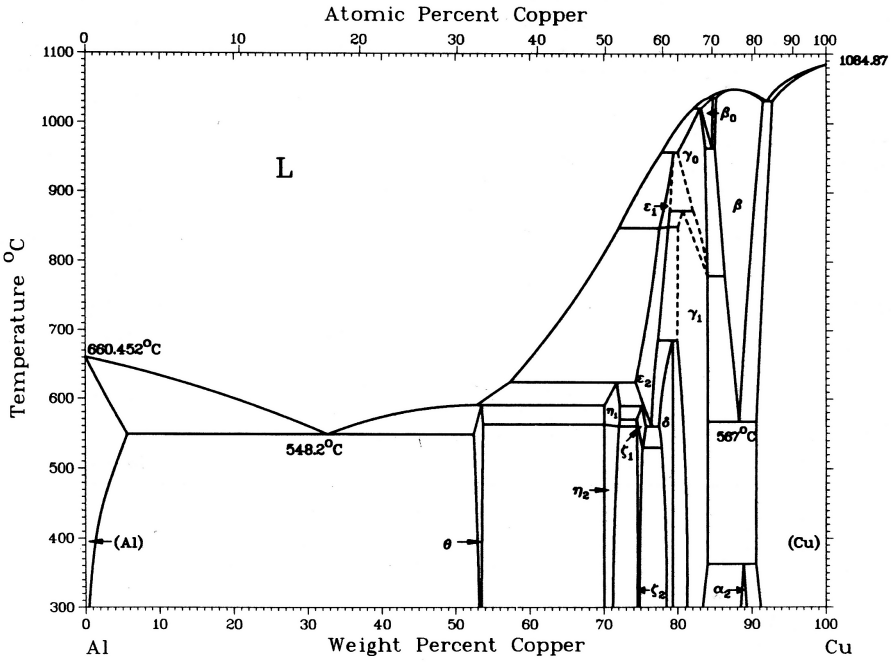


Figure 5.3: Al-Cu phase diagram

The determined liquidus temperatures correlate well to the corresponding equilibrium phase diagrams such as the Al-Cu phase diagram presented in Figure 5.3[97].

## 5.3 WETTING BEHAVIOUR

The discussion of the wetting results will be divided into three sub-sections: the wetting behaviour of pure aluminum, Al-11.5Si, Al-7Cu, Al-1Mg, A356, and AA6061 on alumina and on sapphire substrates, that of aluminum-copper alloys on sapphire, and finally the wetting of silicon carbide by all investigated metals.

### 5.3.1 Wetting Behaviour on Alumina and Sapphire

Contact angle measurements over time of pure aluminum on alumina and on A-plane sapphire obtained between 670°C and 800°C are presented in Figures 5.4 and 5.5. The graphs show that an equilibrium contact angle is usually reached immediately. As can be seen from the 700°C case on sapphire (Figure 5.5) occasionally the equilibrium contact angle materialized only within the first few minutes after a slight change. This occurred arbitrarily and was not related to a certain temperature or the one or the other substrate, as random repeats showed. In all cases, however, contact angles reached a constant value well within the 15-minute wetting tests. Thus, the value of the curve fit at 15 minutes can be considered the equilibrium contact angle and be plotted over the experimental temperature.

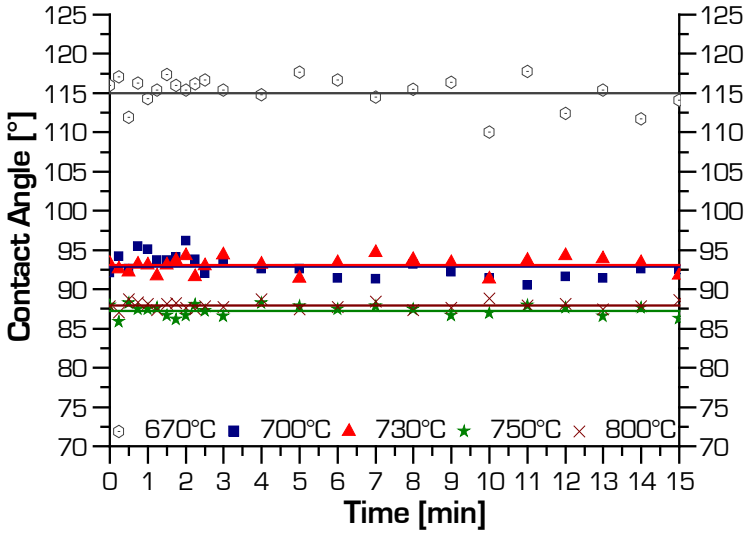


Figure 5.4: Contact angles vs. time for Al-99.99 on alumina

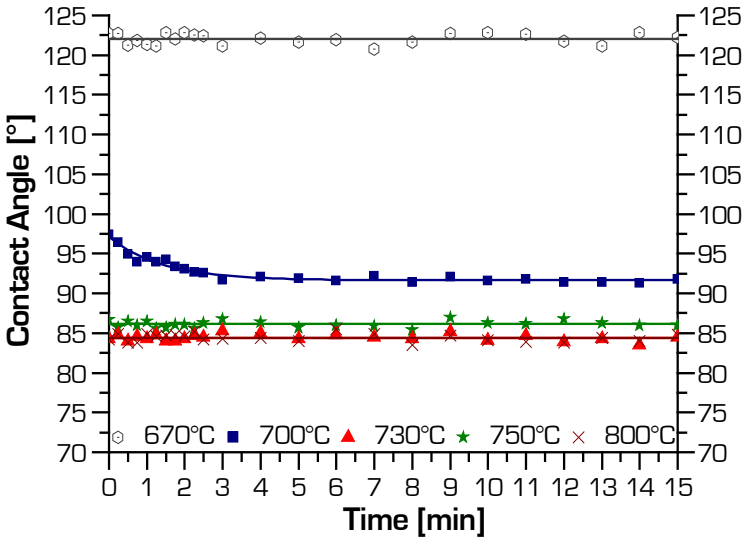


Figure 5.5: Contact angles vs. time for Al-99.99 on sapphire

From Figure 5.6, comparing equilibrium contact angles on polished alumina and A-plane sapphire, it is apparent that the wetting behaviour of pure aluminum on these two substrates is within experimental error identical, with the contact angle on sapphire usually being slightly lower.

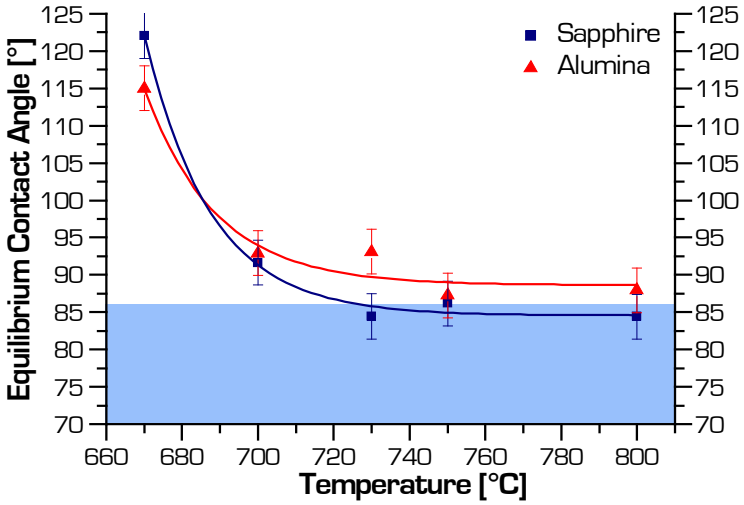


Figure 5.6: Wetting behaviour vs. temperature on alumina and sapphire substrates for Al-99.99; the area shaded in blue is the optimum contact angle range according to *KAPTAY*[12]

Furthermore, the equilibrium contact angles at 700°C are 91.6°±3° and 92.9°±3° on sapphire and alumina, respectively. This is in close correlation with data published in a number of previous studies[58-60], where a value of 90° for pure aluminum on sapphire was measured at 700°C using a vertical dispensed drop method setup (compare Table 2.1). This can be viewed as validation of the current experimental setup and methodology.

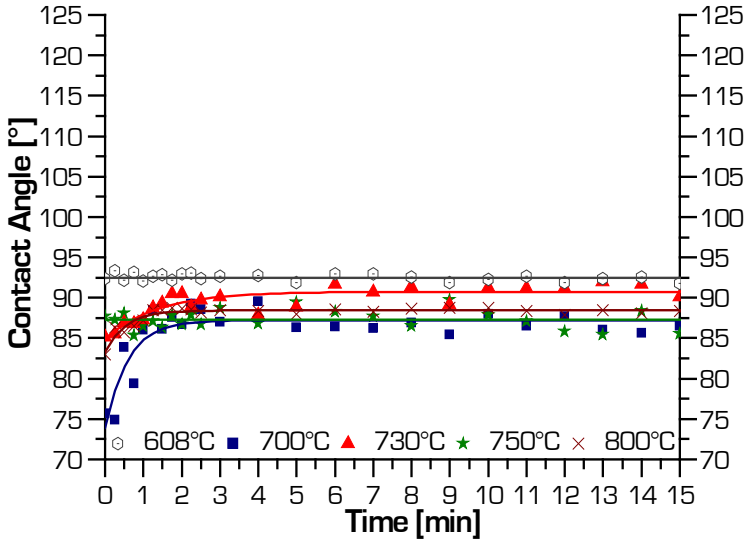


Figure 5.7: Contact angles vs. time for Al-11.5Si on alumina

The contact angle development with time of Al-11.5Si on alumina and sapphire is presented in Figures 5.7 and 5.8. Again, it can be seen that equilibrium contact angles are reached immediately in the case of most tests. However, similarly to the 700 °C plot of pure aluminum on A-plane sapphire, the 700 °C and 730 °C experiments of Al-11.5Si on both substrates show changing contact angles over the first 2 to 3 minutes before equilibrium is reached.

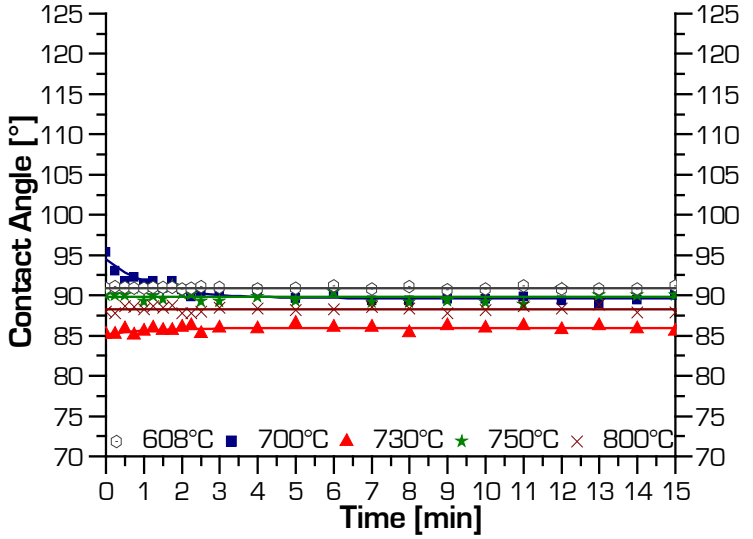


Figure 5.8: Contact angles vs. time for Al-11.5Si on sapphire

*Shen* et al.[98] explain such behaviour with the impingement of the drop on the substrate's surface. If the drop impingement is insufficient, the drop may continue to spread further over the first few minutes after injection. In the case of a slightly excessive dropping force, the drop may recede after being dispensed.

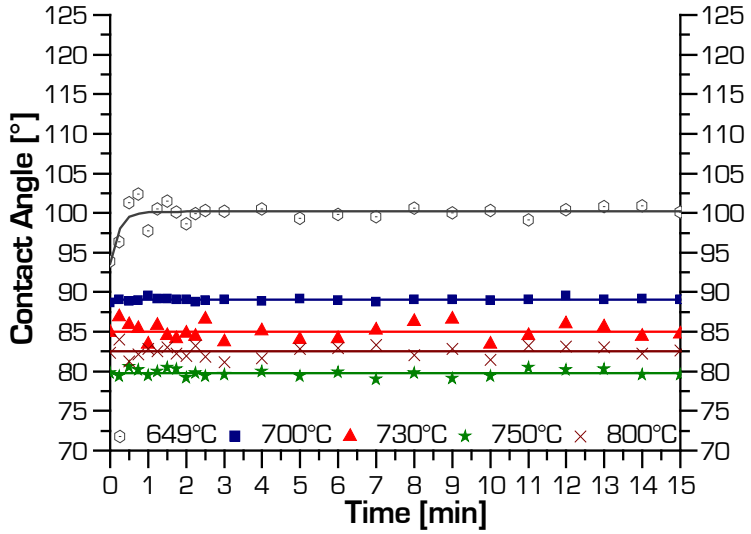


Figure 5.9: Contact angles vs. time for Al-7Cu on alumina

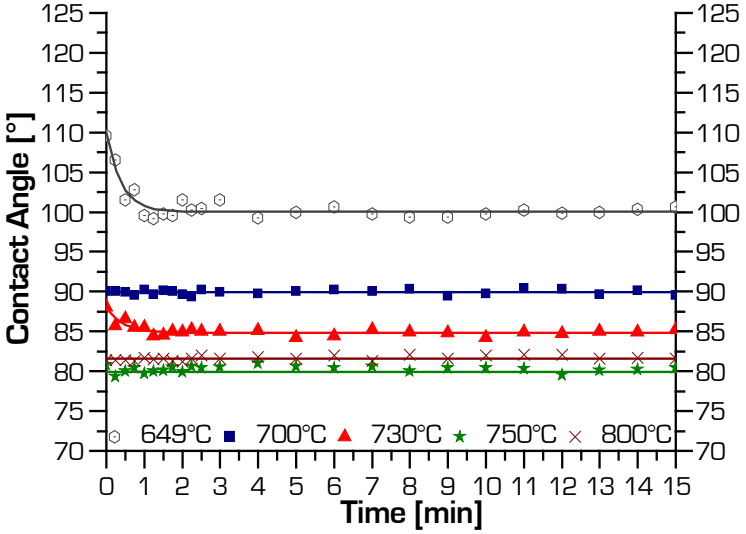


Figure 5.10: Contact angles vs. time for Al-7Cu on sapphire

The contact angle over time plots for Al-7Cu on alumina and sapphire are presented in Figures 5.9 and 5.10. Like in the case of the previously discussed alloy / substrate wetting systems, it is apparent that equilibrium contact angles in most experiments are reached immediately with the odd case where the alloy drop was ejected from the syringe with slightly excessive or insufficient force, resulting in retracting or increasing contact angles over the first 2 to 3 minutes.

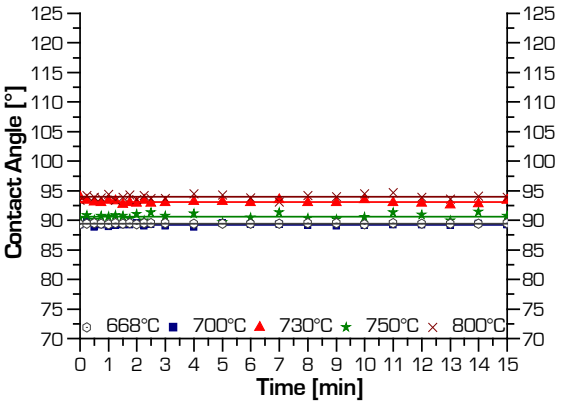


Figure 5.11: Contact angles vs. time for Al-1Mg on alumina

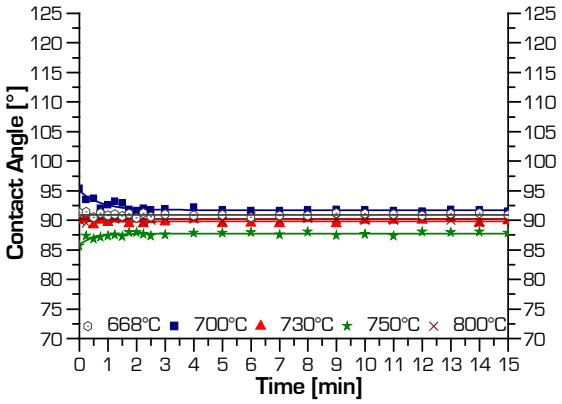


Figure 5.12: Contact angles vs. time for Al-1Mg on sapphire

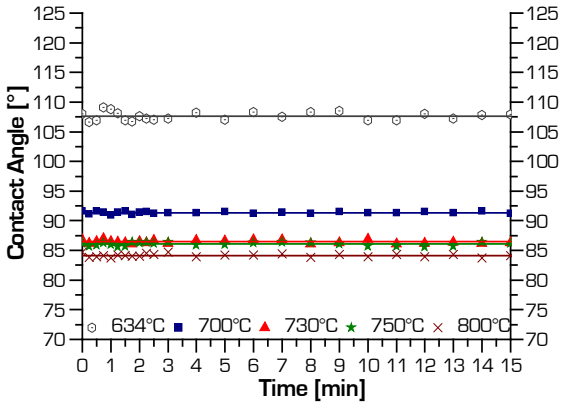


Figure 5.13: Contact angles vs. time for A356 on alumina

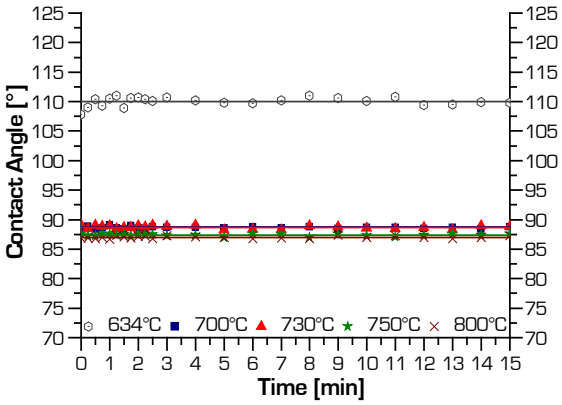


Figure 5.14: Contact angles vs. time for A356 on sapphire

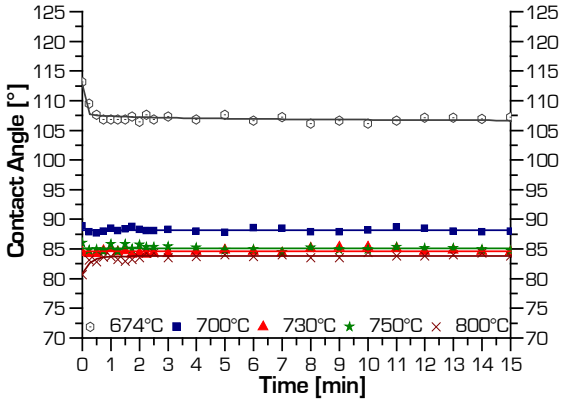


Figure 5.15: Contact angles vs. time for AA6061 on alumina

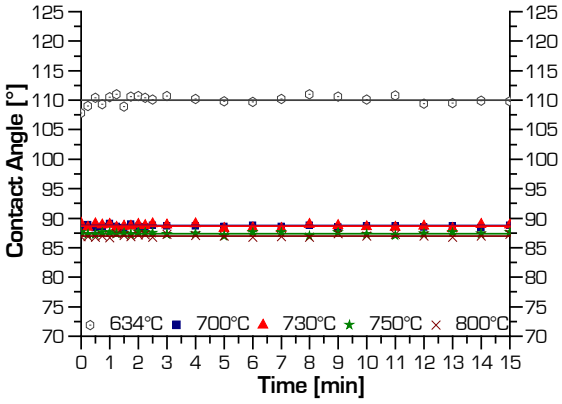


Figure 5.16: Contact angles vs. time for AA6061 on sapphire

The equivalent plots of contact angle evolution with time for Al-1Mg, A356, and AA6061 on alumina and sapphire are presented in Figures 5.11 to 5.16.

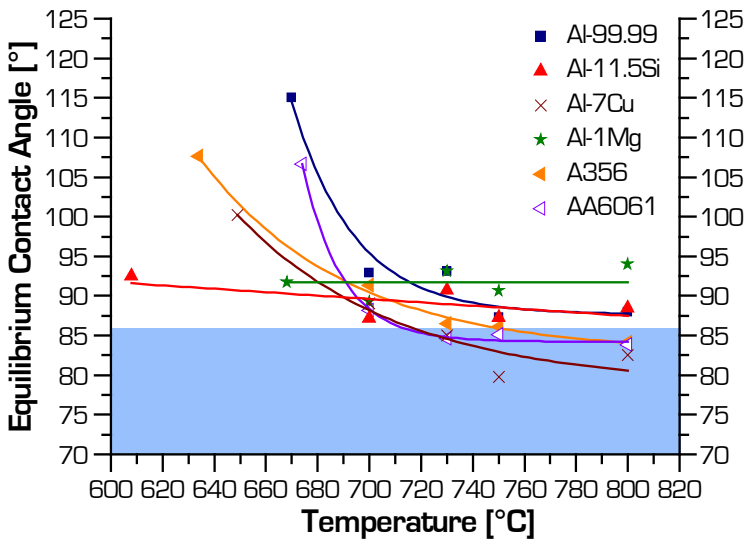


Figure 5.17: Wetting behaviour vs. temperature on alumina for Al-99.99, Al-11.5Si, Al-7Cu, Al-1Mg, A356, and AA6061

Figures 5.17 and 5.18 compare the equilibrium contact angles of the different alloys on alumina and sapphire, respectively. The area shaded in blue in the plots is the 70° to 86° contact angle range, which according to *KAPTAY*[12] should be most beneficial for ceramic particle induced aluminum (alloy) foam stabilization.

From these two diagrams, three facts are important to notice:

Al-99.99, Al-7Cu, A356, and AA6061 on the one hand and Al-1Mg, and Al-11.5Si on the other appear to have fundamentally different wetting behaviour on alumina and sapphire. While the former show a distinct and very significant increase in contact angle towards lower temperatures and in particular, towards the melting point or liquidus temperature of the metal, the latter exhibit a constant or only slightly declining wetting behaviour with temperature on both substrates. This is meaningful, as the wetting behaviour of the former systems changes from the wetting well into the non-wetting regime.

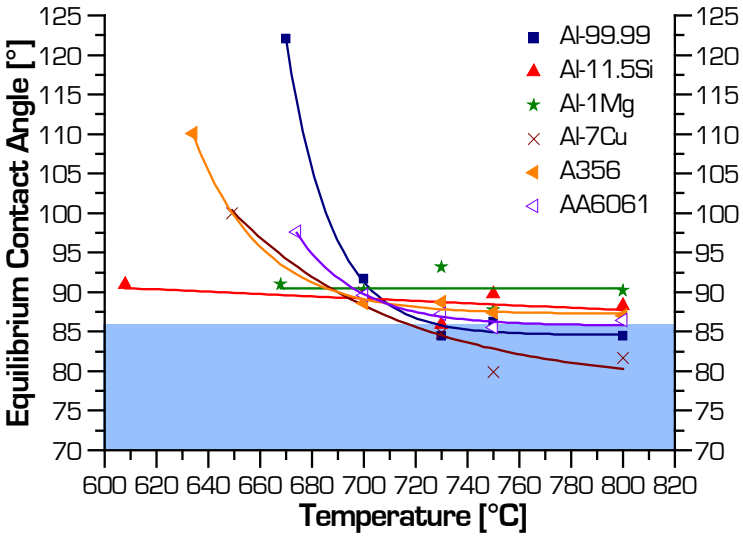


Figure 5.18: Wetting behaviour vs. temperature on sapphire for Al-99.99, Al-11.5Si, Al-7Cu, Al-1Mg, A356, and AA6061

Figures 5.17 and 5.18 furthermore show that not only pure aluminum but also the five alloys presented in the graphs exhibit wetting behaviours on alumina and sapphire, which are within experimental error alike. This almost identical wetting behaviour of the alloys on alumina and sapphire is no real surprise as wetting behaviour of a system free of contaminants, such as oxides, is most influenced by the surface energies, by the vapour phase, and by the surface roughness of the substrate. Since the vapour phase (high vacuum with reduced oxygen partial pressure) and the surface energy of the liquid are identical between two wetting tests with the same alloy on alumina and sapphire, and the surface roughness of both substrates is very comparable, the surface free energy of the substrates is the only factor, which may vary slightly between the two.

The surface free energy of flat surfaces itself is mostly influenced by the bonding type in the material, as well as the degree of (surface) deformation, and grain boundaries, as they are a source of decreased atomic order on the surface.[99-101] Temperature and pressure are influencing factors as well, but to lesser extent; moreover, based on the current experimental conditions they are identical for both substrates.

The chemical composition of alumina and sapphire is the same: $Al_2O_3$. The bonding type can therefore be assumed identical as well, with the limitation that the bond length varies in different crystallographic orientations. The degree of deformation can



be seen as negligible in both cases as the material is a ceramic and hence does not endure significant amounts of plastic deformation.

This leaves grain boundaries and crystallographic orientation being the only two factors distinguishing alumina and sapphire as substrates in the present wetting experiments. *SHEN* et al.[102] have reported differences in contact angle of liquid copper on different crystallographic orientations of sapphire of 1° to 3°. Other authors[53], however, suggest that such differences are hardly measurable. Therefore, it seems reasonable for the purpose of the present work to consider the wetting behaviour of the investigated alloys on sapphire and alumina to be identical.

The third, for this study important fact to note from Figures 5.16 and 5.17, is that only Al-7Cu and AA6061 comfortably reach the contact angle range suggested to be most beneficial for metal foam stabilization,[12] while pure aluminum and A356 only just reach the range on the one substrate but not on the other. All, however, reach the 70° to 86° contact angle range only at higher temperatures and transition well into the non-wetting regime just before solidification, as described earlier.

After the wetting experiments, the solidified drops showed good adhesion on both substrates.

### 5.3.2 Wetting of Aluminum-Copper Alloys on Sapphire

The finding that 7wt.% copper addition to aluminum causes a slight but significant decrease in contact angle of several degrees, behaves contrary to the thermodynamic model for non-reactive liquid alloy / oxide ceramic substrate wetting systems developed by *LI* et al.[63] As described in section 2.2.5 the model predicts that small additions of copper to aluminum should have hardly any effect on the contact angle and rather cause an increase than a decrease, since copper is not a surface active element in aluminum according to *LANG*.[103,104]

In order to clarify the disagreement between the wetting data presented above and the model of *LI* et al.[63], a series of aluminum-copper alloys ranging from 4wt.% copper addition to the intermetallic composition $CuAl_2$ (53wt.% Cu) were investigated regarding their wetting behaviour on $Al_2O_3$. As has been explained above, the wetting behaviour on alumina and sapphire is considered identical. Therefore, these experiments were conducted on sapphire only, as the surface roughness of the sapphire substrate is more controlled (no pulled-out grains).

The contact angles versus time graphs for the aluminum-copper alloys on A-plane sapphire obtained between 10°C above the melting or respective liquidus temperatures and 800°C are presented in Figures 5.19 to 5.22. Again, it can be seen that each experiment reaches a constant contact angle within a very short time after the drop has been dispensed on the substrate and well before the experiments were concluded after 15 minutes. The changes in contact angle over the first few minutes in some cases can again be explained following *SHEN* et al.[98]

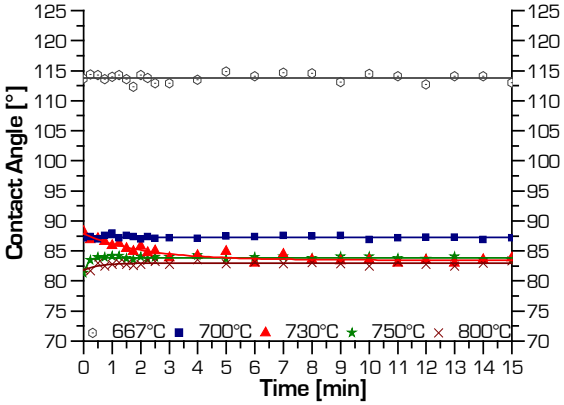


Figure 5.19: Contact angles vs. time for Al-4Cu on sapphire

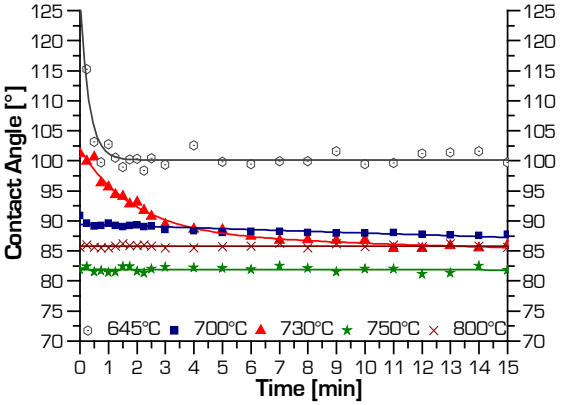


Figure 5.20: Contact angles vs. time for Al-11Cu on sapphire

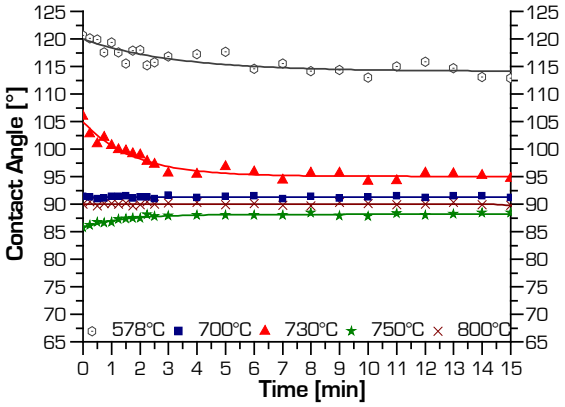


Figure 5.21: Contact angles vs. time for Al-33Cu on sapphire

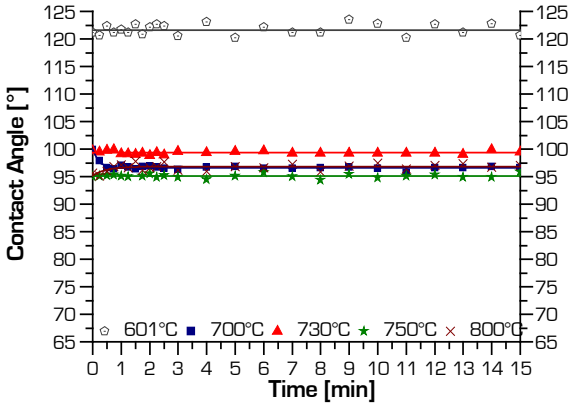


Figure 5.22: Contact angles vs. time for $CuAl_2$ on sapphire

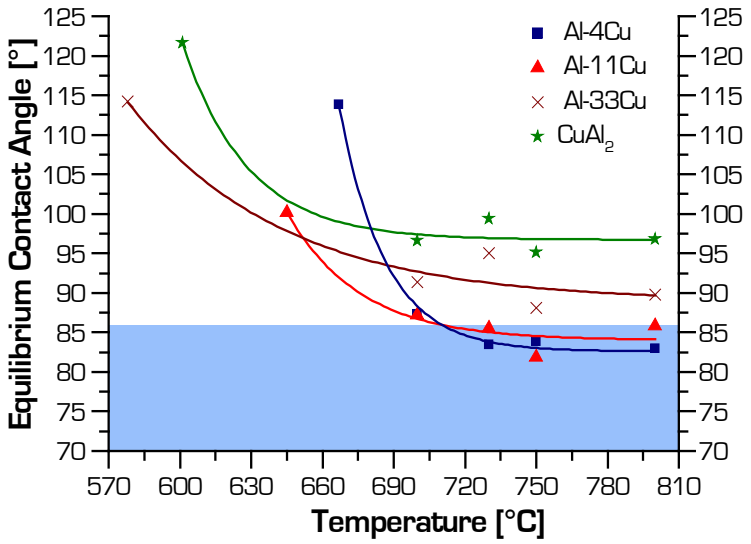


Figure 5.23: Wetting behaviour vs. temperature on sapphire for Al-4Cu, Al-11Cu, Al-33Cu and $CuAl_2$

In Figure 5.23 the wetting behaviour of the additional aluminum-copper alloys on sapphire is presented. It can be seen, that these additional alloys in general behave similar to pure aluminum and Al-7Cu on $Al_2O_3$, transitioning well into the non-wetting regime when the liquidus temperature or the melting point is approached. At higher temperatures, the equilibrium contact angles seem to asymptotically approach a threshold.

If the equilibrium contact angles are not plotted over the experimental temperature but over the copper content in the alloy (Figure 5.24), it can be seen that all curves show a minimum contact angle between approximately 7wt.% and 12wt.% copper with the values for Al-7Cu nicely fitting into the same range.

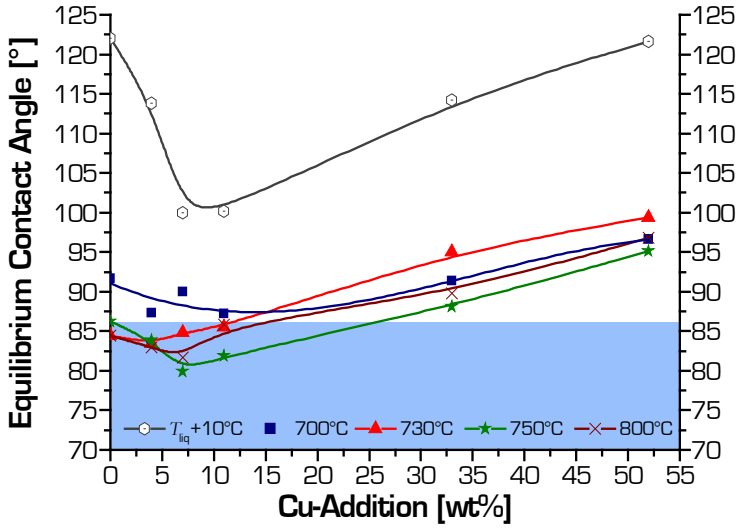


Figure 5.24: Equilibrium contact angles vs. copper content

After the wetting experiments, the aluminum-copper alloys showed generally good adhesion on the sapphire substrates. Solidified drops of Al-7Cu and Al-33Cu had such good adhesion that upon cooling or subsequent sample preparation several of them fractured off the substrates with a piece of sapphire from immediately underneath the drop still being attached to the alloy, thus leaving a pit in the ceramic. Although this is rather evidence of intense residual stresses being induced at the interface due to significantly different coefficients of thermal expansion and cooling rates that do not allow sufficient relaxation to take place, this fact still demonstrates a very strong interface, as the fracture does not occur along the interface but rather through the single crystal.

Drops of $CuAl_2$ always fell off the substrate after the wetting test and before the samples reached room temperature. The fracture occurred along the interface or inside the alloy, frequently leaving small islands of alloy attached to the sapphire. This is considered strong evidence of both significantly different thermal expansion coefficients between alloy and substrate as well as brittleness of the intermetallic.

In order to determine the reason for the wetting behaviour deviating from the model by Li et al.[63], interface investigations were conducted.

*Levi* and *Kaplan* found in their standard sessile drop experiments with pure aluminum on sapphire that a reduction in contact angle occurred from the non-wetting regime to



that of partial wetting with increasing temperature and time. They established that a reduction in solid-vapour and liquid-vapour surface energies, $\sigma_{SV}$ and $\sigma_{LV}$, alone cannot account for the observed transition but that the main reason is the decrease in aluminum / sapphire interface energy, $\sigma_{SL}$, caused by a significantly increased oxygen activity along the interface.[66,68]

Similarly to the case *LEVI* and *KAPLAN* describe[68], for the current case too, it can be assumed that the observed reduction in contact angle with copper content for small amounts of copper addition is due to a reduction in solid-liquid interface energy, $\sigma_{SL}$. This is because the liquid-vapour surface energy, $\sigma_{LV}$, of liquid copper is higher than that of liquid aluminum,[105] and because the solid-vapour surface energy, $\sigma_{SV}$, is almost the same for the different alloys, as substrate, and temperature are the same, and the atmosphere or vapour phase are essentially identical.

#### 5.3.2.1 Microscopy and Microanalysis

In order to observe possible reaction products at the interface, long-term wetting experiments were conducted on sapphire at 750 °C for 65 hours with pure aluminum, Al-7Cu, and $CuAl_2$ only, as these three alloys represent the three extremes with respect to the wetting behaviour of aluminum-copper alloys on sapphire.[f]

Figure 5.25 shows an SEM micrograph of an Al-7Cu / sapphire long-term wetting experiment after most of the solidified drop has been removed using a 20wt.% NaOH in water solution. It can be seen that on the left hand side some alloy remained on the interface. Where the interface that used to be underneath the drop is visible, very noticeable surface roughness can be observed, revealing distinct linear grooves.

[f] The final contact angles observed at the end of these (and other) long-term experiments did not deviate from the equilibrium contact angles measured after 15 minutes.

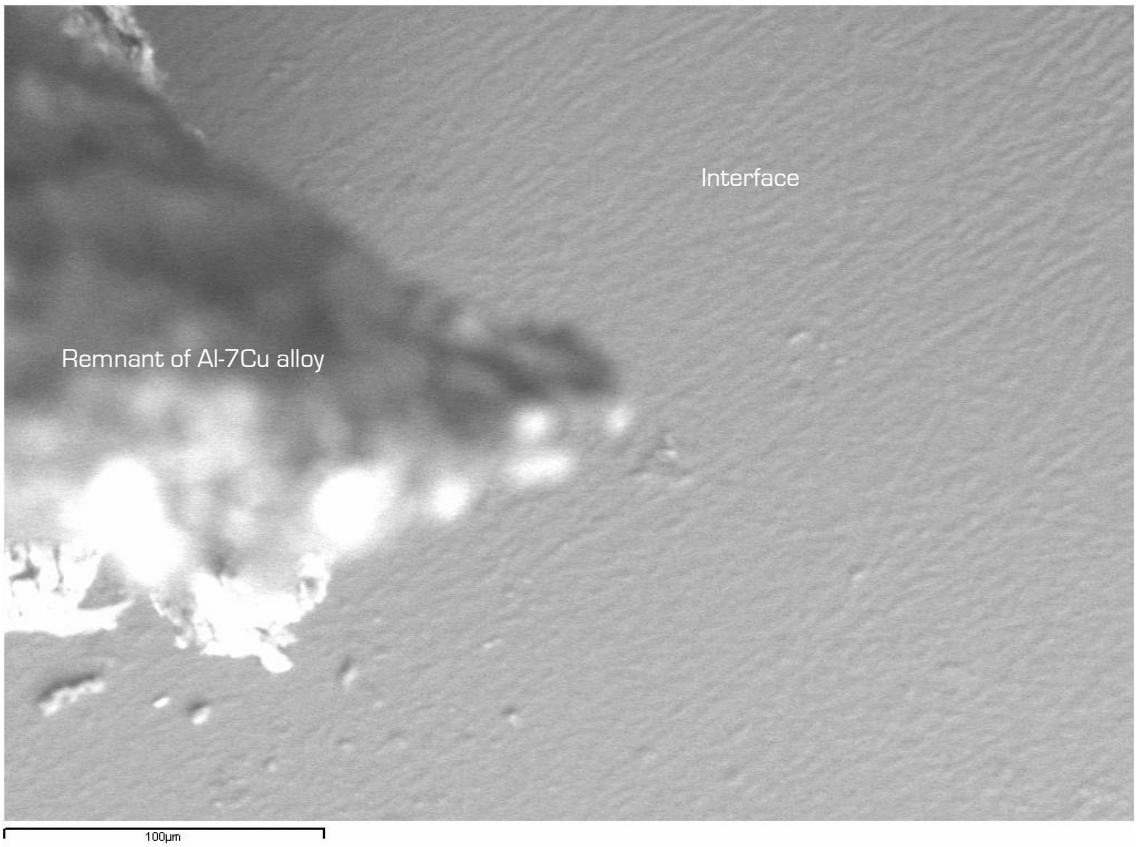


Figure 5.25: SEM top-view micrograph of Al-7Cu / sapphire long-term wetting experiment after most of the solidified drop has been removed chemically.

Although on their own inconclusive, EDS maps of the area were collected (Figures 5.26). From Figure 5.26 a), showing the EDS map where aluminum x-rays originate, it can be seen that aluminum is present both in the sapphire substrate as well as in the remnant Al-7Cu alloy. The apparent reduction in x-ray counts in the bottom left corner of the map is due to a shading effect by the remnant drop. The x-ray detector is located on the top left corner of the image. Therefore, x-rays generated on the other side of the leftover alloy cannot be collected by the detector as they are absorbed by the metal. The intense pink area on part of the alloy is caused by the fact that the leftover drop faces directly towards the detector causing increased peak counts. Similarly, Figure 5.26 b) shows the EDS map for oxygen. It can be seen that the highest oxygen counts are obtained from the sapphire substrate material ($Al_2O_3$). Oxygen x-ray counts are also detected from the remnant alloy, which is caused by the

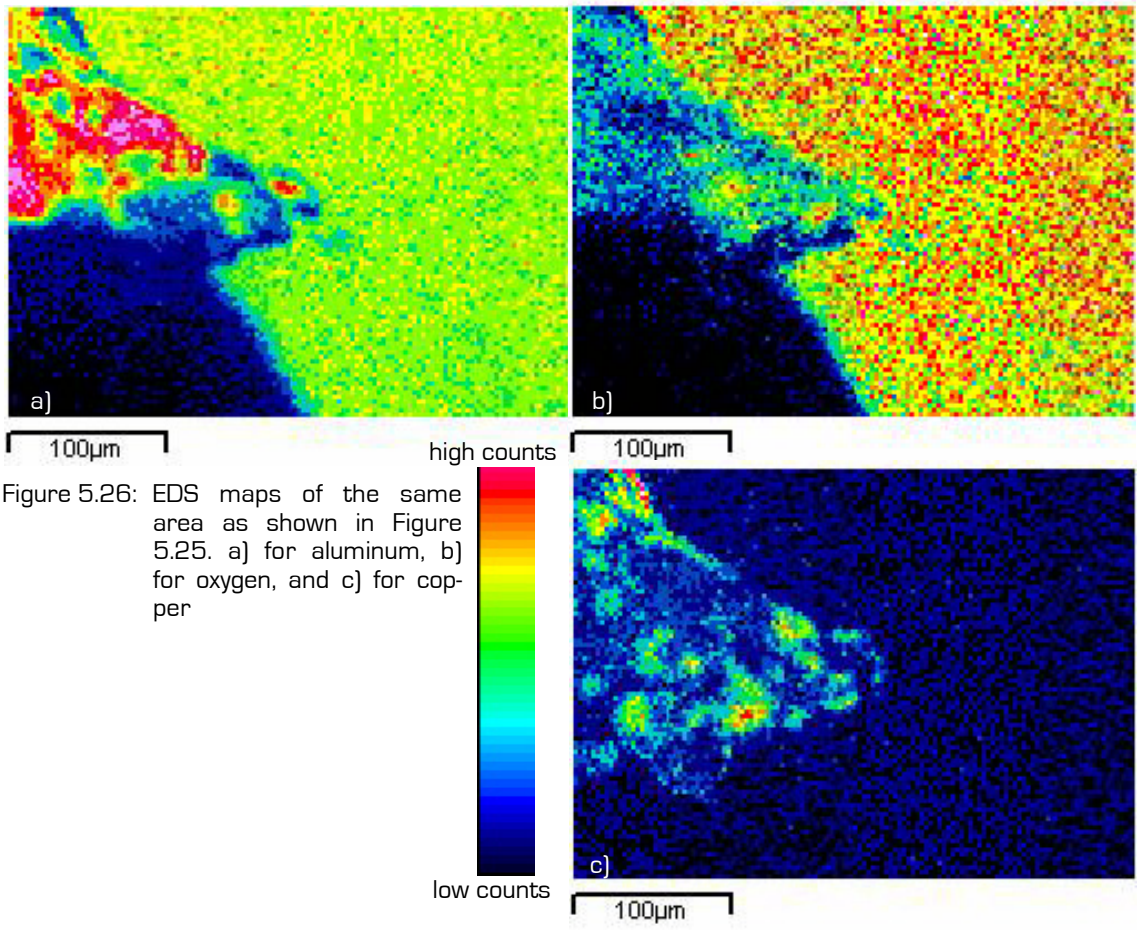


Figure 5.26: EDS maps of the same area as shown in Figure 5.25. a) for aluminum, b) for oxygen, and c) for copper

fact that the alloy surface oxidized after the sample has been removed from the wetting furnace. Again, the bottom-left corner is shaded from the detector by the leftover drop. In Figure 5.26 c) one can see that copper x-ray counts are predominately detected from the remnant alloy. However, low copper x-ray counts are also detected from the interface area where the solidified drop has been removed.

Together with the apparently increased surface roughness this is an indication that indeed a chemical reaction occurs during the wetting experiments.

#### 5.3.2.2 Thermodynamic Modeling

In order to get an estimate of the oxygen partial pressure inside the wetting furnace, the *ELLINGHAM* diagram[106] (Figure 5.27) was initially consulted. Based on the presence of titanium sponge and the graphite syringe in the hot-zone of the furnace, one can obtain an oxygen partial pressure of approximately $10^{-21}$mbar for the equilibrium of

$$2\,C + O_2 \leftrightarrows 2\,CO \qquad \text{Eq. 5.1}$$

at 750°C and about $10^{-45}$mbar for the

$$Ti + O_2 \leftrightarrows TiO_2 \qquad \text{Eq. 5.2}$$

equilibrium at the same temperature. Since, however, the system is in a steady-state vacuum condition, which means that the vacuum pump is constantly running during the experiment in order to maintain the overall pressure, it must be assumed that a very minute, yet constant stream of air is leaking into the vacuum system and past the experiment (mainly through the connectors). Therefore, an initial estimation of the oxygen partial pressure in the system of $10^{-21}$mbar to $10^{-30}$mbar seemed appropriate.

Later, FactSage's *EQUILIB* function was used to verify whether the original estimate was reasonable. For this simulation, the following information was used: On the observation port side of the ceramic substrate in the hot-zone of the furnace are approximately 10g of titanium sponge. This is equivalent to 0.21mol of titanium. With the syringe, which weighs about 25g, there is 2.08mol of carbon in form of graphite in the furnace. The initial oxygen partial pressure (prior to the reactions with titanium and graphite) can be calculated to $1.21 \cdot 10^{-13}$mbar (evacuation of the system to $10^{-6}$mbar overall pressure, followed by purging with pre-purified argon fed through

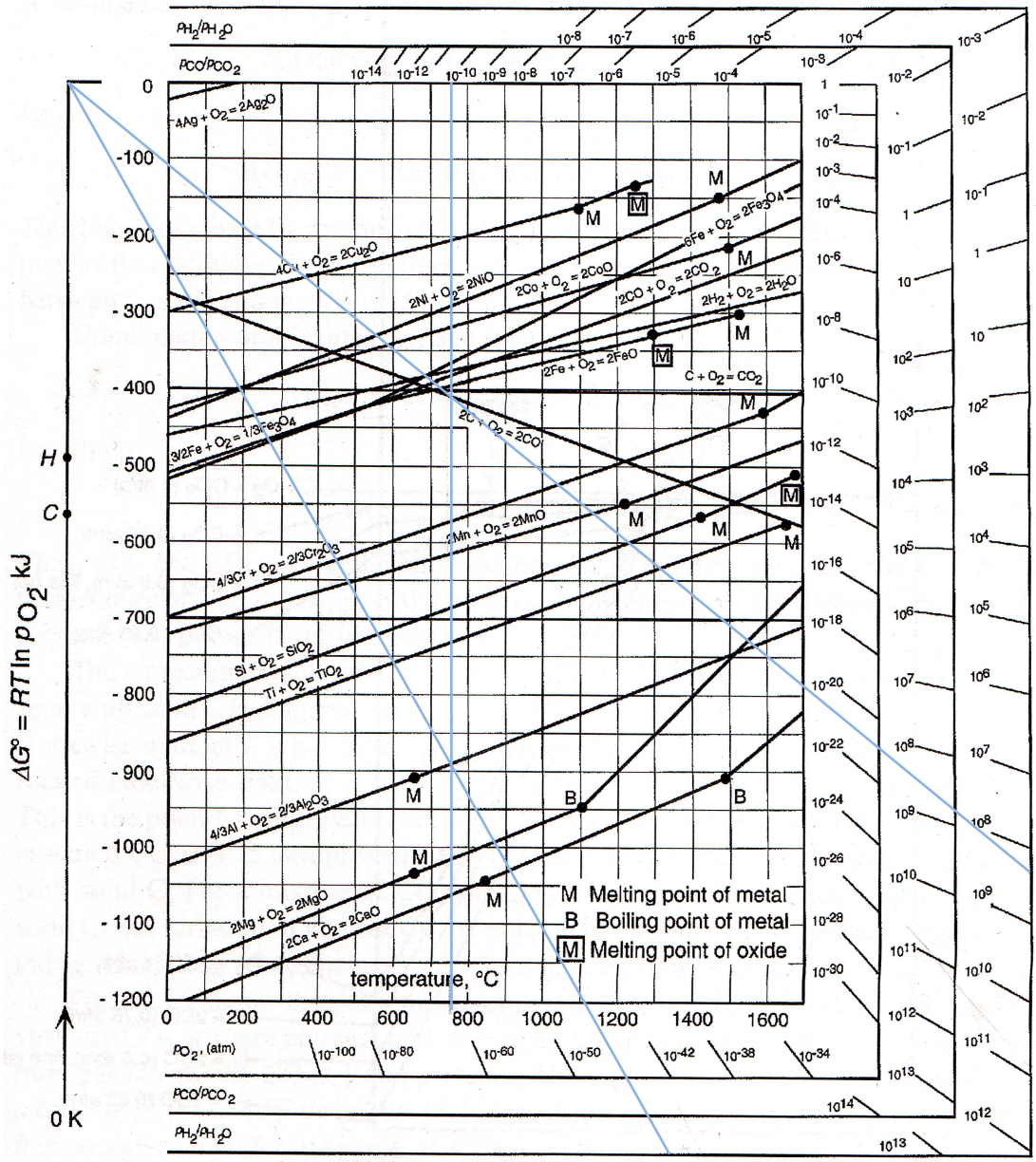


Figure 5.27: *ELLINGHAM* diagram, from which for a given temperature the equilibrium oxygen partial pressure of a given reaction can be obtained: The vertical construction line corresponds to the 750°C. The diagonal construction lines originate in 0 K and pass through the point where the equilibrium line for the two relevant reactions intersects the vertical construction line. The values at which these diagonal construction lines intersect the $p(O_2)$ scale represent the equilibrium oxygen partial pressures for the relevant reactions.

an oxygen and moisture trap to 1bar overall pressure, and re-evacuation to $10^{-6}$mbar; the oxygen and moisture trap reduces the oxygen content in the argon gas to 1ppb). In the vacuum system, which contains a volume of $3.45 \cdot 10^{-3}m^3$, this gives approximately $5.02 \cdot 10^{-18}$mol of oxygen at 750°C. After equilibrium between the three reactants (oxygen, titanium, and graphite) is achieved at 750°C, $1.46 \cdot 10^{-26}$mbar of oxygen are left according to FactSage.

As this value lies nicely within the original estimate, the range of $10^{-21}$mbar to $10^{-30}$mbar is valid.

Table 5.4: Activities of Al and Cu in the liquid alloy for different compositions as modeled by FactSage

| **Composition [wt.% Cu]** | $a(\mathbf{Al}_{liq})$ | $a(\mathbf{Cu}_{liq})$ |
|---|---|---|
| 0 | 1.00000 | 0.00000 |
| 5 | 0.97819 | 0.00030 |
| 10 | 0.95484 | 0.00063 |
| 15 | 0.92928 | 0.00099 |
| 20 | 0.90063 | 0.00140 |
| 25 | 0.86780 | 0.00189 |
| 30 | 0.82943 | 0.00250 |
| 35 | 0.78390 | 0.00330 |
| 40 | 0.72943 | 0.00437 |
| 45 | 0.66424 | 0.00589 |
| 50 | 0.58696 | 0.00812 |
| 55 | 0.49734 | 0.01154 |
| 60 | 0.39727 | 0.01704 |

In order to identify possible reactions leading to the observed surface roughness as well as to the described reduction in solid-liquid surface energy, $\sigma_{SL}$, a second set of simulations was carried out. Table 5.4 shows the activities[g][106] of aluminum and

[g] Activity is the thermodynamic quantity that describes the effective concentration of en element in an alloy.



copper in a liquid aluminum-copper alloy at 750°C depending on copper addition as calculated by FactSage's *EQUILIB* Function.

Using the program's *REACTION* function a number of chemical reactions that might be possible under the given experimental conditions were modeled in order to obtain values for the standard Gibbs free energy of formation, $\Delta G^0$, of the various reaction products:

$$2\,Cu + {}^1/_2\,O_2 \rightarrow Cu_2O; \quad \Delta G^0 = -93.9kJ \qquad \text{Eq. 5.3}$$

$$Al_2O_3 + {}^1/_2\,O_2 + 2\,Cu \rightarrow Cu_2Al_2O_4; \quad \Delta G^0 = -107.0kJ \qquad \text{Eq. 5.4}$$

$$Al_2O_3 + {}^1/_2\,O_2 + Cu \rightarrow CuAl_2O_4; \quad \Delta G^0 = -188.3kJ \qquad \text{Eq. 5.5}$$

$$2\,Al + 2\,O_2 + 2\,Cu \rightarrow Cu_2Al_2O_4; \quad \Delta G^0 = -1460.7kJ \qquad \text{Eq. 5.6}$$

$$2\,Al + 2\,O_2 + Cu \rightarrow CuAl_2O_4; \quad \Delta G^0 = -1542.1kJ \qquad \text{Eq. 5.7}$$

$$2\,Al + {}^3/_2\,O_2 \rightarrow Al_2O_3; \quad \Delta G^0 = -1353.7kJ \qquad \text{Eq. 5.8}$$

With this information, the minimum oxygen partial pressure required for these reactions to occur can be calculated using the equilibrium constant $K$ of each reaction and the equation:

$$\Delta G^0 = -R \cdot T \cdot \ln K, \qquad \text{Eq. 5.9}$$

where R is the ideal gas constant, and $T$ the absolute temperature at which the reaction takes place. The equilibrium constant of the reaction in Equation 5.3 for example is:

$$K = \frac{a(Cu_2O)}{a(Cu_{liq})^2 \cdot \sqrt{p(O_2)}} \qquad \text{Eq. 5.10}$$

Replacing $K$ in Equation 5.9 with Equation 5.10 and solving for the partial pressure of oxygen leads to:

$$\Delta G^0 = -\mathrm{R} \cdot T \cdot \ln \frac{a(\mathrm{Cu_2O})}{a(\mathrm{Cu_{liq}})^2 \cdot \sqrt{p(\mathrm{O_2})}} \qquad \text{Eq. 5.11}$$

$$p(\mathrm{O_2}) = \left( e^{\frac{\Delta G^0}{\mathrm{R} \cdot T}} \cdot \frac{a(\mathrm{Cu_2O})}{a(\mathrm{Cu_{liq}})^2} \right)^2 \qquad \text{Eq. 5.12}$$

As the temperature can be fixed at 750°C (1023K), as this the temperature at which the long-term experiments were conducted, and since the activity of $Cu_2O$ is unity because it is a pure solid, Equation 5.12 becomes a function only of the copper activity in the liquid aluminum-copper alloy. Similar solutions can be found for the other modeled reactions in Equations 5.4 to 5.8. Consequently, the oxygen partial

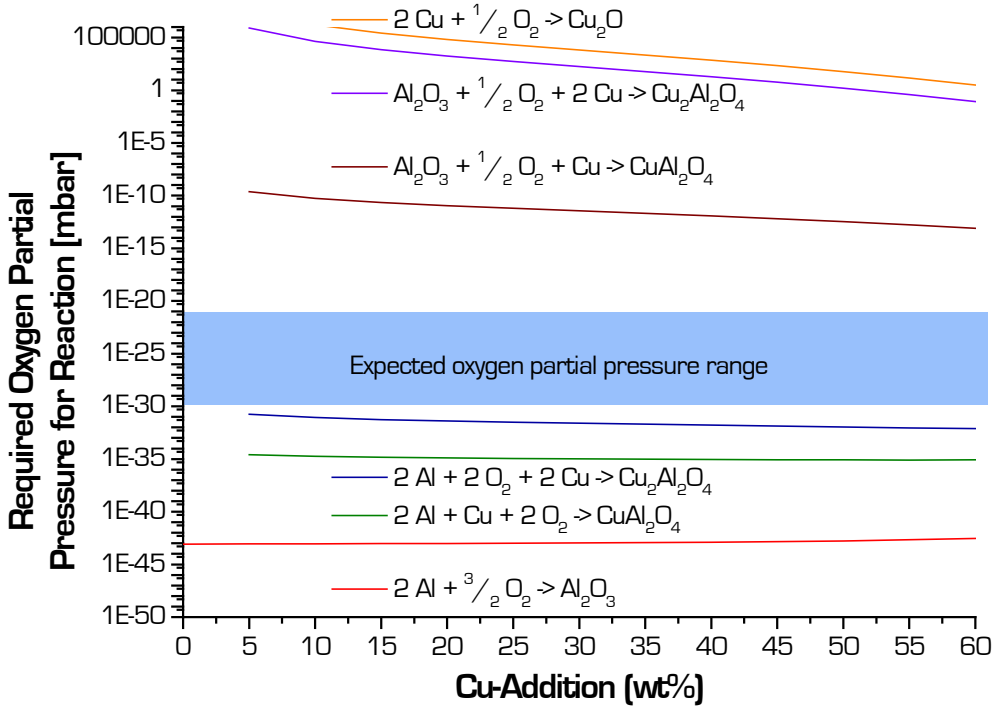


Figure 5.28: Required oxygen partial pressure for the different modeled reactions to occur based on the copper addition to aluminum



pressure required for the various modeled reactions to occur can be plotted over the copper addition to aluminum (Figure 5.28).

The range of the experimental oxygen partial pressure expected in the chamber of $10^{-21}$mbar to $10^{-30}$mbar is shown shaded in blue in the plot. It can be seen that the direct oxidation of copper to form $Cu_2O$ according to Equation 5.3 would not only require very high oxygen partial pressures, the standard Gibbs free energy of formation of this reaction is the least negative of all suggested reactions. Similarly, the two suggested direct reactions of copper in the alloy with the sapphire substrate in Equations 5.4 and 5.5, require oxygen partial pressures higher than that expected to be available inside the experimental chamber. Although the standard Gibbs free energy of formation of Equations 5.4, and particularly 5.5, are already more negative than that of the simple oxidation of copper, they are still approximately one order of magnitude larger than the reaction of the liquid with residual oxygen from the furnace atmosphere to form the spinels $Cu_2Al_2O_4$, and $CuAl_2O_4$ in the case of aluminum-copper alloys, or $Al_2O_3$ in the case of pure aluminum. Disregarding the higher than expected oxygen activities along the interface as suggested by *Levi* et al.[65,66] only the reactions in Equations 5.6 to 5.8 are thermodynamically possible at the estimated oxygen partial pressure in the vacuum furnace, as their requirement for oxygen is lower than what is available in the system.

Since the respective standard Gibbs free energies of formation of the reactions in Equations 5.6 to 5.8 are somewhat similar, it can be assumed that they can all occur simultaneously based on the availability of copper in the alloy.

A third set of FactSage simulations was concerned with the question posed by *Levi* et al.[66] regarding the nature of the high oxygen activity presumed at the interface (whether it is actually oxygen at the interface or whether an oxygen-rich Al-O inter-phase such as $Al_2O$ forms there). In an attempt to answer this question, the standard

Gibbs free energies of the following reactions were calculated using the program's *REACTION* function:

$$3\,Cu + 4\,Al_2O_3 \rightarrow 3\,CuAl_2O_4 + 2\,Al \qquad \text{Eq. 5.13}$$

$$6\,Cu + 4\,Al_2O_3 \rightarrow 3\,Cu_2Al_2O_4 + 2\,Al \qquad \text{Eq. 5.14}$$

For the sake of modeling, these include the possibility of liquid aluminum reacting with the sapphire along the interface to form gaseous $Al_2O$ according to the reaction

$$4\,Al + Al_2O_3 \rightarrow 3\,Al_2O^{\uparrow} \qquad \text{Eq. 5.15}$$

as one step of a multi-step reaction with the overall reaction formulae in Equations 5.13 and 5.14, respectively. FactSage calculates a $\Delta G^0$=788.8kJ for the reaction in Equation 5.13 and $\Delta G^0$=1033.8kJ for that in Equation 5.14. It should be noted that both reactions are independent of the oxygen partial pressure in the furnace. Based again on the activities of aluminum and copper in the liquid aluminum-copper alloys the Gibbs free energy change, $\Delta G$, of the reactions at 750°C can be calculated from

$$\Delta G = \Delta G^0 + R{\cdot}T{\cdot}\ln K \qquad \text{Eq. 5.16}$$

Since the term $R{\cdot}T{\cdot}\ln K$ is positive for both reactions and all modeled alloys, $\Delta G$ remains large and positive. This means that both reactions are thermodynamically very unlikely to occur. Therefore, an oxygen-rich Al-O interphase cannot be the reason for the formation of a reaction product at the interface based on thermodynamic modeling.

#### 5.3.2.3 Interface Characterization

In order to verify whether the above-modeled reactions occur, AFM, HRTEM, FE-SEM, and XPS work were conducted. However, since the $CuAl_2$ drops fell off the substrates

during cooling, interface imaging using HRTEM was possible for pure aluminum and Al-7Cu on sapphire only.

*5.3.2.3.1 Atomic Force Microscopy*

In order to verify the SEM observation (Figure 5.25) of an increased roughness of the interface after long-term wetting experiments, the surface roughness was measured on samples of the three long-term wetting experiments. Surface roughness profiles of the interface were acquired by stitching subsequent 60µm by 60µm scanning areas from the triple line to the center of the interface. From the AFM scans, the surface roughness was measured by integration over 10µm by 10µm panes in the center of each scan (Figure 5.29).

The plot clearly shows significantly decreasing surface roughnesses along the radius from the outside in, in all three cases. It can also be seen that the surface roughness de-creases from pure aluminum to the intermetallic composition. All three curves show an asymptotical behaviour towards the center and remain significantly above the surface roughness of the substrate outside the drops, which other than the reaction with the drop underwent the same conditions as the interface underneath the liquid metal (i.e. heat cycle and NaOH treatment). This indicates the formation of the $Al_2O_3$ or spinel reaction products as modeled in Equations

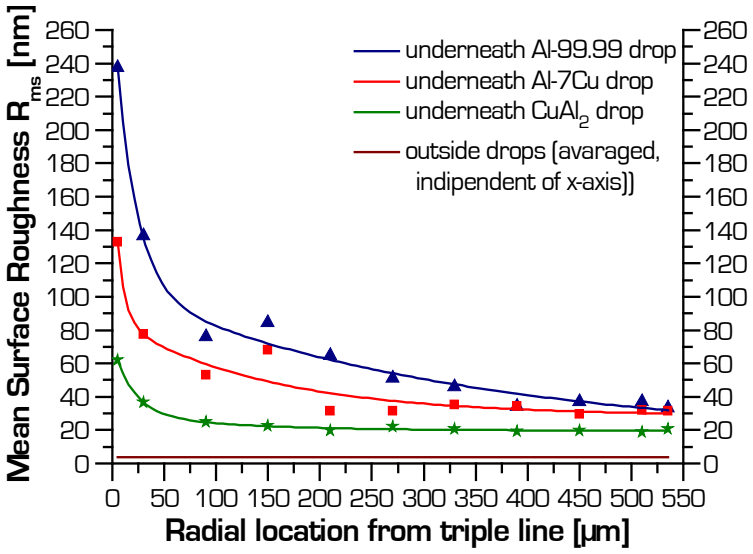


Figure 5.29: Surface roughness profile of the interface of the long term experiments Al-99.99 / sapphire, Al-7Cu / sapphire, and $CuAl_2$ / sapphire after 65 hours in comparison to the unreacted substrate

5.6 to 5.8 in section 5.3.2.2.

The decrease in interface roughness and significant reduction in precipitation density, and thus rate of reaction, from Al-99.99 / sapphire to Al-7Cu / sapphire does not conflict with the improved wetting, as the latter is caused by the precipitates being spinel rather than $Al_2O_3$. The reduction in rate of precipitation from pure aluminum to the $CuAl_2$ intermetallic can be explained with oxygen transport capacities of the interface, which (similarly to the findings of *Saiz* et al.[77]) are expected to be different depending on chemical composition of the alloy. Furthermore, the reduced precipitation rate from Al-7Cu / sapphire to $CuAl_2$ / sapphire likely plays a role in the decreased wetting as the beneficial effect of the spinel formation at the interface is weakened. However, the transition of the wetting behaviour into the non-wetting regime must be explained with an increasing liquid-vapour surface energy, $\sigma_{LV}$, of the liquid alloy with rising copper contents.

Furthermore, the AFM micrograph in Figure 5.30 of a $CuAl_2$ / sapphire long-term experiment reveals that scratches in the surface of the unreacted substrate become more pronounced under the sessile drop after the experiment. In addition to causing precipitates, the liquid alloy appears to act as an etchant on the sapphire surface, revealing asperities.

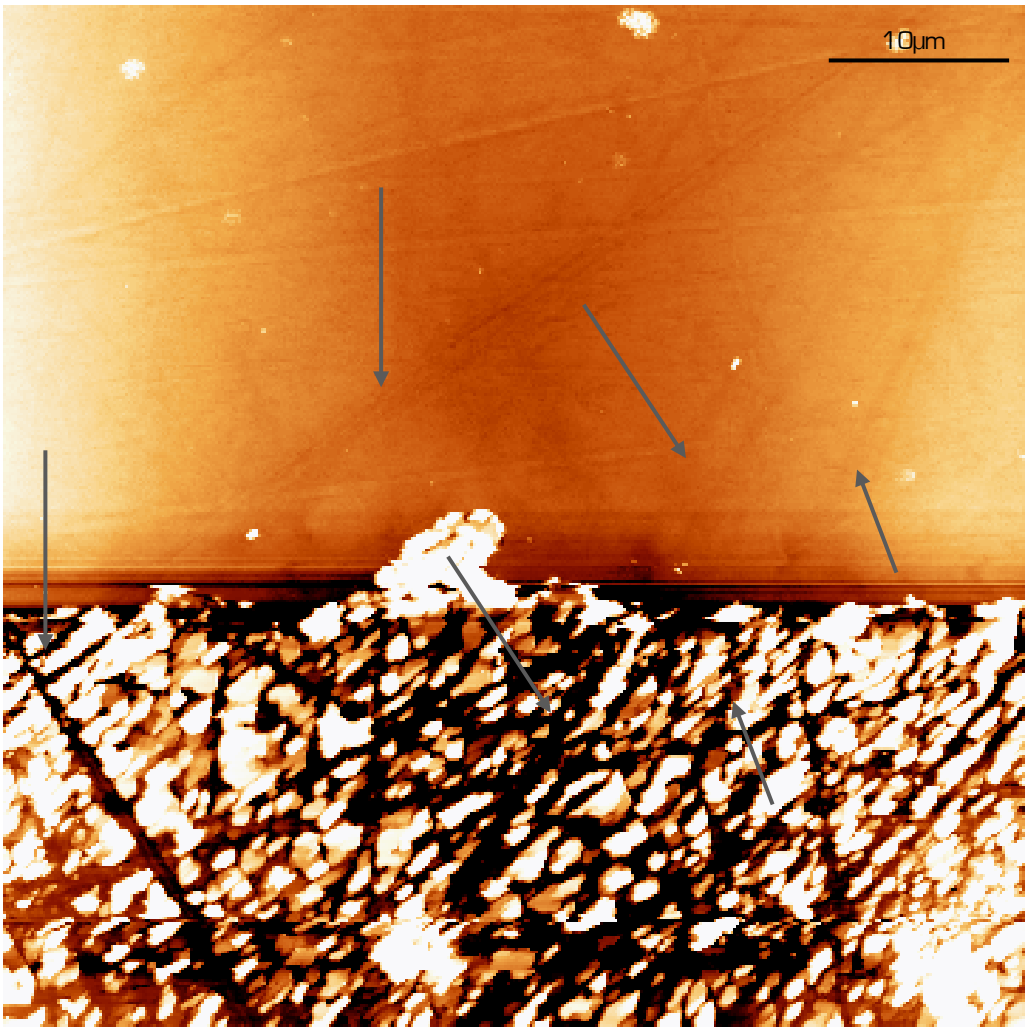


Figure 5.30: AFM image of $CuAl_2$ / sapphire long term sample; each parallel pair of arrows indicates a scratch which progresses from the unreacted substrate (top of image) into the interface area (bottom) where it becomes more pronounced

The AFM micrograph in Figure 5.31 of an Al-99.99 / alumina 15-minute sample shows that precipitates are formed already within this short time (though to lesser extent than during the long-term experiments). The etching effect is already noticeable in this sample too, showing distinct differences in degree of etching on grains of different orientation. This is evidence of varying surface free energy of different grains.

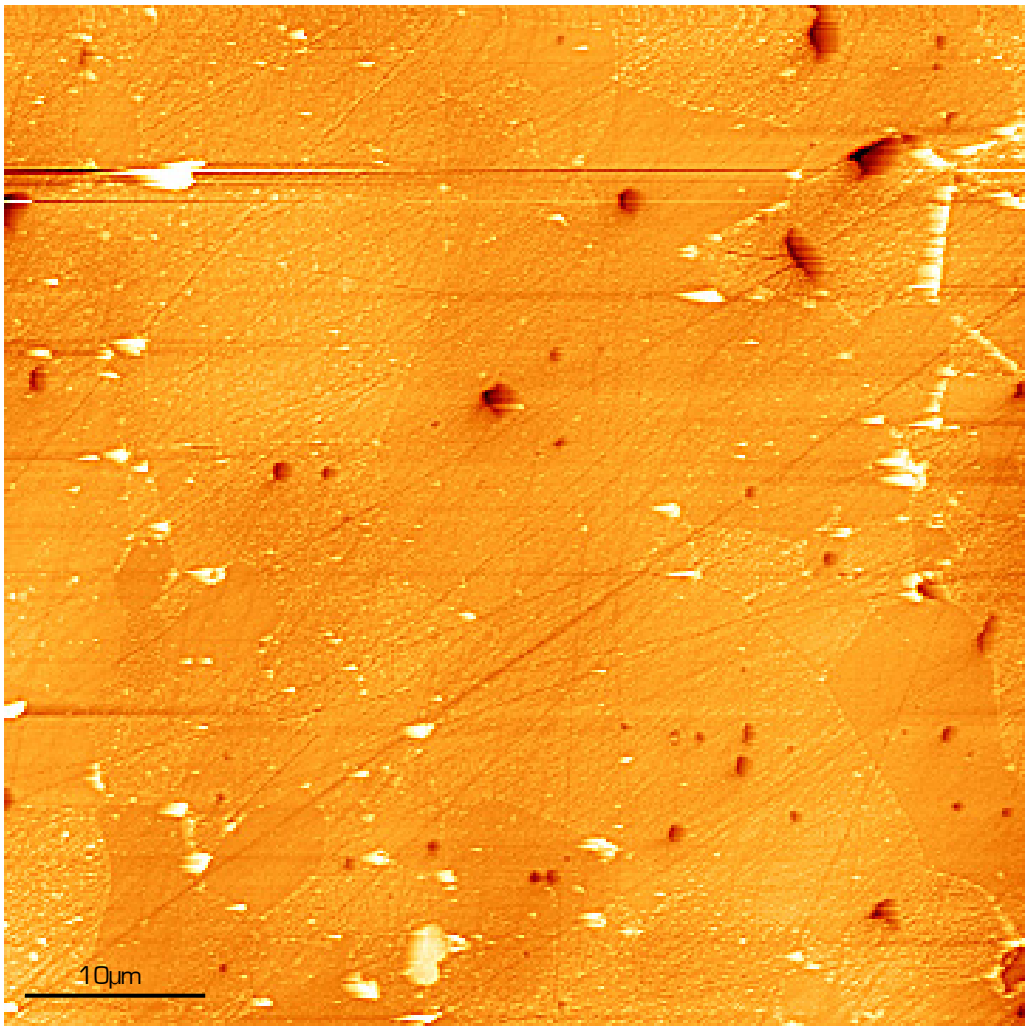


Figure 5.31: AFM micrograph of a 15-minute experiment of Al-99.99 / alumina. Different degrees of etching visible of different grains as well as islands of precipitates (white spots).

*5.3.2.3.2 Transmission Electron Microscopy*

Figure 5.32 shows a TEM micrograph of an Al-7Cu / sapphire long-term specimen in which two dark phases are visible on either side of the light aluminum matrix on top of the sapphire substrate. Using selective area electron diffraction (SAED) patterns it was possible to identify the $CuAl_2$ component of the eutectic phase in the alloy (ICDD pattern 25-0012), as well as a precipitate of $CuAl_2O_4$ (ICDD pattern 33-0448) at the interface grown on top of the sapphire (ICDD pattern 10-0173). This is of importance as it indicates that the substrate is not involved in the reaction between the liquid metal and the residual furnace oxygen and proves the thermodynamic calculations presented in section 5.3.2.2 to be correct.

The identification of $CuAl_2O_4$ at the interface is in contrast to the findings of *SCHEU* et

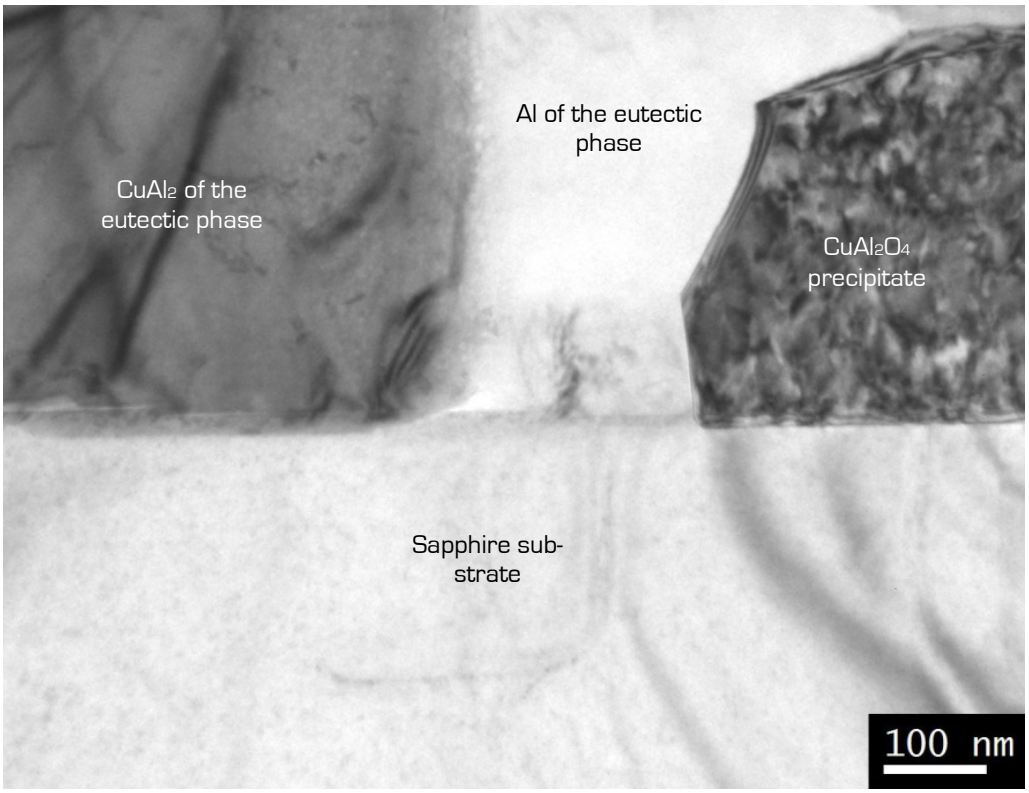


Figure 5.32: Overview TEM image of Al-7Cu / sapphire long-term sample

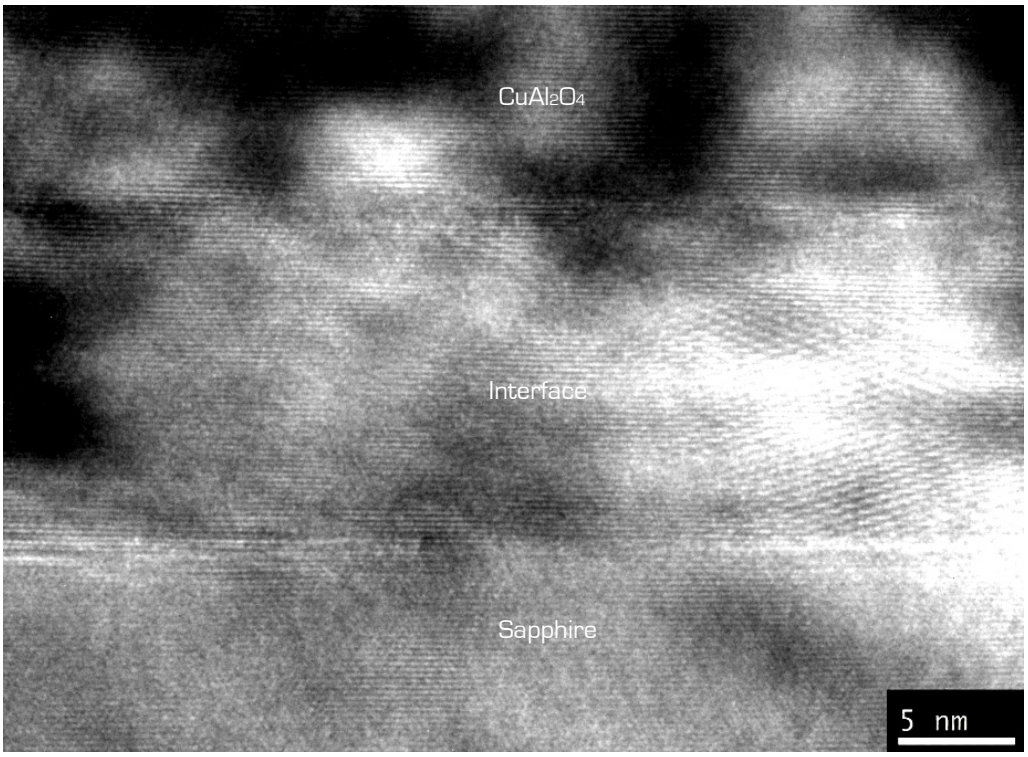


Figure 5.33: High-resolution TEM micrograph showing a crystallographic orientation relationship between the sapphire (bottom of image) and the $CuAl_2O_4$ phase (top of image)

al.[69], who identified $CuAlO_2$ at a copper / sapphire interface. It should be noted, however, that based on the thermodynamic calculations, it is very likely that $Cu_2Al_2O_4$ was formed as well but was not observed due to the size of TEM specimens. In both the metal and the alloy, striations of elastic strain are visible.

In the high-resolution image (Figure 5.33) crystallographic orientation alignment between the sapphire and the $CuAl_2O_4$ precipitate can be observed. In the micrograph, the interface is not parallel to the beam, which allows the intersection of the interface with the edges of the FIBed specimen to be seen, with the sapphire at the bottom and the $CuAl_2O_4$ precipitate at the top of the image.

A composite SAED pattern of this overlap area of the specimen (Figure 5.34) shows that the parallel planes are the $(11\bar{2}0)$ planes of the sapphire and the (111) planes

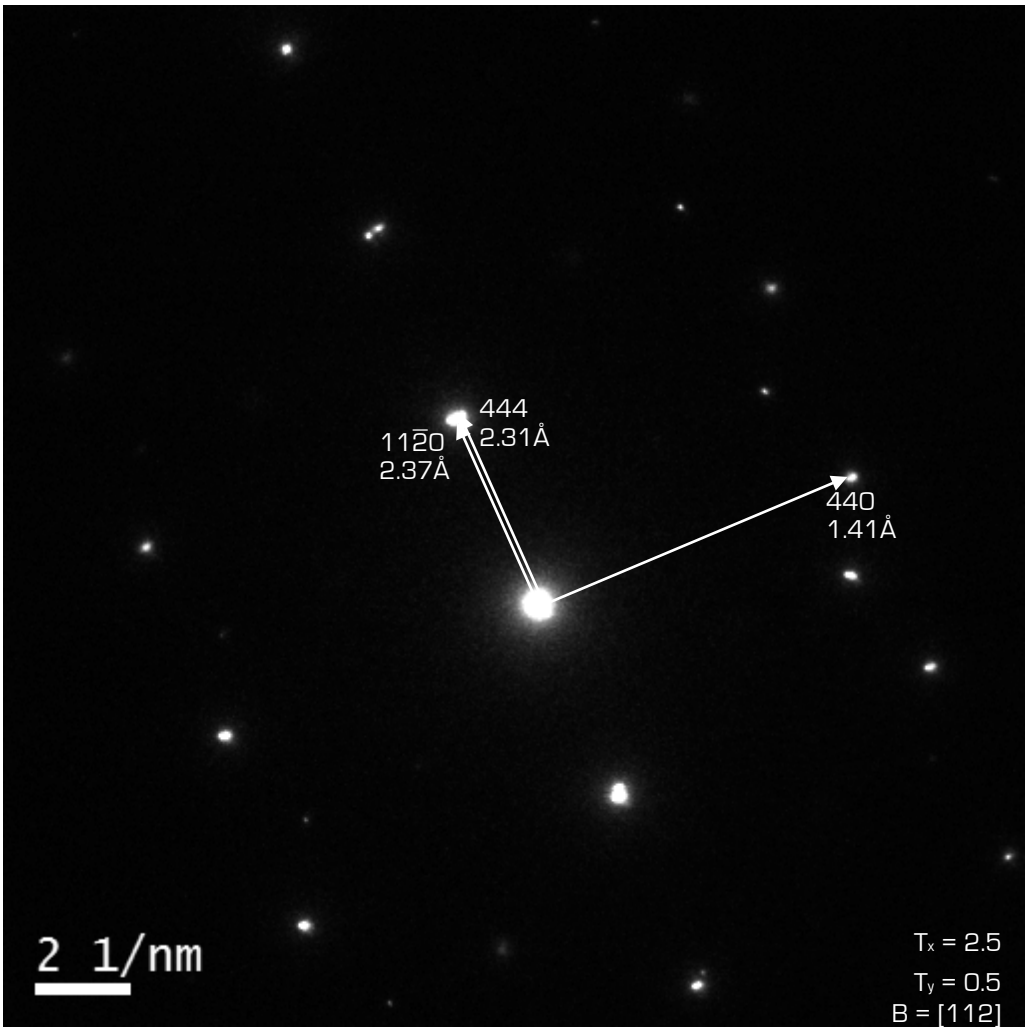


Figure 5.34: Composite SAED pattern of the overlap area in Figure 5.33 shows that the (11$\bar{2}$0) planes of the sapphire and the (111) planes of $CuAl_2O_4$ precipitate are parallel. The reflecting planes of the precipitate are the (444) and the (440) planes. This is equivalent to every fourth (111) and (110) planes. The measurements underneath the vector specifications are the respective planar distances *d*.

of the precipitate. The orientation alignment, together with the fact that $CuAl_2O_4$ is solid below 1200°C[107] and the observed increase in precipitation density with longer durations of the wetting experiments (as discussed previously) is evidence that the arrangement of the $CuAl_2O_4$ phase occurred while the long-term experiment (at 750°C) was running.

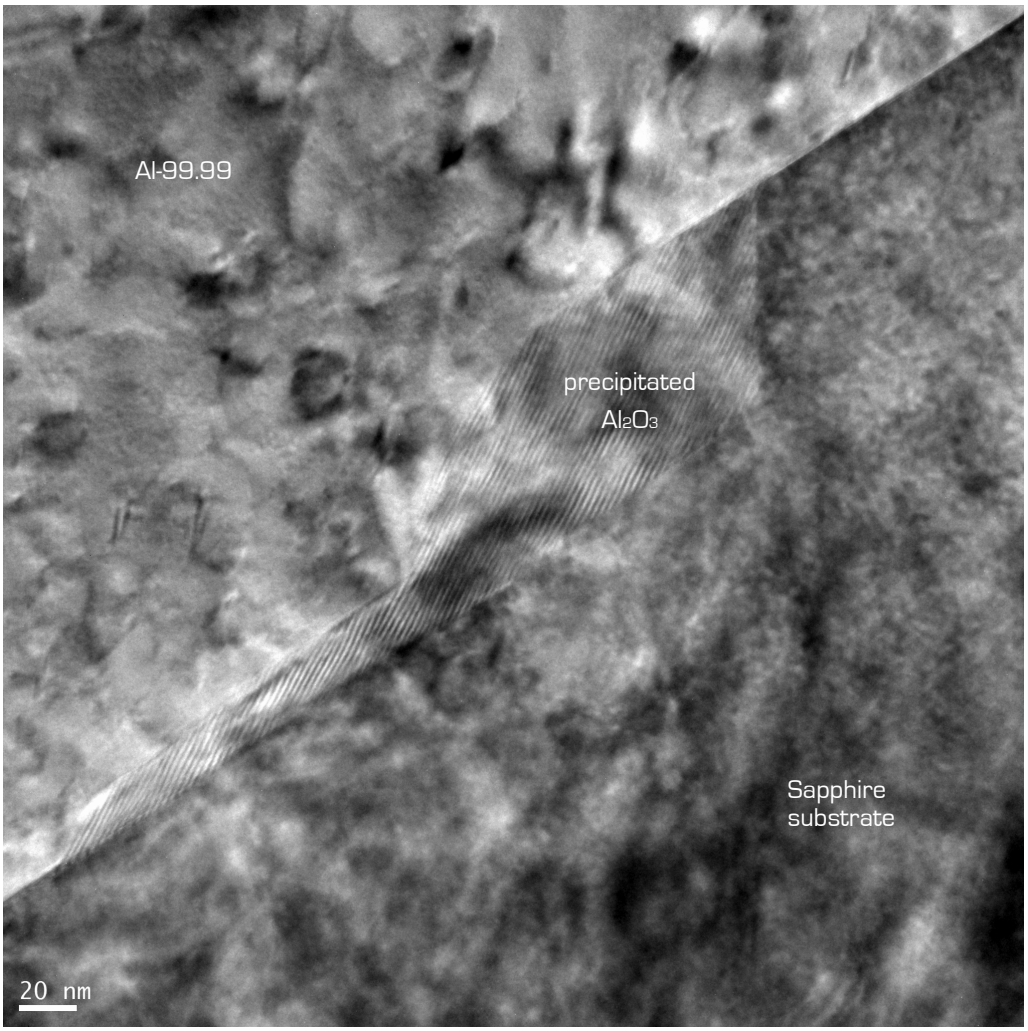


Figure 5.35: TEM image of Al-99.99 / sapphire sample; removal of sapphire substrate can be seen as well as precipitates of $Al_2O_3$

Furthermore, the existence of these $CuAl_2O_4$ precipitates at only the interface and almost certainly at the liquid-gas surface, but not inside the solidified bulk drop (as thorough FE-SEM work revealed), together with the thermodynamic finding that $Al_2O$ is not the oxidizing species, the asymptotical decrease in surface roughness from the triple line towards the center of the interface (Figure 5.29) is evidence that oxygen is transported along the interface to the center of the drop to react with the liquid alloy as suggested by *LEVI* and *KAPLAN*[65,68].



TEM observations on an Al-99.99 / sapphire long-term specimen (Figure 5.35) show evidence of removal of sapphire substrate. Together with the etching process that was observed on AFM micrographs of aluminum-copper alloys as well as pure aluminum on $Al_2O_3$ (Figures 5.30 and 5.31), it seems clear that aluminum in the liquid and $Al_2O_3$ beneath the sessile drops react to form $Al_2O$ at high temperatures and low pressures according to Equation 5.15. In addition, the precipitation of $Al_2O_3$ based on the reaction in Equation 5.8 in energetically favourable locations is evident.

$$4\,Al + Al_2O_3 \rightarrow 3\,Al_2O^{\uparrow} \qquad \text{Eq. 5.15}$$

$$2\,Al + {}^{3}/_{2}\,O_2 \rightarrow Al_2O_3 \qquad \text{Eq. 5.8}$$

Although $Al_2O$ is clearly generated, it is not the source for the spinel or $Al_2O_3$ formation, as has been shown by FactSage modeling (section 5.3.2.2) as well as by the interface roughness profiles (Figure 5.29). The whereabouts of this gaseous aluminum oxide remain therefore unclear, but it can reasonably be assumed that it is transported along the interface to the atmosphere surrounding the wetting experiment.

*5.3.2.3.3 X-Ray Photoelectron Spectroscopy*

Because the $CuAl_2$ alloy drops detached from the sapphire substrate during cooling after every experiment, TEM sample preparation of the interface region was not possible. Therefore, XPS analyses of the interface were performed for long-term samples of Al-7Cu on sapphire as well as of $CuAl_2$ on sapphire. Figures 5.36 show the XPS spectra of the substrate beneath an Al-7Cu drop. The copper photoelectron peak locations obtained from Figures 5.36 a) and b) are summarized in Table 5.5. Given that the TEM analyses identified the precipitates at the interface as $CuAl_2O_4$, the *CuLMM A* peak was chosen as the Auger electron peak location (among the 4 possible peaks in Figure 5.36 c)) since it yields Auger and the modified Auger parameters, $\alpha$ and $\alpha'$, that best verify the standard values for $CuAl_2O_4$ published in the NIST X-ray

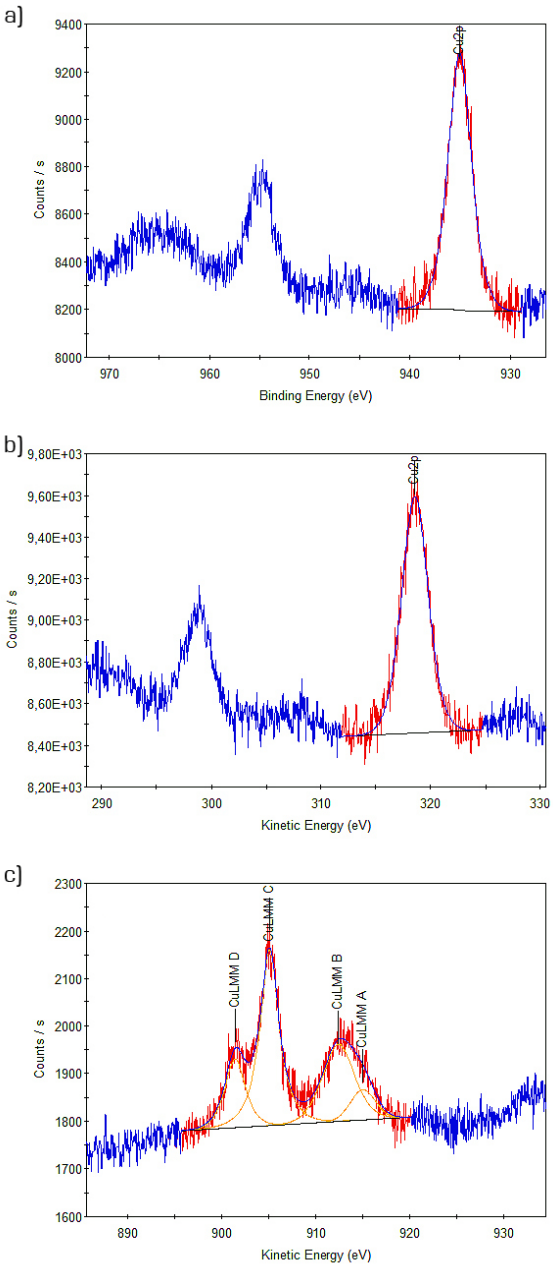


Figure 5.36: XPS spectra of Al-7Cu / sapphire a) zoomed in on the Cu2p$_{3/2}$ peak in the bonding energy spectrum, b) zoomed in on the same Cu2p$_{3/2}$ in the kinetic energy spectrum, and c) zoomed in on the *CuL$_3$M$_{45}$M$_{45}$* peak set.

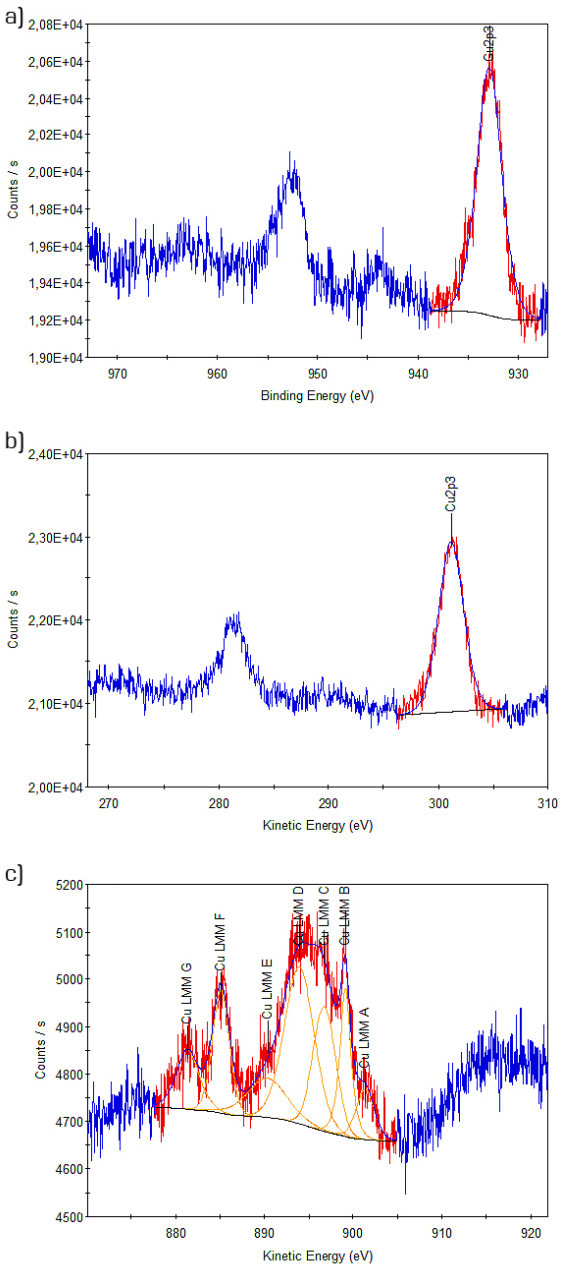


Figure 5.37: XPS spectra of $CuAl_2$ / sapphire a) zoomed in on the Cu2p$_{3/2}$ peak in the bonding energy spectrum, b) zoomed in on the same Cu2p$_{3/2}$ in the kinetic energy spectrum, and c) zoomed in on the *CuL$_3$M$_{45}$M$_{45}$* peak set.



Table 5.5: Photoelectron and Auger electron energies obtained from XPS

| Specimen | Bonding Energy $BE_P$ of the $Cu2p_{3/2}$ peak [eV] | Kinetic Energy $KE_P$ of the $Cu2p_{3/2}$ peak [eV] | Auger Kinetic Energy $KE_A$ of the $CuL_3M_{45}M_{45}$ peak [eV] | Auger Parameter $\alpha = KE_A - KE_P$ | Modified Auger Parameter $\alpha' = KE_A + BE_P$ |
|---|---|---|---|---|---|
| Al-7Cu on sapphire | 935.0 | 318.6 | 915.1 | 596.5 | 1850.1 |
| $CuAl_2$ on sapphire | 933.9 | 301.2 | 898.4 | 597.2 | 1832.3 |
| $CuAl_2O_4$ (NIST standard [108]) | 934.7 | 318.9 | 916.8 | 597.9 | 1851.5 |

photoelectron spectroscopy database.[108] Although, in general, the strongest of the *LMM* peaks should be used for the Auger and modified Auger parameter calculation, the explained procedure is valid since the existence of $CuAl_2O_4$ at the Al-7Cu / sapphire interface has been confirmed using TEM and SAED patterns.

Figures 5.37 a) and b) show the copper photoelectron peaks of the $CuAl_2$ / sapphire interface; the peak locations are presented in Table 5.5. In order to verify the presence of $CuAl_2O_4$ at the $CuAl_2$ / sapphire interface, the *CuLMM B* peak as the strongest of the *LMM* peak set in Figure 5.37 c) was chosen for the calculation of $\alpha$ and $\alpha'$ as shown in Table 5.5. From this table, it can be seen that the values are reasonably close to those published in the NIST database. Therefore, characterization results by XPS confirm that $CuAl_2O_4$ is present not only at the Al-7Cu / sapphire but also at the $CuAl_2$ / sapphire interface, and thus most likely in all other aluminum-copper alloy compositions investigated.

### 5.3.3 Microscopy & Microanalysis work – Wetting of Alumina & Sapphire

EPMA analyses on sections through solidified Al-1Mg drops on both substrates show magnesium depletion. This is an indication that magnesium at least partially evaporates from the alloy under the experimental conditions. The different wetting behaviour of Al-1Mg and pure aluminum on both substrates particularly at low tempera-

tures (Figures 5.17 and 5.18), however, suggests that enough magnesium is left in the alloy when it is dispensed onto the substrate to alter wetting of the system noticeably.

Using FactSage in a very similar fashion as in section 5.3.2.2, the activities of aluminum and magnesium of a liquid Al-1Mg at 700°C can be modeled. Using the program's *EQUILIB* function, one obtains

$$a(\mathrm{Al_{liq}}) = 0.88679 \qquad \text{Eq. 5.17}$$

$$a\left(\mathrm{Mg_{liq}}\right) = 0.063147 \qquad \text{Eq. 5.18}$$

FactSage's *REACTION* function models the reaction

$$2\,\mathrm{Al} + \mathrm{Mg} + 2\,\mathrm{O_2} \rightarrow \mathrm{MgAl_2O_4} \qquad \text{Eq. 5.19}$$

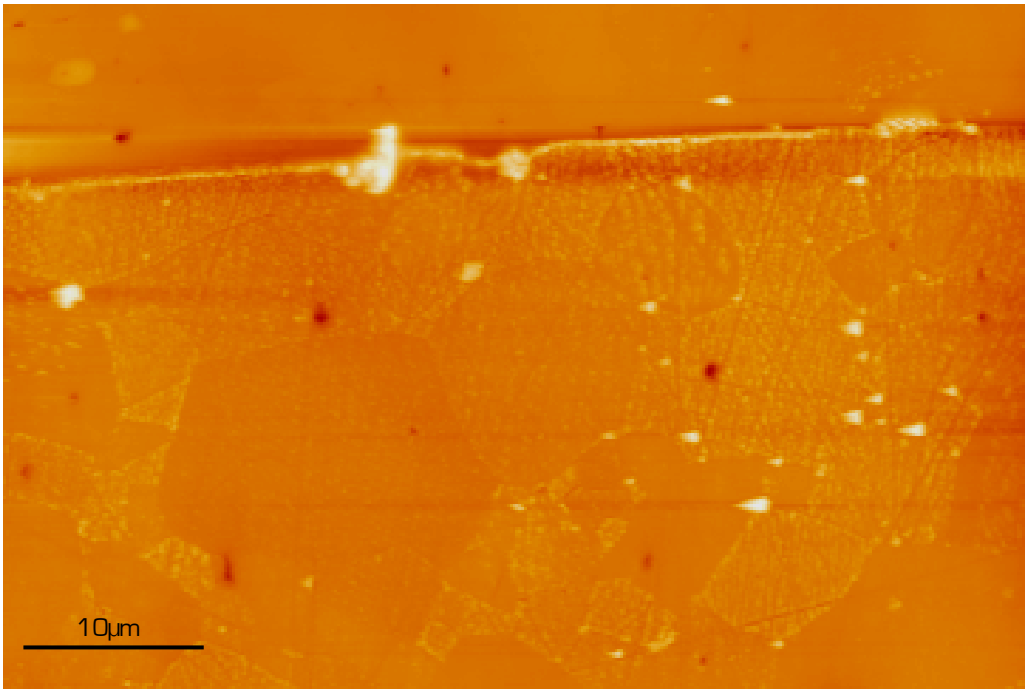


Figure 5.38: AFM micrograph of a 15-minute experiment of Al-1Mg / alumina. Different degrees of etching visible of different grains as well as islands of precipitates (white spots), and line of precipitation at the triple line.



to have a $\Delta G^0 = -2219\text{kJ}$. Following the same procedure as described above, one obtains a minimum required oxygen partial pressure of $p(O_2) \approx 5 \cdot 10^{-56}\text{mbar}$ for the reaction to take place. Evidence of this reaction occurring can be seen in the white spots and the white line of precipitation product along the triple line in the AFM micrograph of a 15-minute wetting experiment with Al-1Mg on alumina (Figure 5.38). The formation of $MgAl_2O_4$ at the interface can be seen as the reason for the differing wetting behaviour of Al-1Mg and pure aluminum on $Al_2O_3$. It also contributes to the depletion in magnesium in the solidified alloy drop. In particular, the formation of reaction product at the triple line after only 15 minutes suggests a very rapid reaction. The ridge formation at the triple line can be seen as an indication that Al-1Mg / $Al_2O_3$ wetting systems do not reach equilibrium, as the triple line is likely to be pinned by the ridge.

The reason for the significant decline in wettability of alumina and sapphire by pure aluminum, aluminum-copper alloys, A356, and AA6061 (but not Al-1Mg and Al-11.5Si) with decreasing temperature has yet to be determined. In similar cases, it has been argued in literature[53] that clusters or embryos of atoms in the liquid form at the interface, particularly just above the liquidus temperature of the alloy (induced by the atomic structure of the substrate) and alter the wetting behaviour of the system. Following this line of argument, one could reason that such clusters or embryos form in the case of (almost) constant wetting behaviour over the investigated temperature range and do not in cases exhibiting significantly increasing contact angles upon cooling, or vice versa. This difference could then be carried forward as the reason for the different behaviour at low temperatures.

It must be assumed, however, that such clusters would be noticeably more prone to be oxidized and form precipitates such as $CuAl_2O_4$, or $MgAl_2O_4$ at the interface if the interface has enough oxygen transport capacity and if the oxygen partial pressure in the reactor favours this. However, as has been shown, the formation of $CuAl_2O_4$ along

the interface is the reason for improved wetting of $Al_2O_3$ by aluminum-copper alloys and contradicts the increase in contact angle just above the liquidus temperature. Similarly, $MgAl_2O_4$ formation in the Al-1Mg / $Al_2O_3$ system has been named the reason for this system having higher contact angles than Al-99.99 / $Al_2O_3$ at elevated temperatures and cannot cause better wetting just above the liquidus temperature.

It is furthermore interesting to see that while magnesium and silicon additions to aluminum very significantly alter the wetting behaviour of the liquid binary alloys on $Al_2O_3$ just above the respective liquidus temperatures, A356 and AA6061, which are aluminum alloys containing magnesium *and* silicon, do not exhibit such modification in low temperature contact angles on $Al_2O_3$. Again, one might claim that while magnesium *or* silicon atoms in the liquid binary alloy alter the solid-liquid interface energy, $\sigma_{SL}$, magnesium *and* silicon in A356 / $Al_2O_3$ or AA6061 / $Al_2O_3$ wetting systems form embryos of $Mg_2Si$ for example and thereby make magnesium and silicon less available to modify the solid-liquid surface energy.

It should be noted that the formation of clusters of atoms in a liquid metal has not yet been shown experimentally. Current microscopy techniques do not allow the interface of a wetting experiment to be analysed as it is being conducted. Arguments based on such clusters are consequently pure speculation. It furthermore appears more likely that the significantly higher contact angles at lower temperatures are caused by a strong increase in liquid-vapour surface energy, $\sigma_{LV}$, just above the liquidus or melting temperature. This is less pronounced in the case of Al-1Mg / $Al_2O_3$ and Al-11.5Si / $Al_2O_3$, as the surface energies of liquid magnesium and liquid silicon are lower than that of liquid aluminum.[105]

### 5.3.4 Wetting of Silicon Carbide

The contact angle measurements in the case of α-SiC substrates were generally noticeably less repeatable than in wetting experiments on alumina or sapphire.

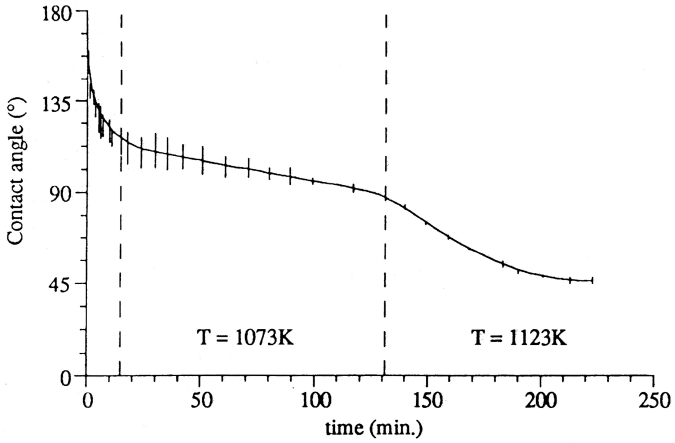


Figure 5.39: Wetting of pure aluminum on SiC as reported by *LAURENT* et al.[75] at 800°C (1073K) before the temperature is raised to 850°C (1123K). Continuous decrease in contact angle over approximately 2 hours can be observed with an equilibrium contact angle at 850°C of roughly 45°

Therefore, an experimental error of ±5° must be considered in these cases. Contact angle measurements within a particular experiment, however, were trivial.

The commonly reported contact angle change for pure aluminum on silicon carbide over several hours, as reported by *LAURENT* et al.[74,75] is presented in Figure 5.39.

Such behaviour has not been observed in the current experiments (Figures 5.40 to 5.45). Most investigated wetting systems involving silicon carbide showed changing contact angles at some temperatures; however, changes never occurred beyond 15 to 20 minutes as long-term trials with all investigated alloys showed. Only in the cases of Al-11.5Si and Al-7Cu on SiC was it therefore worthwhile to conduct wetting experiments over 3 hours.

Similar to the wetting experiments on alumina and sapphire, contact angles of Al-99.99, Al-1Mg, A356, and AA6061 on SiC (Figures 5.40, and 5.43 to 5.45) reach a constant value within 2 to 3 minutes. In these cases, it appears likely that the explanation regarding drop ejection force (following *SHEN* et al.[98]) is valid again.

The contact angle changes over 15 to 20 minutes in several tests in the case of Al-11.5Si and Al-7Cu on SiC (Figures 5.41 and 5.42), however, are more likely to be caused by chemical reactions such as the dissolution of silicon in the alloy and the precipitation of $Al_4C_3$ as reported in literature[53,74,75].

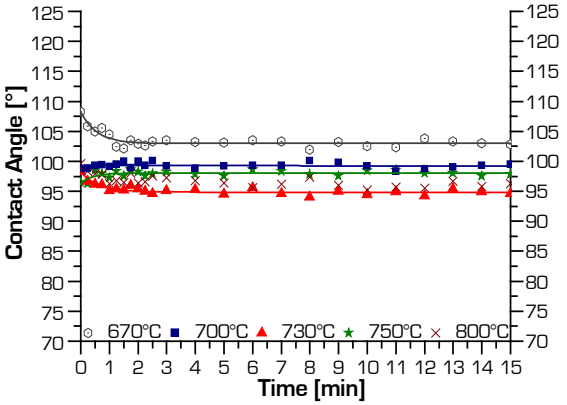


Figure 5.40: Contact angles vs. time for Al-99.99 on SiC

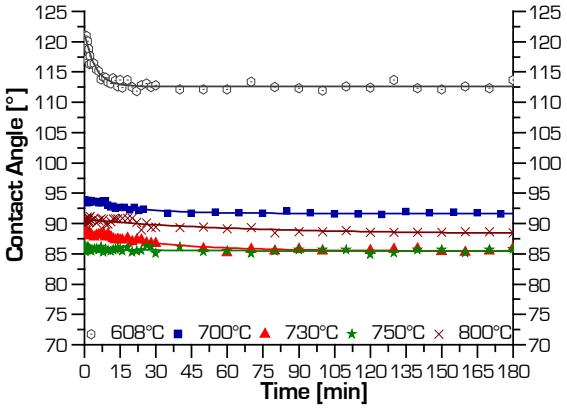


Figure 5.41: Contact angles vs. time for Al-11.5Si on SiC

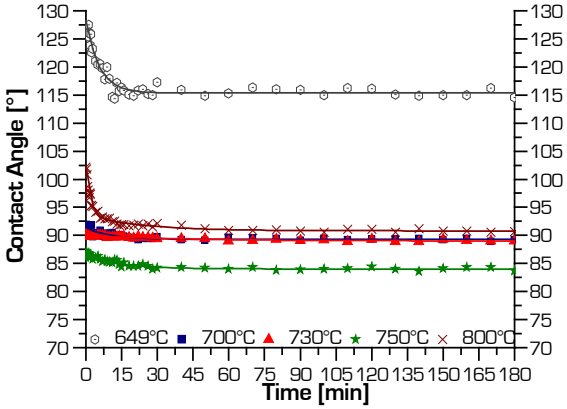


Figure 5.42: Contact angles vs. time for Al-7Cu on SiC

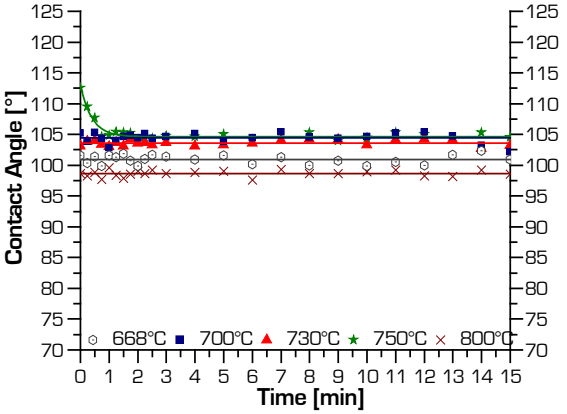


Figure 5.43: Contact angles vs. time for Al-1Mg on SiC

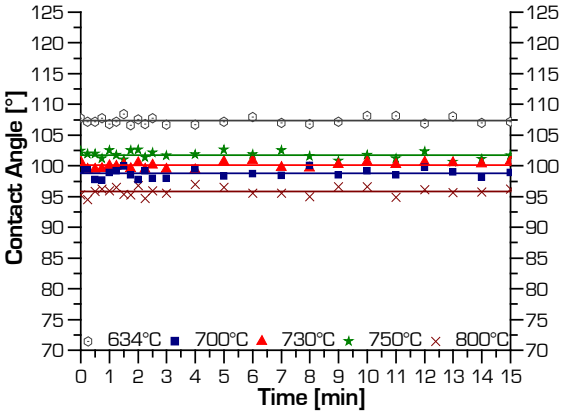


Figure 5.44: Contact angles vs. time for Al356 on SiC

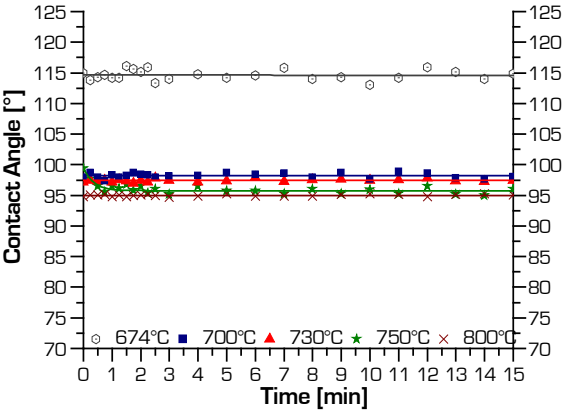


Figure 5.45: Contact angles vs. time for AA6061 on SiC

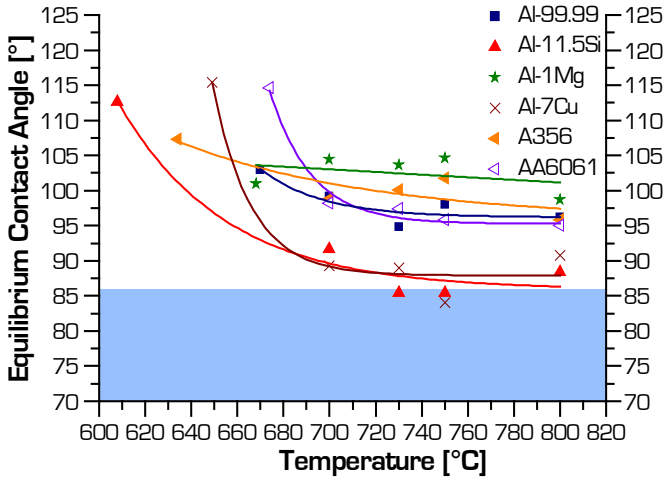


Figure 5.46: Wetting behaviour of Al-99.99, Al-11.5Si, Al-1Mg, Al-7Cu, A356, and AA6061 on SiC

As can be seen from Figure 5.46, the equilibrium contact angles[h] of all alloys except Al-1Mg show a noticeable increase towards the liquidus temperature of the alloy or the melting point of the metal. No alloy / SiC wetting system appears to reach the optimum contact angle range after *KAPTAY*[12].

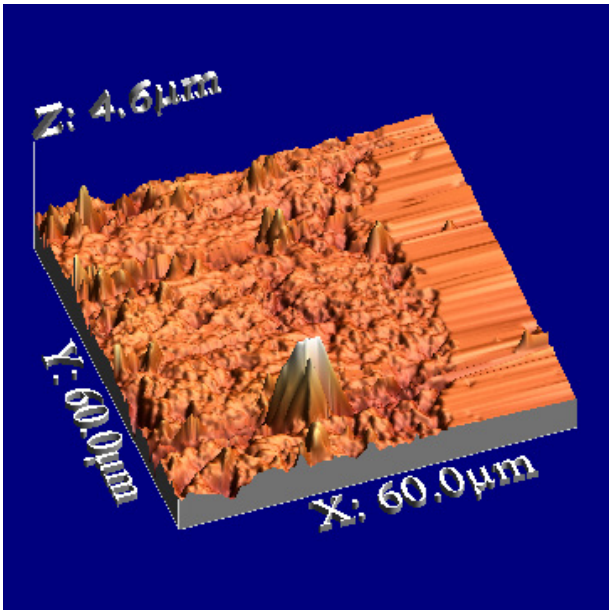


Figure 5.47: AFM micrograph of an Al-99.99 / SiC wetting experiment (15 minutes) after the drop has been removed.

The observed wetting behaviour on silicon carbide, showing contact angle changes at best for the first 15 to 20 minutes of certain wetting experiments, is in stark contrast to literature. *LAURENT* et al.[74,75] and others[53,109,110] agree upon the reactive character of the wetting system liquid aluminum on silicon carbide.

Figure 5.47 shows an AFM micrograph of a 15-minute Al-99.99 / SiC wetting experiment at 750°C after the solidified drop was removed chemically. It shows clearly that a step of a few

[h] Note that the equilibrium contact angles for Al-11.5Si / SiC and Al-7Cu / SiC have been taken after 3 hours, while those of the other investigated wetting systems involving SiC were taken after 15 minutes.

hundred nanometres in height has formed where the triple line of the wetting experiment was. The formation of a such pronounced step during 15 minutes of wetting contact demonstrates the dramatically reactive nature of the wetting system. The micrograph also shows very pronounced islands in the very rough interface. These precipitates are likely $Al_3C_4$, as has been described by *LAURENT* et al.[74,75]

Similar observations were made on samples of other alloy / SiC wetting experiments. Therefore, it is clear that these wetting systems are of the reactive type. That they, despite reactive wetting, do not show changing contact angles over several hours and do not equilibrate inside the wetting regime means that the triple line is pinned by the rapidly developing step.

The reason for this is likely that the SiC substrates used in the present experiments presumably have little native $SiO_2$ *protecting* the surface, as they were transferred from the vibro-polisher immediately into the vacuum furnace for the wetting tests. More importantly, the metal or alloy drop, freed of the oxide layer, can react with the substrate immediately upon impingement on the ceramic. In contrast in the standard sessile drop experiments reported in literature[74,75], *protective* layers of $SiO_2$ on the silicon carbide and $Al_2O_3$ on the aluminum drop cause the dissolution-precipitation reactions to commence gradually as the liquid metal is provided to the interface slowly and steadily over several tens of minutes. As the reaction in these cases occurs in a more measured fashion, the formation of a pinning ridge at the triple line does not occur until equilibrium is reached.

Such protective layers are not present in the current case. It can therefore be assumed that the reaction between aluminum (alloys) and the silicon carbide substrate in the present case is so rapid that equilibrium is never reached since the drop digs itself into the substrate rather than spreading on it. The contact angles presented in Figures 5.40 to 5.46 must consequently be seen in the light of this important limitation.

## 5.4 FOAMING

The discussion of the foaming results will be divided into two sections: foams stabilized by alumina particles and those stabilized by silicon carbide.

### 5.4.1 Alumina Stabilized Foams

Expansion curves were recorded over 20 minutes at 90°C and 140°C above the liquidus temperature or melting point as presented in section 5.2 (Figures 5.48 to 5.59). From several of these expansion curves, such as in Figure 5.48 or Figure 5.51, it can be seen that the expansion onset varies by a few tens of seconds. The reason for this is that the placement of the compact into the crucible took slightly longer in those cases with later onset of expansion. As the heat shield is removed from the furnace during sample placement, the furnace lost temperature during these delays and the hydrogen release onset is consequently delayed.

All compositions at both respective foaming temperatures show five main stages in the expansion curve:

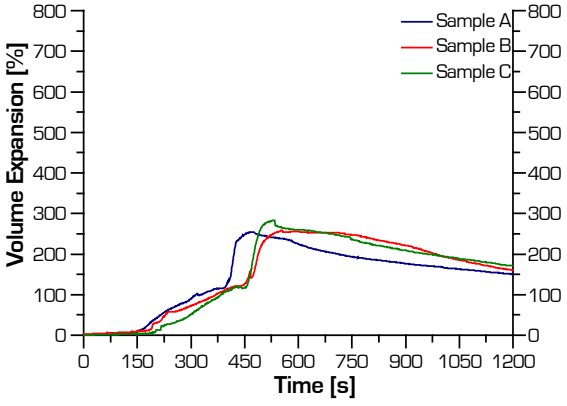


Figure 5.48: Foam expansion curves for Al-99.99 with 1wt.% $TiH_2$ and 8vol.% $Al_2O_3$ at 750°C

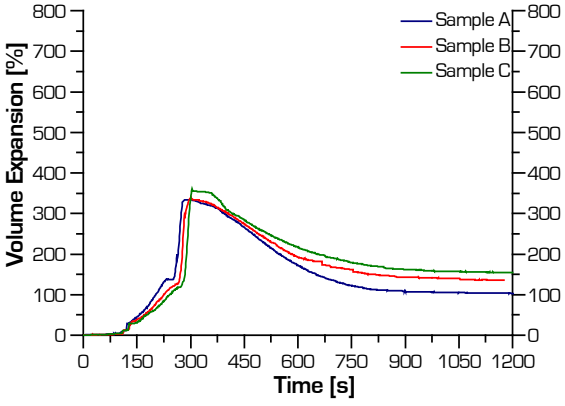


Figure 5.49: Foam expansion curves for Al-99.99 with 1wt.% $TiH_2$ and 8vol.% $Al_2O_3$ at 800°C

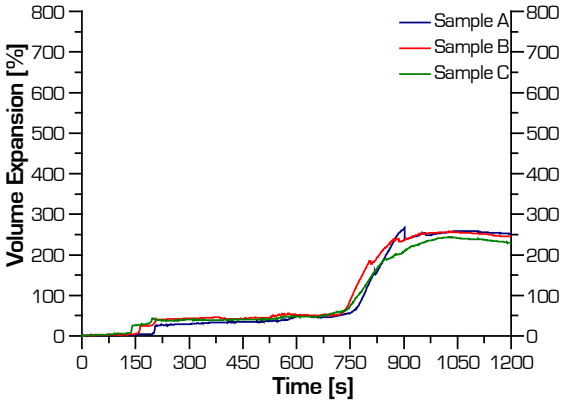


Figure 5.50: Foam expansion curves for Al-11.5Si with 1wt.% $TiH_2$ and 8vol.% $Al_2O_3$ at 688°C

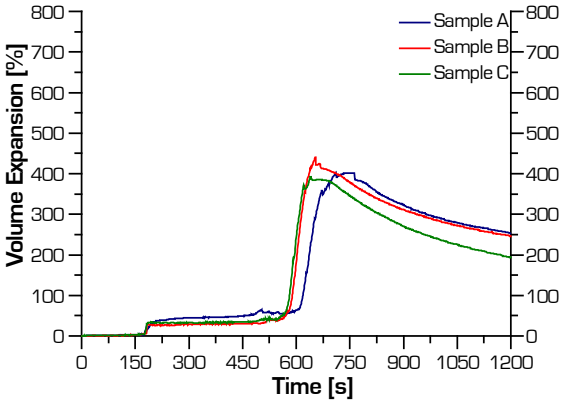


Figure 5.51: Foam expansion curves for Al-11.5Si with 1wt.% $TiH_2$ and 8vol.% $Al_2O_3$ at 738°C

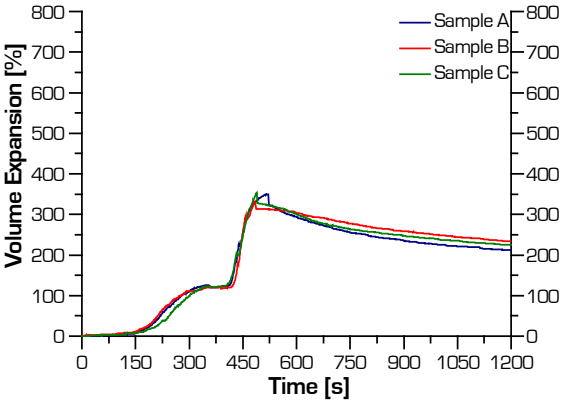


Figure 5.52: Foam expansion curves for Al-7Cu with 1wt.% $TiH_2$ and 8vol.% $Al_2O_3$ at 729°C

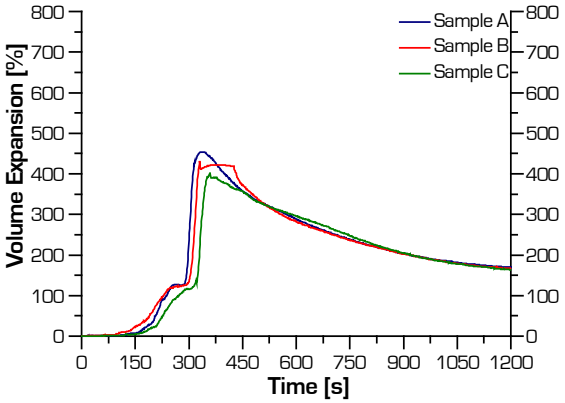


Figure 5.53: Foam expansion curves for Al-7Cu with 1wt.% $TiH_2$ and 8vol.% $Al_2O_3$ at 779°C

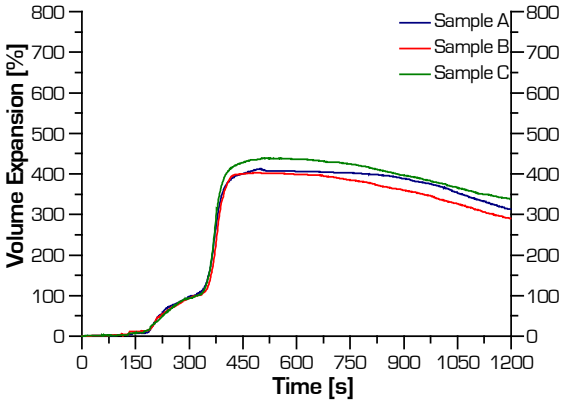


Figure 5.54: Foam expansion curves for Al-1Mg with 1wt.% $TiH_2$ and 8vol.% $Al_2O_3$ at 748°C

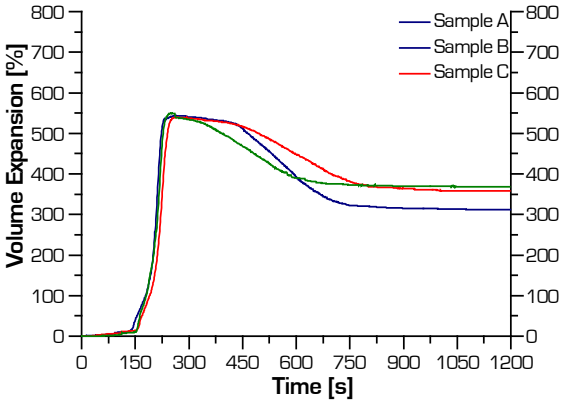


Figure 5.55: Foam expansion curves for Al-1Mg with 1wt.% $TiH_2$ and 8vol.% $Al_2O_3$ at 798°C

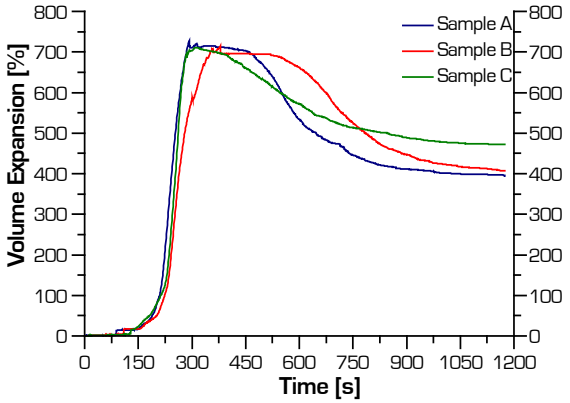


Figure 5.56: Foam expansion curves for A356 with 1wt.% $TiH_2$ and 8vol.% $Al_2O_3$ at 714°C

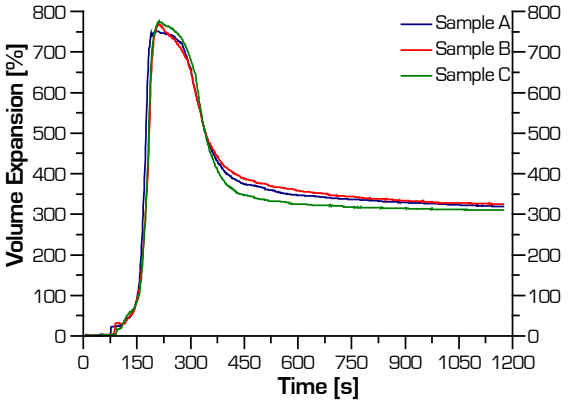


Figure 5.57: Foam expansion curves for A356 with 1wt.% $TiH_2$ and 8vol.% $Al_2O_3$ at 764°C

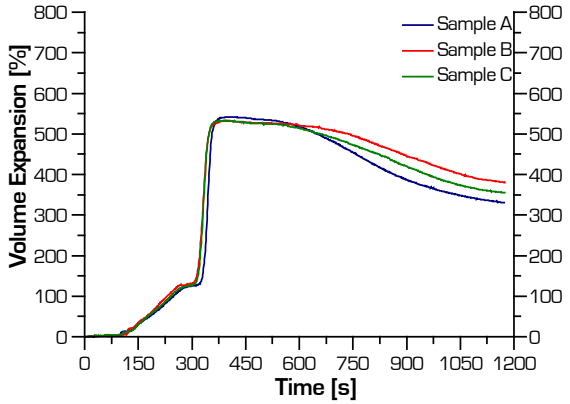


Figure 5.58: Foam expansion curves for AA6061 with 1wt.% $TiH_2$ and 8vol.% $Al_2O_3$ at 754°C

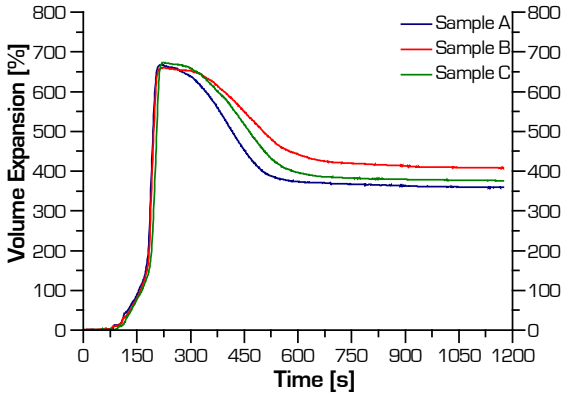


Figure 5.59: Foam expansion curves for AA6061 with 1wt.% $TiH_2$ and 8vol.% $Al_2O_3$ at 804°C

During the first 70s to 150s, depending on composition and foaming temperature, no significant expansion is observed. In this stage, the sample heats up and sample growth is to a large extent due to thermal expansion.

At the beginning of the second stage, the metal is almost molten and the blowing agent begins to decompose. This is usually characterized by cracks forming in the compacts, and by the top and bottom of the samples becoming slightly dome-shaped. During this stage, hydrogen escapes to the periphery, since foaming agent decomposition occurs at a lower temperature than metal melting. Once the sample is molten,

it expands in all directions until the crucible walls are reached and the dome-shape at the top and the bottom disappears due to the load exerted by the plunger.

In stage 3, the foam fills the complete diameter of the crucible, expansion is restricted to unidirectional growth, and the evolving gas is used more efficiently for volume growth. As the volume increase to fill the crucible diameter during stage 2 is not considered in the volume growth calculation, the expansion rate is always slower than in stage 3. In the cases of the Al-7Cu / $Al_2O_3$ and Al-11.5Si / $Al_2O_3$ compositions (Figures 5.50 to 5.53) a distinct plateau can even be observed between the two stages. It is believed that in these cases the domes disappear at the same rate as the overall foam expands until it reaches the crucible walls.

Since the heating input into the sample is higher for the higher of the two respective foaming temperatures, the time delay between hydrogen release onset by the foaming agent (at roughly 500°C)[26] and the melting of the alloy is shortened at this temperature (i.e. the stages 2 and particularly 3 start earlier). This results in less foaming gas being lost through cracks in the compact while it is still solid. Hence, the larger maximum foam expansions are observed for the higher respective foaming temperatures.

Stage 4 commences when the rate of expansion and that of foam collapse become even. Most experiments show a plateau at maximum expansion for at least a few tens of seconds. In the case of Al-1Mg / $Al_2O_3$ at 748°C (Figure 5.54), this plateau lasts for approximately 7 minutes.

The last stage is dominated by very noticeable foam collapse and volume decrease after maximum expansion has been reached. In several cases, foam collapse levels out towards the end of the 20-minutes test and overall expansion becomes constant. For Al-99.99 / $Al_2O_3$ and Al-7Cu / $Al_2O_3$ at both respective temperatures (Figures 5.48 and 5.49, as well as 5.52 and 5.53), as well as for Al-1Mg / $Al_2O_3$ and Al-11.5Si /



$Al_2O_3$ at the higher respective foaming temperature (Figures 5.51 and 5.55), this foam collapse is very pronounced; the rate and extent of it is generally more dramatic at the higher temperatures.

Al-11.5Si / $Al_2O_3$ at 688°C does not seem to show significant foam collapse during the 20 minutes over which the expansion curves were recorded. Additional, longer foaming time tests with Al-11.5Si / $Al_2O_3$, however, demonstrate that foam collapse commences after approximately 23 minutes (1360s).

The photographs in Figures 5.60 to 5.83 show longitudinal foam sections. From these, it can be seen that foams generated to reach maximum expansion generally exhibit more rounded pores and mostly a sharper pore size distribution than over-aged foams. Al-11.5Si / $Al_2O_3$ at 688°C is an exception in terms of the pore size distribution, as this condition shows a wide range of pore sizes, which appear rather irregular already at maximum expansion.

The foams interrupted 5 minutes after maximum foam expansion all show significant pore coarsening, irregular pore shapes, significant drainage of metal to the bottom of the foam, collapsed cell walls, as well as extreme thinning of the latter in the upper half of the foam. In the cases of the Al-7Cu / $Al_2O_3$ and AA6061 / $Al_2O_3$ foams, some rounded pores usually remain in the bottom third of the foam, surrounded by the drained metal. At the higher of the respective foaming temperatures caving-in of the foam walls is often apparent in the overaged foams.

Al-1Mg / $Al_2O_3$ foams, particularly at the 798°C foaming temperature, tend to form elongated vertical pores in the center of the foam, which remain somewhat stable even 5 minutes after maximum expansion.

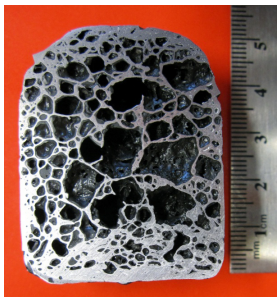

Figure 5.60: Al-99.99 / $Al_2O_3$ foamed to maximum expansion at 750°C

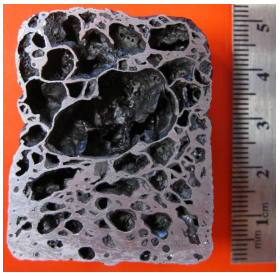

Figure 5.61: Al-99.99 / $Al_2O_3$ foam overaged at 750°C

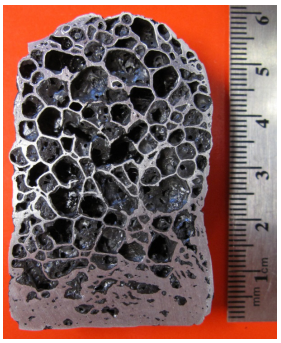

Figure 5.62: Al-99.99 / $Al_2O_3$ foamed to maximum expansion at 800°C

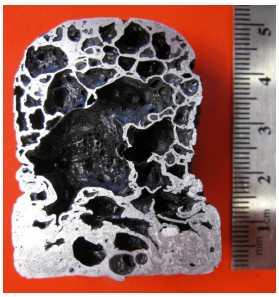

Figure 5.63: Al-99.99 / $Al_2O_3$ foam overaged at 800°C

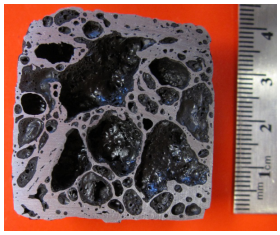

Figure 5.64: Al-11.5Si / $Al_2O_3$ foamed to maximum expansion at 688°C

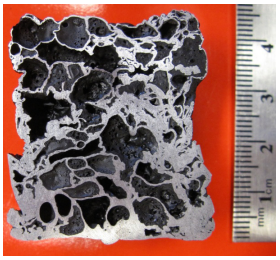

Figure 5.65: Al-11.5Si / $Al_2O_3$ foam overaged at 688°C

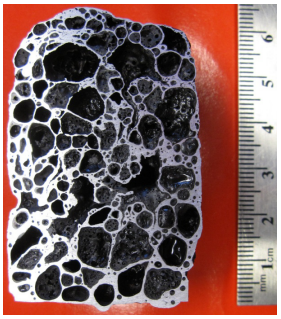

Figure 5.66: Al-11.5Si / $Al_2O_3$ foamed to maximum expansion at 738°C

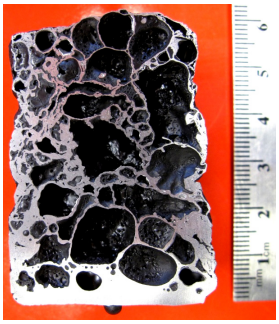

Figure 5.67: Al-11.5Si / $Al_2O_3$ foam overaged at 738°C

Figure 5.68: Al-7Cu / $Al_2O_3$ foamed to maximum expansion at 729°C

Figure 5.69: Al-7Cu / $Al_2O_3$ foam overaged at 729°C

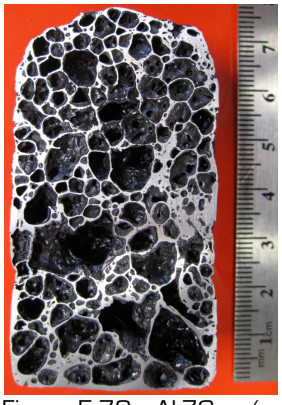

Figure 5.70: Al-7Cu / $Al_2O_3$ foamed to maximum expansion at 779°C

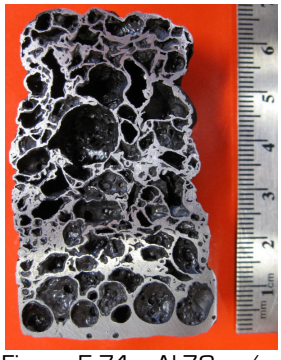

Figure 5.71: Al-7Cu / $Al_2O_3$ foam overaged at 779°C

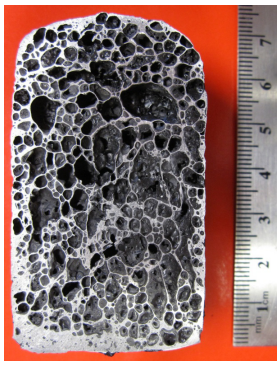

Figure 5.72: Al-1Mg / $Al_2O_3$ foamed to maximum expansion at 748°C

Figure 5.73: Al-1Mg / $Al_2O_3$ foam overaged at 748°C

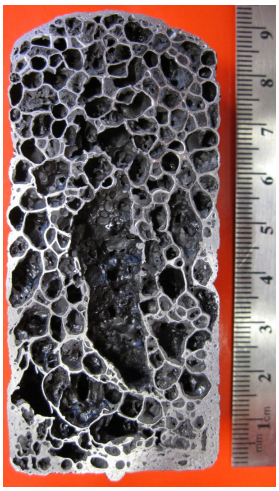

Figure 5.74: Al-1Mg / $Al_2O_3$ foamed to maximum expansion at 798°C

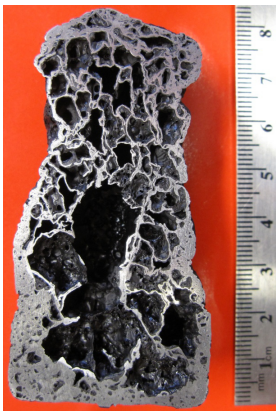

Figure 5.75: Al-1Mg / $Al_2O_3$ foam overaged at 798°C

Figure 5.76: A356 / $Al_2O_3$ foamed to maximum expansion at 714°C

Figure 5.77: A356 / $Al_2O_3$ foam overaged at 714°C

Figure 5.78: A356 / $Al_2O_3$ foamed to maximum expansion at 764°C

Figure 5.79: A356 / $Al_2O_3$ foam overaged at 764°C

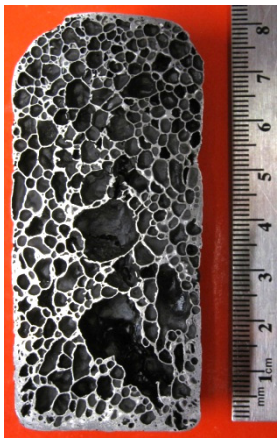

Figure 5.80: AA6061 / $Al_2O_3$ foamed to maximum expansion at 754°C

Figure 5.81: AA6061 / $Al_2O_3$ foam overaged at 754°C

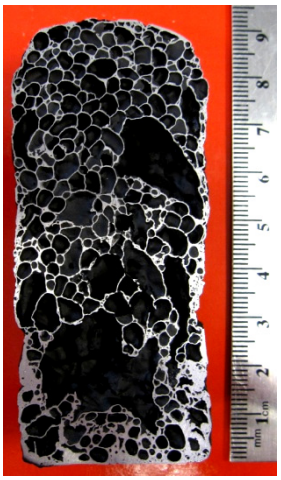

Figure 5.82: AA6061 / $Al_2O_3$ foamed to maximum expansion at 804°C

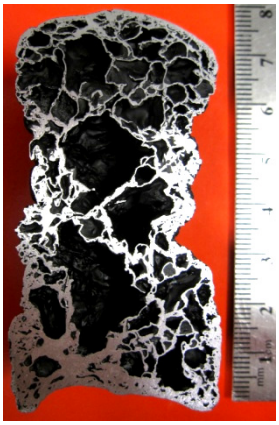

Figure 5.83: AA6061 / $Al_2O_3$ foam overaged at 804°C

Similarly, A356 / $Al_2O_3$ maximum expansion foams at the lower foaming temperature show some longitudinally elongated pores; however, they are distributed throughout the foam. Maximum expansion foams at the higher foaming temperature show a comparatively narrow pore size distribution with relatively equiaxed foam cells. The overaged foams at both foaming temperatures show typical behaviour with significant collapse, particularly at 764°C.

AA6061 / $Al_2O_3$ foams in all conditions show several large, fairly polygonal pores in addition to smaller cells. The overaged foams at 804°C show severely caved-in sides of the foam. They furthermore typically exhibit a concave bottom with noticeable drainage. The concave bottom is likely the result of the foam cooling from the top down after the crucible has been removed from the furnace. Large pores in the center of the foam shrink with decreasing temperature and the remaining liquid or semi-solid alloy at the bottom of the foam follows this contraction.

In terms of foam quality, large pores in the center of foams are very undesirable, as they will dominate the mechanical properties. Therefore, the A356 / $Al_2O_3$ foams produced to maximum expansion must be seen as the best quality samples among



alumina stabilized foams, as they show large expansion (i.e. low density) as well as a narrow pore size distribution and no significant drainage. However, considering the corresponding 5-minutes-overaged foams, it becomes clear that this composition has only a very narrow window to obtain good pore morphology and mechanical properties. Hence, the foam stability and tolerance against overaging of these A356 / $Al_2O_3$ foams is not particularly good, even though they reach the largest expansion among all tested systems.

### 5.4.2 Silicon Carbide Stabilized Foams

The expansion curves of SiC stabilized pure aluminum, Al-11.5Si, Al-7Cu, and Al-1Mg foams are presented in Figures 5.84 to 5.91. In general, they appear similar to those involving alumina as stabilizing particles.

After an initial period of 70s to 150s, the expansion curves exhibit two subsequent expansion stages, a maximum expansion stage, and a foam collapse stage. During the first expansion stage severe dome-formation of the top and the bottom of the compact occur. In several cases, a very pronounced plateau can be observed between the two expansion stages. The reason for this is that the domes that developed at the top and the bottom of the sample decline while the compact expands in all directions. Once the crucible diameter is filled, the second expansion stage is characterized by the majority of the volume gains.

Three important differences to aluminum alloy foams containing alumina as stabilizing particles can be observed:

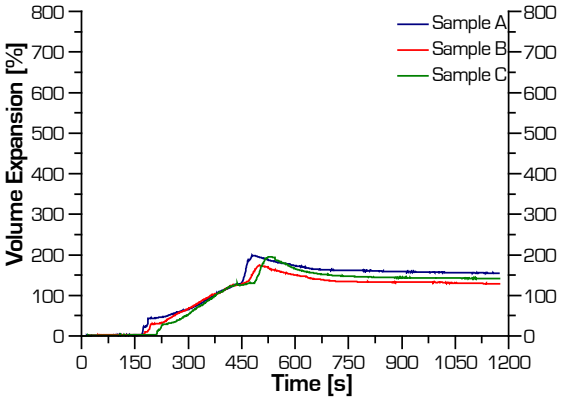


Figure 5.84: Foam expansion curves for Al-99.99 with 1wt.% $TiH_2$ and 8vol.% SiC at 750°C

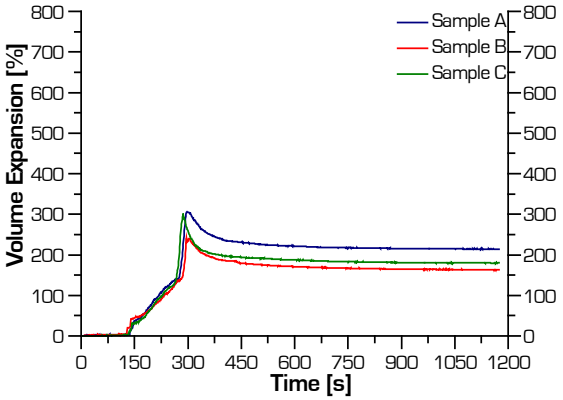


Figure 5.85: Foam expansion curves for Al-99.99 with 1wt.% $TiH_2$ and 8vol.% SiC at 800°C

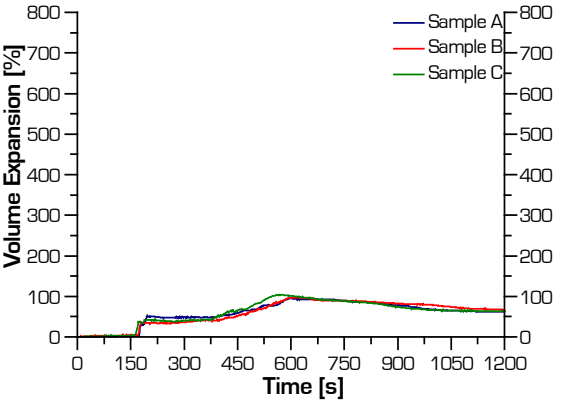


Figure 5.86: Foam expansion curves for Al-11.5Si with 1wt.% $TiH_2$ and 8vol.% SiC at 688°C

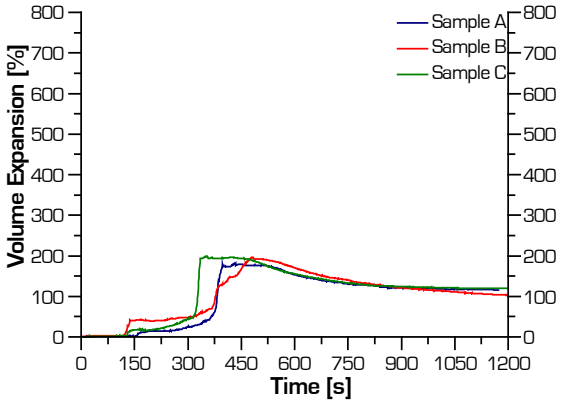


Figure 5.87: Foam expansion curves for Al-11.5Si with 1wt.% $TiH_2$ and 8vol.% SiC at 738°C

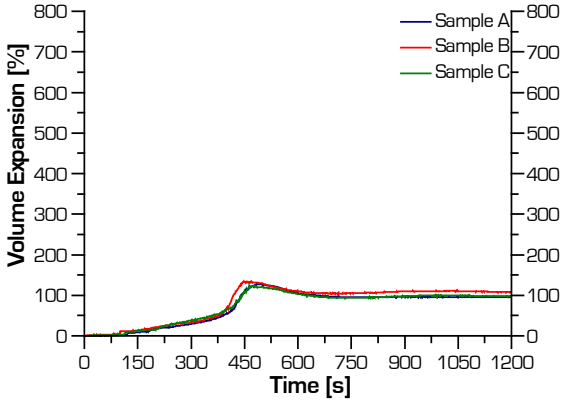


Figure 5.88: Foam expansion curves for Al-7Cu with 1wt.% $TiH_2$ and 8vol.% SiC at 729°C

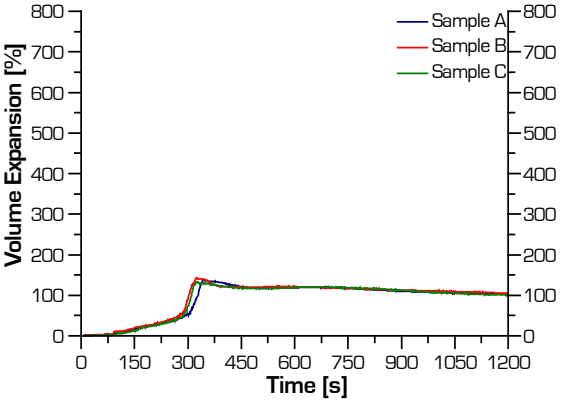


Figure 5.89: Foam expansion curves for Al-7Cu with 1wt.% $TiH_2$ and 8vol.% SiC at 779°C

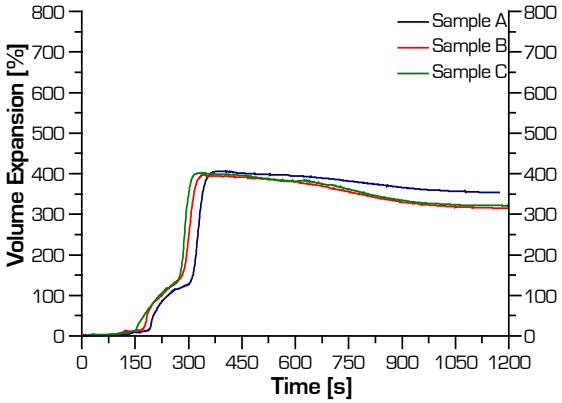


Figure 5.90: Foam expansion curves for Al-1Mg with 1wt.% $TiH_2$ and 8vol.% SiC at 748°C

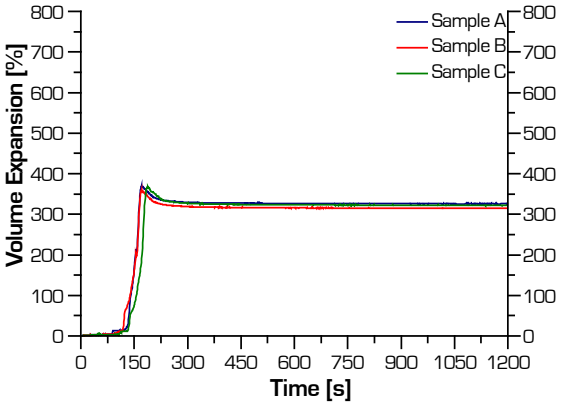


Figure 5.91: Foam expansion curves for Al-1Mg with 1wt.% $TiH_2$ and 8vol.% SiC at 798°C

Overall, foams stabilized by silicon carbide particles at both respective foaming temperatures exhibit noticeably less expansion than the equivalent composition with alumina particles. The differences in maximum foam expansion are approximately 40% less volume expansion at 750°C and 60% less at 800°C for Al-99.99 foams, 150% less at 688°C and over 200% less at 738°C for Al-11.5Si foams, almost 200% less expansion at both temperatures for Al-7Cu foams, and approximately 40% less expansion at 748°C and almost 200% less at 798°C for Al-1Mg foams.

It is very noticeable that SiC stabilized Al-7Cu foams show no significant difference in the expansion curves between the two different foaming temperatures, while Al-1Mg / SiC foams actually show lower expansion at the higher foaming temperature than at the lower one. This is unexpected as metal foams generally exhibit larger expansion if the time delay between foaming agent decomposition and metal melting is shorter, i.e. if the heat input is faster, less foaming gas is lost through cracks in the still (semi-) solid compact.

Furthermore, SiC stabilized foams show significantly less volume shrinkage during the foam collapse stage than the equivalent alumina stabilized foams. Al-11.5Si / SiC foams at the lower foaming temperature as well as Al-7Cu / SiC foams even appear to exhibit a further slight expansion after foam collapse occurred. This apparent foam

stability well beyond maximum foam expansion and therefore tolerance against overaging is very interesting because it allows a wider window for foam production.

When the pore morphology images at maximum expansion as well as at 5 minutes beyond maximum expansion of Al-7Cu / SiC (Figures 5.100 to 5.103) and particularly Al-11.5Si / SiC (Figures 5.96 to 5.99) are examined, the high densities and low expansion of these foams are evident. The Al-11.5Si / SiC foams at 688°C (Figures 5.96 and 5.97) furthermore show very crack-like pores, which at 738°C simply seem to be cleaved open further. In cross-section, Al-11.5Si / SiC foams are generally characterized by a smaller number of pores than other compositions featuring SiC and even more so in comparison to alumina stabilized foams.

In the case of Al-7Cu / SiC, the foam cross-sections show fewer crack-like pores, however, the foam morphologies still appear very irregular. Moreover, the few large pores will dominate the mechanical properties.

Figure 5.92: Al-99.99 / SiC foamed to maximum expansion at 750°C

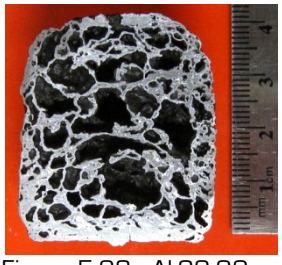

Figure 5.93: Al-99.99 / SiC foam overaged at 750°C

Figure 5.94: Al-99.99 / SiC foamed to maximum expansion at 800°C

Figure 5.95: Al-99.99 / SiC foam overaged at 800°C

Figure 5.96: Al-11.5Si / SiC foamed to maximum expansion at 688°C

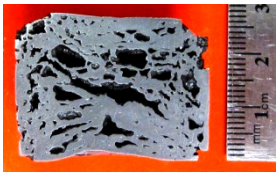

Figure 5.97: Al-11.5Si / SiC foam overaged at 688°C

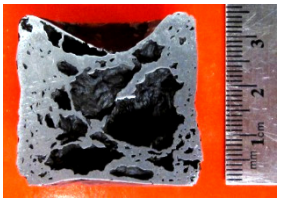

Figure 5.98: Al-11.5Si / SiC foamed to maximum expansion at 738°C

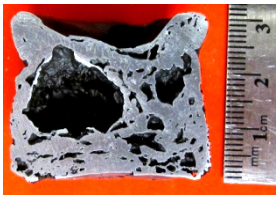

Figure 5.99: Al-11.5Si / SiC foam overaged at 738°C

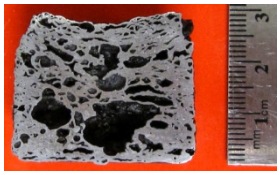

Figure 5.100: Al-7Cu / SiC foamed to maximum expansion at 729°C

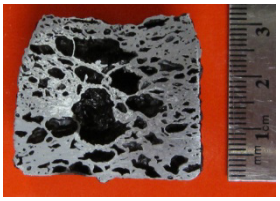

Figure 5.101: Al-7Cu / SiC foam overaged at 729°C

Figure 5.102: Al-7Cu / SiC foamed to maximum expansion at 779°C

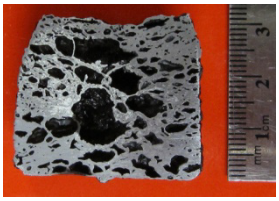

Figure 5.103: Al-7Cu / SiC foam overaged at 779°C

Figure 5.104: Al-1Mg / SiC foamed to maximum expansion at 748°C

Figure 5.105: Al-1Mg / SiC foam overaged at 748°C

Figure 5.106: Al-1Mg / SiC foamed to maximum expansion at 798°C

Figure 5.107: Al-1Mg / SiC foam overaged at 798°C

Judging from the longitudinal cross-sections, particularly of the Al-99.99 / SiC (Figures 5.92 to 5.95) and Al-1Mg / SiC foams (Figures 5.104 to 5.107), it seems that the stability of the overall foams that is apparent in the expansion curves is not accompanied by improved cell wall stability. On the contrary, the overaged foams are characterized by a large number of collapsed cells, missing cell walls, and irregular pore shapes. Drainage of the liquid towards to bottom of the foam is noticeable only in case of the all Al-99.99 / SiC foams, and the Al-1Mg / SiC foams at 798°C. However, even here this phenomenon is significantly less pronounced than in foams stabilized by alumina.

Among the aluminum alloy foams containing silicon carbide particles, only the Al-1Mg foams produced for maximum expansion at both foaming temperatures exhibit comparatively even pore sizes and the most equiaxed foam cells.

The foam expansion performance of the SiC stabilized foams in this work, in general, is weaker than what has been presented in literature[111,112], where significantly better foam morphologies and overall expansions have been reported, particularly for aluminum-silicon alloy / SiC foams. The reason for this is likely that the silicon carbide powder used has, with 0.7wt.% oxygen, a considerable degree of oxidation. This results in the surface of the powder being $SiO_2$ rather than SiC. Furthermore, despite literature generally using higher foaming temperatures for aluminum-silicon compacts, Al-11.5Si foams in this study were produced at comparatively low temperature, in order to maintain analogous foaming conditions for all compositions (foaming temperatures at 90°C and 140°C above melting or liquidus temperature of the metal or alloy).

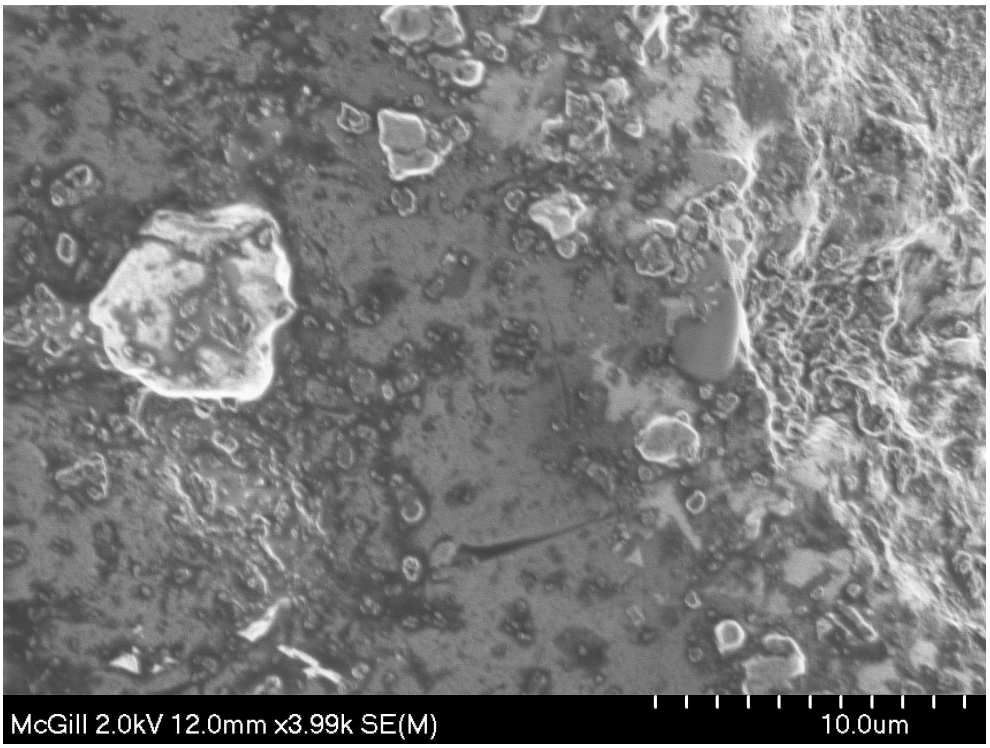


Figure 5.108: SEM micrograph of an Al-7Cu / SiC foam foamed to maximum expansion at 729°C. Wide SiC particle size distribution visible

Micrographs of foams stabilized by silicon carbide particles (such as that of an Al-7Cu / SiC foam presented in Figure 5.108) show evidence of a wide range of ceramic particle sizes. A large fraction of the visible silicon carbide particles appear to be a fraction of the 5µm $d_{50}$ nominal particle size and the powder seems to have a wider distribution of sizes than the alumina powder. This is supported by particle size analyses of the alumina and silicon carbide powders presented in Figure 5.109. As can be seen from the graph, not only do both powders have a larger than nominal particle size with 8µm for alumina, and 8.7µm for silicon carbide, but also the distribution of the latter ranges from 0.2µm to 70µm while that of the former ranges from 0.45µm to 19µm.

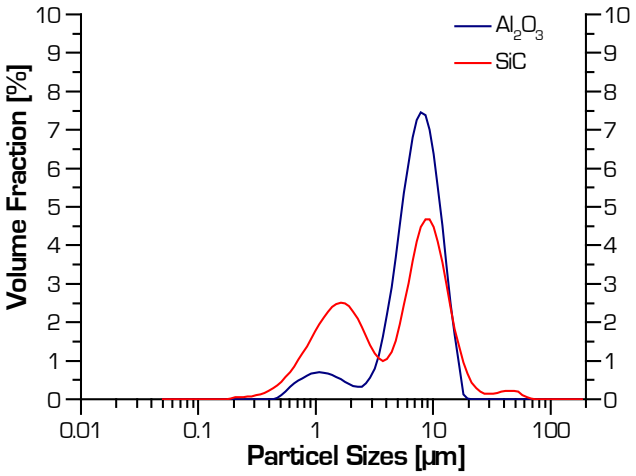


Figure 5.109: Particle size distributions of the alumina and silicon carbide particles added to the powder mixtures, from which the metal foam precursors were compacted.

Due to their large surface area per volume, the small silicon carbide particles likely react rapidly with the liquid aluminum alloy and thus are fully immersed in the latter. Particles that do not protrude the interface do not act as stabilizers[89,113], rather they likely increase the viscosity of the liquid metal noticeably during foaming. This may well be the reason for the crack-like pore shapes observed in foams produced at lower temperatures and the insignificant drainage observed in silicon carbide stabilized foams.

## 5.5 *KAPTAY*'S MODELS

*KAPTAY*'s theory[4,8,12] linking contact angles and foam stability suggests that those liquid metal / solid particle combinations that exhibit contact angles in the range of 70° to 86° should form the most stable foams. It is commonly believed that the more stable the foam is while the metal is liquid, the more even its pore morphology, the narrower the pore size distribution and the more resistant the composition is against overaging. Based on this model and the wetting behaviour presented in section 5.3, Al-1Mg / $Al_2O_3$ and Al-11.5Si / $Al_2O_3$ foams should be less stable than A356 / $Al_2O_3$, AA6061 / $Al_2O_3$, pure aluminum / $Al_2O_3$, and particularly Al-7Cu / $Al_2O_3$ foams, as only the latter reach the proposed optimum contact angle range as can be seen from Figures 5.17 and 5.18. None of the investigated wetting systems involving silicon carbide substrates reached the 70° to 86° contact angle range; Al-11.5Si / SiC and Al-7Cu / SiC, however came close. Therefore, it is not surprising to see higher overall

expansions in the case of alumina particle addition than with added SiC particles to the powder mixtures.

As has been shown in section 5.4, A356 / $Al_2O_3$, AA6061 / $Al_2O_3$, and Al-1Mg / $Al_2O_3$ foams reach the highest maximum foam expansions among the precursor compositions containing alumina particles at both temperatures, and show the most advantageous pore morphologies at maximum expansion. Al-7Cu / $Al_2O_3$ and, to lesser extent, A356 / $Al_2O_3$ show the highest tolerance against overaging. *ASAVAVISITHCHAI* and *KENNEDY*[11] have reported similar findings, where improved foam expansion was obtained from the addition of magnesium to aluminum foams that contain $Al_2O_3$ and were produced via the PM route.

Among the silicon carbide stabilized foams, Al-1Mg / SiC shows the highest expansions, while in terms of pore morphology, none show reasonable tolerance to overaging, despite the overall expansion not showing as significant degrees of foam collapse as most alumina stabilized foams.

SEM micrographs of maximum expansion foams of Al-99.99 / $Al_2O_3$, Al-11.5Si / $Al_2O_3$, Al-7Cu / $Al_2O_3$, and Al-1Mg / $Al_2O_3$ are presented in Figures 5.110 to 5.113.

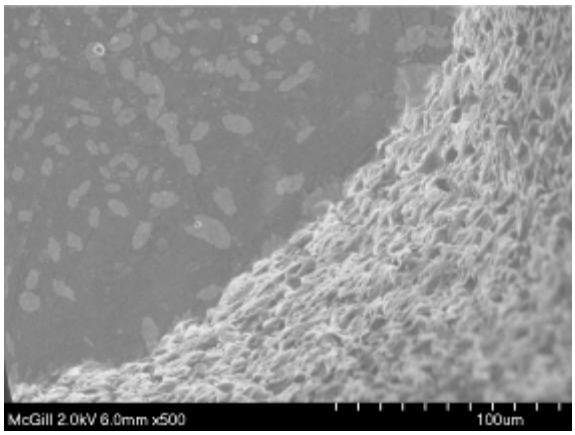


Figure 5.110: SEM micrograph of a polished section through an Al99.99 / $Al_2O_3$ foam produced to maximum expansion at 750°C

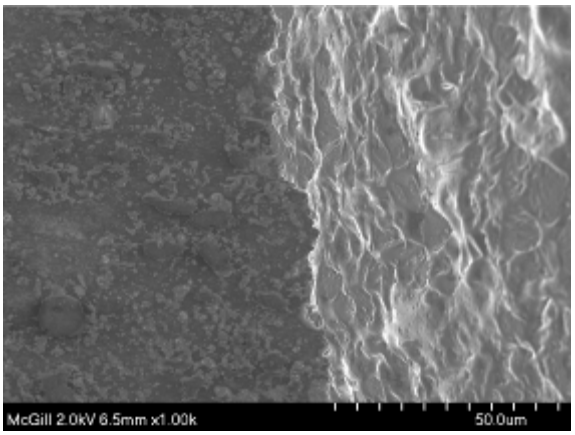


Figure 5.111: SEM micrograph of a polished section through an Al-11.5Si / $Al_2O_3$ foam produced to maximum expansion at 688°C

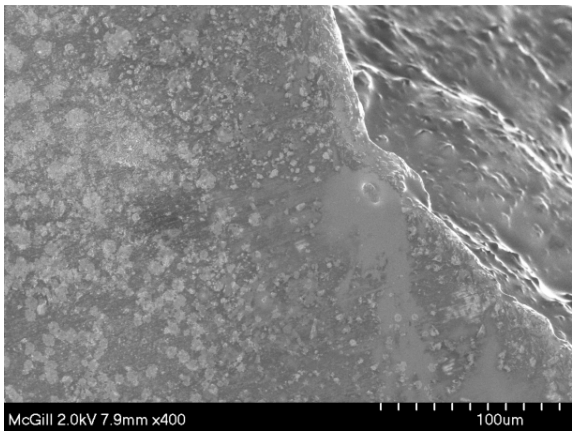


Figure 5.112: SEM micrograph of a polished section through an Al-7Cu / $Al_2O_3$ foam produced to maximum expansion at 729°C

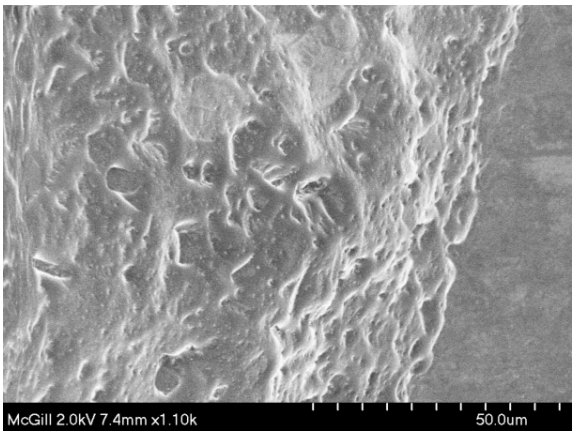


Figure 5.113: SEM micrograph of a polished section through an Al-1Mg / $Al_2O_3$ foam produced to maximum expansion at 748°C

It can be seen from the micrographs that better foam stability, quality, and expansion seem to go along with the alumina particles being embedded deeper in the cell walls, thus yielding a smoother and less faceted interface; Al-1Mg / $Al_2O_3$ and Al-7Cu / $Al_2O_3$ foams show noticeably smoother cell walls than Al-99.99 / $Al_2O_3$ and Al-11.5Si / $Al_2O_3$ foams. This is in agreement with *ASAVAVISITHCHAI* and *KENNEDY*[11], as well as *KAPTAY*[8], and must be interpreted as improved in-situ wetting in the Al-1Mg / $Al_2O_3$ system over the Al-99.99 / $Al_2O_3$ system during foaming. From Figure 5.114, a polished section of an A356 / $Al_2O_3$ foam, however, it can be seen that in the case of the composition that yields the largest maximum expansion and the best pore morphology among all tested systems, the stabilizing alumina particles protrude quite far into the cell wall, resulting in a rough interface. In the case of AA6061 / $Al_2O_3$ foams (Figure 5.115), the particles protrude even further into the cell wall than in the case of A356 / $Al_2O_3$. However, it is possible that in these two cases the remaining cell wall thickness is so small that the stabilizing particles are essentially forced into the cell, thus forming dense 3D networks (Figure 5.115).

It remains unclear whether the particle arrangement along the interface (closely packed single layer, closely packed double layer, or 3D networks) is a function of the

alloy / ceramic particle combination, the wetting behaviour or the density of particles in the cell walls.

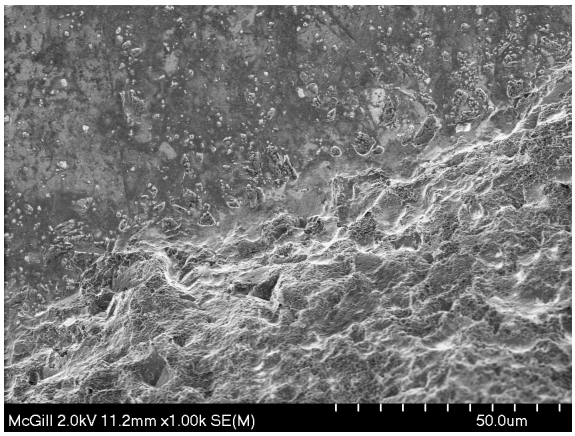


Figure 5.114: SEM micrograph of a polished section through an A356 / $Al_2O_3$ foam produced to maximum expansion at 714°C

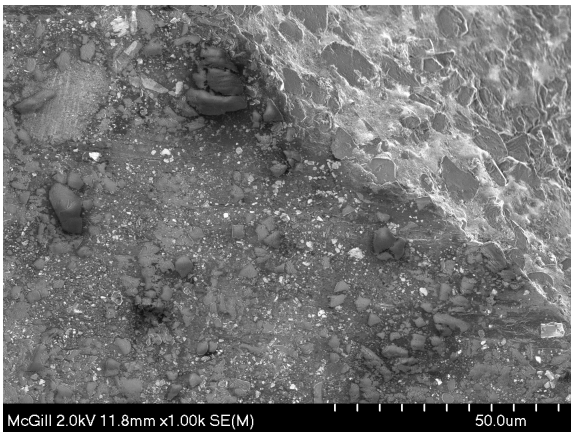


Figure 5.115: SEM micrograph of a polished section through an AA6061 / $Al_2O_3$ foam produced to maximum expansion at 754°C

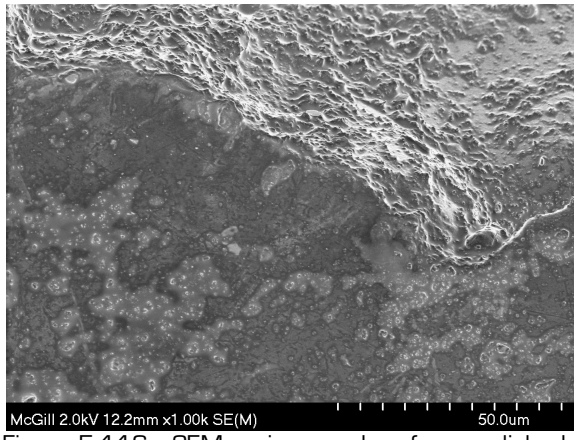


Figure 5.116: SEM micrograph of a polished section through an Al-99.99 / SiC foam produced to maximum expansion at 750°C

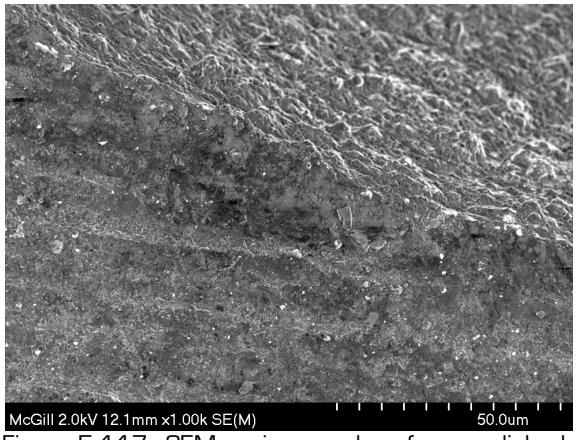


Figure 5.117: SEM micrograph of a polished section through an Al-1Mg / SiC foam produced to maximum expansion at 748°C

Similar SEM micrographs of foams, stabilized by silicon carbide particles (Figures 5.116 and 5.117), show comparatively rough cell wall morphologies.

It therefore appears that smooth cell wall structures in foams and apparently good in-situ wetting between liquid metal and stabilizing particles often go along with large

foam expansion, which can be accompanied by good tolerance against overaging; however, as can be seen from the results presented above, this is not a consistent trend.

Furthermore, the in-situ wetting behaviour is significantly different from that observed during the high vacuum wetting experiments shown in section 5.3. Thus, the conditions during foaming are sufficiently different to cause clearly different wetting behaviour. This difference is easy to understand, considering that the wetting experiments were conducted under vacuum while the foaming experiments were conducted under standard atmosphere and hence very different oxygen availability. Moreover, the presence of oxide layers around the aluminum powder particles in the foaming precursors adds to the significant difference in oxygen activities between idealized wetting experiments and in-situ wetting during foaming. The wetting behaviour is severely susceptible to oxygen activity in the system, as has been shown in section 5.3.2.

Hence, based on the contact angle behaviour of the tested alloy / ceramic particle combinations, *KAPTAY*'s model[8] does not predict the foam stability / quality sequence correctly for the investigated combinations. It therefore appears that additional factors beyond *KAPTAY*'s models affect metal foam expansion and stability more than the wetting behaviour alone. The theory, which has been supported by experimental simulations using aqueous solutions to mimic the liquid metal and polymer or ceramic particles to simulate the ceramic particles[5,90], seems to agree with the in-situ wetting behaviour in several cases and is conclusive. Nevertheless, it appears that in the case of aluminum alloy foams containing ceramic particles, wetting experiments under idealized experimental conditions are insufficient to grasp all reaction processes occurring during foaming under standard atmosphere. Most importantly, however, *KAPTAY*'s models do not suggest which factors influence particle arrangements. Therefore, even knowledge of in-situ wetting behaviour between metal and stabilizing particles is insufficient to predict good foam morphologies with certainty.



Wetting experiments involving aluminum and its alloys under standard atmosphere are irrelevant, because they will not yield true equilibrium contact angles (as has been explained in section 2.2.5). However, it might be interesting to see if, during foaming experiments under inert gas atmosphere with significantly reduced oxygen partial pressure, closer correlation can be achieved between the contact angles measured in idealized experiments and the in-situ wetting behaviour.

# 6 CONCLUSIONS

## 6.1 WETTING EXPERIMENTS

The conducted wetting experiments show that pure aluminum as well as all investigated aluminum alloys exhibit contact angles which, within experimental error, can be considered identical on polycrystalline alumina and single-crystalline A-plane sapphire substrates of equivalent surface roughness. As has been explained, this is understandable considering the very similar surface free energies of alumina and sapphire, which differ only due to the presence of grain boundaries (or the lack thereof) and crystallographic orientation.

For pure aluminum, aluminum-copper alloys, AA6061, and A356 the contact angles on $Al_2O_3$ change significantly and well into the non-wetting regime upon approaching the melting point or the liquidus temperature, respectively. With increasing temperatures, each system seems to approach a threshold value. At 700°C, the measured contact angles of aluminum on $Al_2O_3$ were close to the literature value of 90°. This clearly validates the present methodology.

For Al-11.5Si / $Al_2O_3$, and Al-1Mg / $Al_2O_3$, the contact angles found just above their respective liquidus temperatures remain roughly the same values as those at higher temperatures. Thus, even small additions of alloying elements to aluminum can significantly alter both the temperature dependent behaviour of the wetting system as well as the measured contact angles at a given temperature.



On silicon carbide, pure aluminum and all investigated alloys, with the exception of Al-1Mg, exhibited strongly temperature dependent contact angle behaviour, with asymptotically decreasing values with higher temperatures. Other than on $Al_2O_3$, for Al-11.5Si on SiC constant wetting behaviour was not observed. The measured equilibrium contact angle of Al-99.99 / SiC remained significantly higher than what has been published in literature.

It has been found that the aluminum (alloy) / SiC wetting systems presented in section 5.3.4 are more reactive than reported by other researchers. This is caused by cleaner experiments, as the current wetting furnace setup dispenses liquid metal drops freed of their natural oxide layers and because the substrate preparation method resulted in silicon carbide with minute protective $SiO_2$ coverage. Consequently, the reaction between the drop and the substrate was so rapid that within minutes (possibly even seconds), the drop dug itself into the substrate, pinning the triple line and preventing an equilibrium contact angle to form with the unperturbed substrate surface.

The present results for wetting of aluminum-copper alloys on sapphire demonstrated a decrease in contact angles from pure aluminum to low copper contents and a subsequent increase towards higher copper additions. Coinciding with the wetting experiments was a significant increase in interface roughness after the short-term wetting tests, and particularly after the long-term experiments. The occurrence of chemical reactions at the interface between the liquid alloy and residual furnace oxygen has been confirmed by FactSage thermodynamic simulations, HRTEM, XPS, and AFM. FactSage modeling and AFM profiles of the interface rule out that the formation of precipitates from the liquid metal is related to an oxygen-rich Al-O interphase at the interface. Nevertheless, $Al_2O$ is believed to form between the liquid aluminum (alloy) and the $Al_2O_3$ substrate, as a noticeable *etching* effect pronounces asperities and scratches in the substrate underneath the sessile drop.

## 6.2 FOAMING EXPERIMENTS

Using $TiH_2$ as blowing agent, metal foams were produced via the PM route from the same metal / ceramic particle systems with which the wetting experiments have been conducted. Foam expansion curves as well as macrostructures of interrupted foaming experiments were employed to evaluate foam quality and stability. It has been found that A356 / $Al_2O_3$ foams achieve the highest maximum expansions, while porous metals from Al-7Cu / $Al_2O_3$ appear to have the highest tolerance against overaging.

The SiC stabilized foams, presented in section 5.4.2, show significantly less expansion than has been reported for similar foams in literature. The apparently good tolerance of SiC stabilized foams against overaging observed from the expansion curves is not supported by pore morphology evaluations.

## 6.3 *KAPTAY*'S MODELS

Among the investigated alloy / ceramic particle wetting systems, Al-7Cu / $Al_2O_3$ and AA6061 / $Al_2O_3$ appeared most promising to produce good quality foams, as these were the only systems that comfortably reached the contact angle range deemed most promising for metal foam stabilization by *KAPTAY*. From the foaming results, it must be concluded that the in-situ wetting behaviour during foaming of the metal on the stabilizing particles is significantly different from the wetting behaviour observed in the idealized wetting experiments. Wetting experiments under idealized conditions are therefore unsuitable to predict the performance during foaming.

As has been shown, A356 / $Al_2O_3$, and AA6061 / $Al_2O_3$ form 3D networks of particles at the interface between liquid metal and gas bubble. These networks can stabilize foams virtually irrespective of the wetting behaviour of the according system. There-



fore, even the observed in-situ wetting behaviour cannot be related to foaming performance.

Thus, it must be concluded that in the case of aluminum foams, processes and factors play significant roles during foaming and in foam stabilization that are not sufficiently considered in *KAPTAY*'s theory, despite this theory seemingly applying well to aqueous foams, as has been shown in literature.

# 7 CONTRIBUTIONS TO ORIGINAL KNOWLEDGE

The presented work includes, to the best of the candidate's knowledge, the first in-detail description of a horizontal wetting furnace featuring a drop dispensing arrangement. This setup combines several advantages over other wetting setups currently employed by other research groups. It reaches significantly higher vacuums than similar systems with a vertical arrangement in a box furnace. This is not only because a box furnace has a significantly larger volume and more surface area that needs to be sealed, but also because these systems feature a plunger as drop-injection mechanism. Moving parts that break the vacuum system are always sources of leaks.

The present wetting results are novel. The employed interface characterization techniques, as well as the thermodynamic simulation work have not been presented in this context before. Particularly, the proof that, even in very controlled environments, wetting experiments with aluminum and its alloys on $Al_2O_3$ must not be considered non-reactive, is a very important finding. The clear identification of residual furnace oxygen transported along the interface to be the source of the higher than expected oxygen activity at the interface, causing the chemical reactions that accompany wetting in these systems, is important and new.

Moreover, to the best of the candidate's knowledge, the present work is the first, where aluminum (alloy) on silicon carbide wetting systems were sufficiently clean, for the reactivity of these systems to prevent them from attaining equilibrium.



Lastly, the present work showed clearly that not only is the wetting behaviour of the liquid metal on stabilizing ceramic particles in metal foams not the dominating characteristic determining foam quality, but also has it been shown that knowledge of the wetting behaviour of a liquid metal / ceramic substrate system under idealized conditions is insufficient to predict foaming performance.

# REFERENCES


[1] J. Banhart, "Manufacture, Characterisation and Application of Cellular Metals and Metal Foams", *Progress in Materials Science* **46** (6), 559-632 (2001).

[2] N. Babcsán, D. Leitlmeier, and J. Banhart, "Metal foams - High Temperature Colloids Part I. Ex Situ Analysis of Metal Foams", *Colloids and Surfaces A: Physicochemical and Engineering Aspects* **261** (1-3), 123-130 (2005).

[3] D. Weaire and S. Hutzler, *The Physics of Foams*, 1st ed. (Clarendon Press, Oxford (UK), 1999).

[4] G. Kaptay, "Interfacial Criteria for Ceramic Particle Stabilised Metallic Foams", presented at the *International Conference for Metal Foams and Porous Metal Structures*, Bremen (Germany), (MIT Press, 1999).

[5] Y. Q. Sun and T. Gao, "The Optimum Wetting Angle for the Stabilization of Liquid-Metal Foams by Ceramic Particles: Experimental Simulations", *Metallurgical and Materials Transactions A: Physical Metallurgy and Materials Science* **33** (10), 3285-3292 (2002).

[6] T. Wübben, H. Stanzick, J. Banhart, and S. Odenbach, "Stability of Metallic Foams Studied under Microgravity", *Journal of Physics: Condensed Matter* **15** (1), 427-433 (2003).

[7] N. Babcsán, D. Leitlmeier, H. P. Degischer, and J. Banhart, "The Role of Oxidation in Blowing Particle-Stabilised Aluminium Foams", *Advanced Engineering Materials* **6** (6), 421-428 (2004).

[8] G. Kaptay, "Interfacial Criteria for Stabilization of Liquid Foams by Solid Particles", *Colloids and Surfaces A: Physicochemical and Engineering Aspects* **230** (1-3), 67-80 (2004).

[9] A. R. Kennedy and S. Asavavisithchai, "Effect of Ceramic Particle Additions on Foam Expansion and Stability in Compacted Al-$TiH_2$ powder precursors", *Advanced Engineering Materials* **6** (6), 400-402 (2004).

[10] T. Wübben and S. Odenbach, "Stabilisation of Liquid Metallic Foams by Solid Particles", *Colloids and Surfaces A: Physicochemical and Engineering Aspects* **266** (1-3), 207-213 (2005).



[11] S. Asavavisithchai and A. R. Kennedy, "The effect of Mg addition on the stability of Al-$Al_2O_3$ foams made by a powder metallurgy route", *Scripta Materialia* **54** (7), 1331-1334 (2006).

[12] G. Kaptay, "On the Equation of the Maximum Capillary Pressure Induced by Solid Particles to Stabilize Emulsions and Foams and on the Emulsion Stability Diagrams", *Colloids and Surfaces A: Physicochemical and Engineering Aspects* **282-283**, 387-401 (2006).

[13] J. J. Brennan and J. A. Pask, "Effect of Nature of Surfaces on Wetting of Sapphire by Liquid Aluminum", *Journal of the American Ceramic Society* **51** (10), 569-573 (1968).

[14] H. John and H. Hausner, "Influence of Oxygen Partial Pressure on the Wetting Behaviour in the System Al/$Al_2O_3$", *Journal of Materials Science Letters* **5** (5), 549-551 (1986).

[15] V. Laurent, D. Chatain, C. Chatillon, and N. Eustathopoulos, "Wettability of Monocrystalline Alumina by Aluminium between its Melting Point and 1273 K", *Acta Metallurgica* **36** (7), 1797-1803 (1988).

[16] D. A. Weirauch, Jr., "Interfacial Phenomena Involving Liquid Metals and Solid Oxides in the Mg-Al-O System", *Journal of Materials Science* **3** (4), 729-739 (1988).

[17] S. M. Wolf, A. P. Levitt, and J. Brown, "Whisker-Metal Matrix Bonding", *Chemical Engineering Progress* **62** (3), 74-78 (1966).

[18] D. Leitlmeier, H. P. Degischer, and H. J. Flankl, "Development of a Foaming Process for Particulate Reinforced Aluminum Melts", *Advanced Engineering Materials* **4** (10), 735-740 (2002).

[19] I. Jin, L. D. Kenny, and H. Sang, Canada, Patent No. WO 91/03578 (1991).

[20] L. D. Kenny and M. Thomas, Canada, Patent No. WO 91/03578 (1994).

[21] R. Montanini, "Measurement of strain rate sensitivity of aluminium foams for energy dissipation", *International Journal of Mechanical Sciences* **47** (1), 26-42 (2005).

[22] P. Åsholt, "Aluminium Foam Produced by the Melt Foaming Route - Process, Properties and Applications", presented at the *International Conference for Metal Foams and Porous Structures 1999*, Bremen (Germany), (MIT-Verlag, 1999).

[23] L. M. Niebylski, C. P. Jarema, and T. E. Lee, USA, Patent No. US3843353 (1974).

[24] S. Akiyama, K. Imagawa, A. Kitahara, S. Nagata, K. Morimoto, T. Nishikawa, and M. Itoh, Japan, Patent No. EP0210803 (1987).


[25] F. Baumgartner, I. Duarte, and J. Banhart, "Industrialization of Powder Compact Foaming Process", *Advanced Engineering Materials* **2** (4), 168-174 (2000).

[26] P. M. Proa-Flores and R. A. L. Drew, "Production of Aluminum Foams with Ni-coated $TiH_2$ Powder", *Advanced Engineering Materials* **10** (9), 830-834 (2008).

[27] D. Lehmhus and M. Busse, "Potential new Matrix Alloys for Production of PM Aluminium Foams", *Advanced Engineering Materials* **6** (6), 391-396 (2004).

[28] M. F. Ashby, *Metal Foams: A Design Guide*. (Butterworth-Heinemann, Boston (USA), 2000).

[29] U. Ramamurty and A. Paul, "Variability in Mechanical Properties of a Metal Foam", *Acta Materialia* **52** (4), 869-876 (2004).

[30] J. S. Blazy et al., "Deformation and Fracture of Aluminium Foams under Proportional and Non Proportional Multi-Axial Loading: Statistical Analysis and Size Effect", *International Journal of Mechanical Sciences* **46** (2), 217-244 (2004).

[31] E. W. Andrews and L. J. Gibson, "The Influence of Cracks, Notches and Holes on the Tensile Strength of Cellular Solids", *Acta Materialia* **49** (15), 2975-2979 (2001).

[32] W. D. J. Callister, *Materials Science and Engineering - an Introduction*, 4th ed. (John Wiley & Sons, New York (USA), 1997).

[33] J. Baumeister, J. Banhart, and M. Weber, "Aluminium Foams for Transport Industry", *Materials & Design* **18** (4-6), 217-220 (1997).

[34] G. J. Davies and S. Zhen, "Metallic Foams: Their Production, Properties and Applications", *Journal of Materials Science* **18** (7), 1899-1911 (1983).

[35] L. J. Gibson and M. F. Ashby, *Cellular Solids - Structure and Properties*, 2nd ed. (Cambridge University Press, Cambridge (UK), 1997).

[36] J. Banhart, "Aluminium Foams for Lighter Vehicles", *International Journal of Vehicle Design* **37** (2-3), 114-125 (2005).

[37] A. Fuganti, L. Lorenzi, A. G. Hanssen, and M. Langseth, "Aluminium Foam for Automotive Applications", *Advanced Engineering Materials* **2** (4), 200-204 (2000).

[38] H. W. Seeliger, "Aluminium Foam Sandwich (AFS) Ready for Market Introduction", *Advanced Engineering Materials* **6** (6), 448-451 (2004).

[39] F. Moussy, "*Car Manufacturing: Materials Choices and Materials Research for the Future*", NESMI Conference: Minerals for a sustainable and competitive Europe, 24. April 2006



[40] C. Kammer, "TALAT Lecture 1410 - Aluminium Foam", *European Aluminium Association* (1999).

[41] Unknown, in *Cymat Technologies Ltd. - Management's Discussion and Analysis ("MD&A") as at January 31, 2009* (Mississauga, Ontario, Canada, 2009).

[42] H. Lüth, *Solid Surfaces, Interfaces and Thin Films*, fourth ed. (Springer-Verlag, Berlin (Germany), 2001).

[43] J. B. Hudson, *Surface Science - An Introduction*. (Butterworth-Heinemann, Stoneham (USA), 1992).

[44] R. Holze, *Surface and Interface Analysis - An Electrochemists Toolbox*. (Springer-Verlag, Berlin (Germany), 2009).

[45] K. Holmberg and A. Matthews, *Coatings Tribology - Properties, Mechanisms, Techniques and Applications in Surface Engineering*, second ed. (Elsevier, Amsterdam (Netherlands), 2009).

[46] P. G. B.-W. de Gennes, F.; Quéré, D., *Capillarity and Wetting Phenomena - Drops, Bubbles, Pearls, Waves*, translated ed. (Springer, New York (USA), 2004).

[47] J. R. Rosen, *Surfactants and Interfacial Phenomena*, 3rd ed. (John Wiley & Sons, Inc., Hoboken (USA), 2004).

[48] B. J. Dalgleish, E. Saiz, A. P. Tomsia, R. M. Cannon, and R. O. Ritchie, "Interface Formation and Strength in Ceramic-Metal Systems", *Scripta Metallurgica Et Materialia* **31** (8), 1109-1114 (1994).

[49] V. Gupta, A. S. Argon, and J. A. Cornie, "Interfaces with Controlled Toughness as Mechanical Fuses to Isolate Fibres from Damage", *Journal of Materials Science* **24** (6), 2031-2040 (1989).

[50] T. R. Jonas, J. A. Cornie, and K. C. Russell, "Infiltration and Wetting of Alumina Particulate Preforms by Aluminum and Aluminum-Magnesium Alloys", *Metallurgical and Materials Transactions a-Physical Metallurgy and Materials Science* **26** (6), 1491-1497 (1995).

[51] M. Rühle and A. G. Evans, "Structure and Chemistry of Metal/Ceramic Interfaces", Newport, RI, USA, 1989).

[52] J. M. Howe, "Bonding, Structure, and Properties of Metal/Ceramic Interfaces: Part I. Chemical Bonding, Chemical Reaction, and Interfacial Structure", *International Materials Reviews* **38** (5), 233-256 (1993).

[53] N. Eustathopoulos, M. G. Nicholas, and B. Drevet, *Wettability at High Temperatures*, 1st ed. (Pergamon, Amsterdam (Netherlands), 1999).

[54] R. Furstner, W. Barthlott, C. Neinhuis, and P. Walzel, "Wetting and Self-Cleaning Properties of Artificial Superhydrophobic Surfaces", *Langmuir* **21** (3), 956-961 (2005).

[55] N. Eustathopoulos, "Progress in understanding and modeling reactive wetting of metals on ceramics", *Current Opinion in Solid State and Materials Science* **9** (4-5), 152-160 (2005).

[56] K. Landry, S. Kalogeropoulou, N. Eustathopoulos, Y. Naidich, and V. Krasovsky, "Characteristic contact angles in the aluminium/vitreous carbon system", *Scripta Materialia* **34** (6), 841-846 (1996).

[57] E. Rocha-Rangel, P. F. Becher, and E. Lara-Curzio, "Reactive-Wetting of Alumina by Molten Aluminum Alloys", presented at the *Proceedings to the International Conference for Advanced Structural Materials Symposium 2003*, Cancun Quintana Roo, Mexico, (Trans Tech Publications Ltd, 2003).

[58] Y. V. Naidich, Y. N. Chubashov, N. F. Ishchuk, and V. P. Krasovskii, "Wetting of some Nonmetallic Materials by Aluminum", *Soviet Powder Metallurgy and Metal Ceramics (English translation of Poroshkovaya Metallurgiya)* **22** (6), 481-483 (1983).

[59] D. J. Wang and S. T. Wu, "The Influence of Oxidation on the Wettability of Aluminum on Sapphire", *Acta Metallurgica et Materialia* **42** (12), 4029-4034 (1994).

[60] H.-N. Ho and S.-T. Wu, "Influences of Temperature and Residual Gas on the Wettability of Aluminum Melt on Sapphire", *Japanese Journal of Applied Physics, Part 1: Regular Papers & Short Notes & Review Papers* **37** (1), 274-278 (1998).

[61] P. Shen, H. Fujii, T. Matsumoto, and K. Nogi, "Wetting of (0001) $\alpha$-$Al_2O_3$ single crystals by molten Al", *Scripta Materialia* **48** (6), 779-784 (2003).

[62] J. G. Li, D. Chatain, L. Coudurier, and N. Eustathopoulos, "Wettability of sapphire by Sn-Al alloys", *Journal of Materials Science Letters* **7** (9), 961-963 (1988).

[63] J. G. Li, L. Coudurier, and N. Eustathopoulos, "Work of Adhesion and Contact-Angle Isotherm of Binary Alloys on Ionocovalent oxides", *Journal of Materials Science* **24** (3), 1109-1116 (1989).

[64] N. K. Adam and H. K. Livingston, "Contact Angles and Work of Adhesion", *Nature* **182** (4628), 128-128 (1958).

[65] G. Levi and W. D. Kaplan, "Oxygen Induced Interfacial Phenomena during Wetting of Alumina by Liquid Aluminium", *Acta Materialia* **50** (1), 75-88 (2002).



[66] G. Levi, W. D. Kaplan, and R. E. Loehman, "Iron as an Oxygen Tracer at the Aluminum-Alumina Interface", *Journal of the American Ceramic Society* **85** (6), 1601-1606 (2002).

[67] V. Ghetta and D. Chatain, "Morphologies Adopted by $Al_2O_3$ Single-Crystal Surfaces in Contact with Cu Droplets", *Journal of the American Ceramic Society* **85** (4), 961-964 (2002).

[68] G. Levi and W. D. Kaplan, "Aluminium-Alumina Interface Morphology and Thermodynamics from Dewetting Experiments", *Acta Materialia* **51** (10), 2793-2802 (2003).

[69] C. Scheu, W. Stein, and M. Ruhle, "Electron Energy-Loss Near-Edge Structure Studies of a Cu/(11-20)$\alpha$-$Al_2O_3$ Interface", *Physica Status Solidi B-Basic Research* **222** (1), 199-211 (2000).

[70] N. Eustathopoulos and B. Drevet, "Determination of the Nature of Metal-Oxide Interfacial Interactions from Sessile Drop Data", *Materials Science and Engineering a-Structural Materials Properties Microstructure and Processing* **249** (1-2), 176-183 (1998).

[71] Y. V. Naidich, in *Progress in Surface and Membrane Science*, edited by D.A. Cadenhead and J.F. Danielli (Academic Press, New York, 1981), Vol. 14, pp. 353-484.

[72] D. Chatain, I. Rivollet, and N. Eustathopoulos, "Thermodynamic Adhesion in Nonreaactive Liquid Metal-Alumina Systems", *Journal de Chimie Physique et de Physico-Chimie Biologique* **83** (9), 561-567 (1986).

[73] C. Scheu, W. Stein, S. Klein, T. Wagner, A. P. Tomsia, and M. Ruhle, "Microstructure and Modifications of Cu/$Al_2O_3$ Interfaces", *Zeitschrift für Metallkunde/Materials Research and Advanced Techniques* **92** (7), 707-711 (2001).

[74] V. Laurent, D. Chatain, and N. Eustathopoulos, "Wettability of SiC by Aluminium and Al-Si Alloys", *Journal of Materials Science* **22** (1), 244-250 (1987).

[75] V. Laurent, C. Rado, and N. Eustathopoulos, "Wetting Kinetics and Bonding of Al and Al Alloys on $\alpha$-SiC", *Materials Science & Engineering A: Structural Materials: Properties, Microstructure and Processing* **A205** (1-2), 1-8 (1996).

[76] C. Rado, B. Drevet, and N. Eustathopoulos, "The role of compound formation in reactive wetting: the Cu/SiC system", *Acta Materialia* **48** (18-19), 4483-4491 (2000).

[77] E. Saiz, A. P. Tomsia, and R. M. Cannon, "Ridging Effects on Wetting and Spreading of Liquids on Solids", *Acta Materialia* **46** (7), 2349-2361 (1998).

[78] J. J. Bikerman, "Use of Hysteresis of Wetting for Measuring Surface Tension", *Journal of Physical Chemistry* **62** (12), 1534-1536 (1959).

[79] G. R. Lester, "Contact angles of liquids at deformable solid surfaces", *Journal of Colloid Science* **16** (4), 315-326 (1961).

[80] Y. Liu and R. M. German, "Contact angle and solid-liquid-vapor equilibrium", *Acta Materialia* **44** (4), 1657-1663 (1996).

[81] E. Saiz, R. M. Cannon, and A. P. Tomsia, "Energetics and Atomic Transport at Liquid Metal/$Al_2O_3$ Interfaces", *Acta Materialia* **47** (15-16), 4209-4220 (1999).

[82] S. W. Ip, Y. Wang, and J. M. Toguri, "Aluminum foam stabilization by solid particles", *Canadian Metallurgical Quarterly* **38** (1), 81-92 (1999).

[83] T. N. Hunter, R. J. Pugh, G. V. Franks, and G. J. Jameson, "The role of particles in stabilising foams and emulsions", *Advances in Colloid and Interface Science* **137** (2), 57-81 (2008).

[84] T. V. Subrahmanyam and E. Forssberg, "Froth Stability, Particle Entrainment and Drainage in Flotation - A Review", *International Journal of Mineral Processing* **23** (1-2), 33-53 (1988).

[85] H. Stanzick, M. Wichmann, J. Weise, L. Helfen, T. Baumbach, and J. Banhart, "Process control in aluminum foam production using real-time X-ray radioscopy", *Advanced Engineering Materials* **4** (10), 814-823 (2002).

[86] N. Babcsán, D. Leitlmeier, and H. P. Degischer, "Foamability of Particle Reinforced Aluminum Melt", *Materialwissenschaft und Werkstofftechnik* **34** (1), 22-29 (2003).

[87] K. Kadoi, M. Tayama, M. Yoshida, and H. Nakae, "Influence of Viscosity on Foamability of Aluminum Melts", presented at the *MetFoam 2005 - 4th International Conference on Porous Metals and Metal Foaming Technology*, Kyoto, Japan, (The Japan Institute of Metals, 2005).

[88] L. Q. Ma and Z. L. Song, "Cellular structure control of aluminium foams during foaming process of aluminium melt", *Scripta Materialia* **39** (11), 1523-1528 (1998).

[89] R. Minto and W. G. Davenport, "Entrapment and Flotation of Matte in Molten Slags", *Canadian Mining and Metallurgical Bulletin* **65** (720), 70-76 (1972).

[90] H. Nakae and K. Kota, "Processing Fundamentals of Fine Aluminum Foam Production from Liquid Metals", presented at the *International Conference on Porous Metals and Metal Foaming Technology - MetFoam 2005*, Kyoto (Japan), (Japan Institute of Metals, 2005).



[91] in *ASM International Handbook Committee* (ASM International, Materials Park (USA), 1998), Vol. 2: *Properties and Selection: Nonferrous Alloys and Special-Purpose Materials*.

[92] G. W. H. Höhne, W. F. Hemminger, and H. J. Flammersheim, *Differential Scanning Calorimetry*, 2nd rev. ed. (Springer, Berlin (Germany), 2003).

[93] J. Banhart, "Metal Foams - Production and Stability", *Advanced Engineering Materials* **8** (9), 781-794 (2006).

[94] C. J. Yu, H. H. Eifert, J. Banhart, and J. Baumeister, "Metal Foaming by a Powder Metallurgy Method: Production, Properties and Applications", *Materials Research Innovations* **2** (3), 181-188 (1998).

[95] C. W. Bale et al., "FactSage thermochemical software and databases", *Calphad: Computer Coupling of Phase Diagrams and Thermochemistry* **26** (2), 189-228 (2002).

[96] C. W. Bale, A. D. Pelton, and W. T. Thompson, *FactSage 5.5* (2007).

[97] C. J. Smithells, *Smithells Metals Reference Book*. (Butterworth-Heinemann, 2004).

[98] P. Shen, H. Fujii, T. Matsumoto, and K. Nogi, "Critical Factors Affecting the Wettability of α-Alumina by Molten Aluminum", *Journal of the American Ceramic Society* **87** (11), 2151-2159 (2004).

[99] A. W. Adamson and A. P. Gast, *Physical Chemistry of Surfaces*, 6th ed. (John Wiley & Sons, New York (USA), 1997).

[100] J. C. Anderson, K. D. Leaver, R. D. Rawlings, and J. M. Alexander, *Materials Science*, 3rd ed. (Van Nostrand Reinhold, Wokingham (UK), 1985).

[101] G. Gottstein, *Physical Foundations of Materials*. (Springer-Verlag, Berlin (Germany), 2004).

[102] P. Shen, H. Fujii, and K. Nogi, "Effect of Substrate Surface Orientation on the Wettability and Adhesion of α-$Al_2O_3$ Single Crystals by Molten Cu", *Journal of Materials Research* **20** (4), 940-951 (2005).

[103] G. Lang, "Casting Properties and Surface Tension of Aluminum and Binary Aluminum Alloys - 3", *Aluminium* **49** (3), 231-238 (1973).

[104] G. Lang, "Effect of Addition Elements on the Surface Tension of Liquid Very High Purity Aluminum", *Aluminium* **50** (11), 731-734 (1974).

[105] T. Iida and R. I. L. Guthrie, *The Physical Properties of Liquid Metals*. (Oxford University Press, New York (USA), 1988).

[106] D. R. Gaskell, *Introduction to the thermodynamics of materials*, 4th ed. (Taylor and Francis, New York (USA), 2003).

[107] A. M. M. Gadalla and J. White, "Equilibrium relationships in the system CuO-$Cu_2O$-$Al_2O_3$", *Transactions of the British Ceramic Society* **63** (1964).

[108] C. D. Wagner, A. V. Naumkin, A. Kraut-Vass, J. W. Allison, C. J. Powell, and J. John R. Rumble, "*NIST X-ray Photoelectron Spectroscopy Database*", Measurement Services Division of the National Institute of Standards and Technology (NIST), August 12th, 2008, http://srdata.nist.gov/xps/Default.aspx

[109] A. C. Ferro and B. Derby, "Wetting Behaviour in the Al-Si/SiC System: Interface Reactions and Solubility Effects", *Acta Metallurgica et Materialia* **43** (8), 3061-3073 (1995).

[110] J. Goicoechea, C. Garcia-Cordovilla, E. Louis, and A. Pamies, "Wetting and reactivity of SiC particulates with liquid aluminium alloys", presented at the *Proceedings to the Symposium A4 on Composite Materials of the International Conference on Advanced Materials, Strasbourg (France)*, (Elsevier Science Publishers B.V., Amsterdam (Netherlands), 1992).

[111] S. Esmaeelzadeh, A. Simchi, and D. Lehmhus, "Effect of ceramic particle addition on the foaming behavior, cell structure and mechanical properties of P/M AlSi7 foam", *Materials Science and Engineering: A* **424** (1-2), 290-299 (2006).

[112] M. Haesche, J. Weise, F. Garcia-Moreno, and J. Banhart, "Influence of particle additions on the foaming behaviour of AlSi11/$TiH_2$ composites made by semi-solid processing", *Materials Science and Engineering: A* **480** (1-2), 283-288 (2008).

[113] J. Banhart, "Metal Foams – The Mystery of Stabilisation", presented at the *MetFoam 2005 - 4th International Conference on Porous Metals and Metal Foaming Technology*, Kyoto, Japan, (The Japan Institute of Metals, 2005).

# APPENDICES

## APPENDIX A: WETTING FURNACE

The equipment employed for the wetting experiments is schematically depicted in Figures 9.1 and 9.2. It follows the theoretical suggestion of *NAIDICH*[58], however with one important modification: Instead of the suggested vertical setup, which requires some sort of box furnace arrangement, a horizontal setup is chosen utilizing a tube furnace. Reason for this is that due to the smaller furnace volume and smaller surface area that needs to be sealed, a tube furnace generally reaches higher vacuum than a box furnace arrangement. The chosen tube furnace setup consists of a mullite

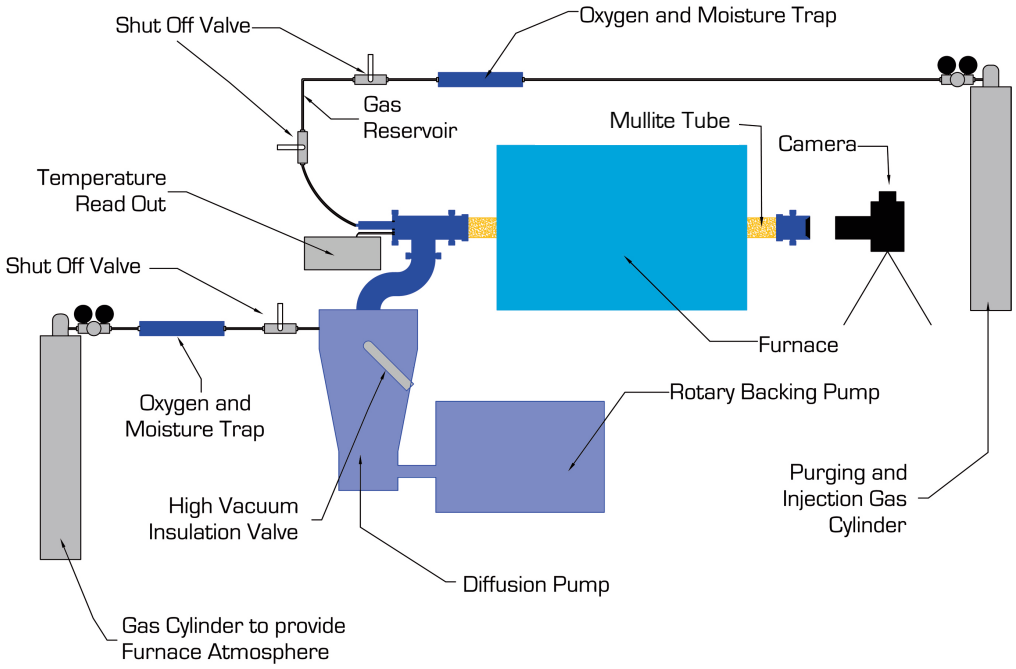


Figure 0.1: Schematic of the overall setup for the wetting experiments (not to scale)

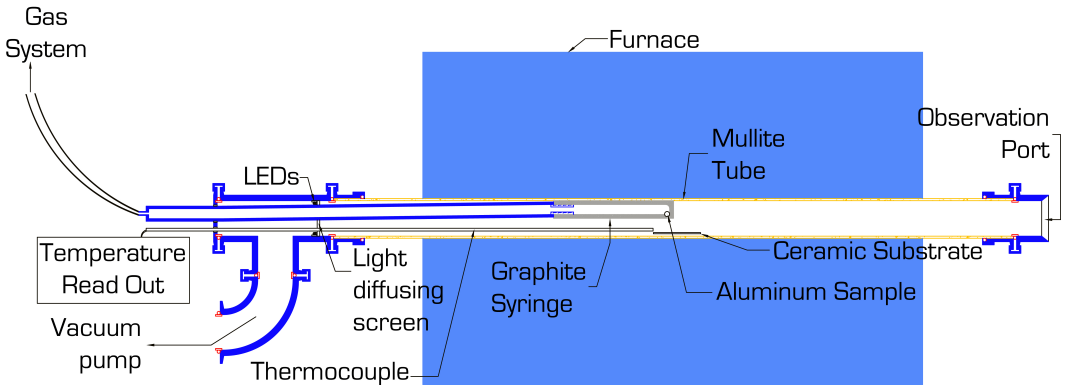


Figure 0.2: Schematic drawing of a section through the vacuum tube furnace

tube of 50mm outer diameter, 45mm inner diameter, two gas systems, a powerful vacuum pump system, and an LED background light source, to allow low temperature experiments, that do not provide enough brightness due to thermal radiation in the visible spectrum (i.e. below 700°C). The furnace is a *LINDBERG* model 54233 with 8 silicon carbide heating-elements, featuring a programmable *EUROTHERM* temperature control (model 2416). The two gas systems are designed to allow for experiments under gas atmosphere as well as under vacuum.

The vacuum pump system consists of a diffusion pump (model Diffstak 100/300) and a rotary backing pump (model RV5). The pressure inside the furnace system is measured by an active wide range gauge (model WRG-SL-NW25) and displayed by an active gauge controller (model RS232, 3 Head); the system features an additional active Pirani gauge (model APG-M-NW25) which measures the backing pressure. All vacuum pump parts and gauges were purchased from *BOC EDWARDS*.

Inside the mullite tube, a 22mm $(\frac{7}{8}")$ outer diameter, 13mm $(\frac{1}{2}")$ inner diameter graphite syringe manufactured by *GRAPHITESTORE* is placed horizontally. It is connected to the purging and injection gas system. The syringe has a recess around an orifice of 1.5mm diameter, drilled through the wall. The syringe is oriented so that the orifice is directed vertically approximately 18mm above the substrate (Figure 9.3).

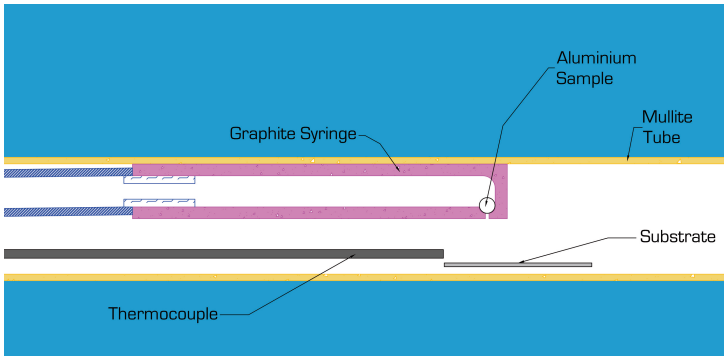


Figure 0.3: Schematic of the graphite syringe inside the tube

Possible leaks on the vacuum pump side of the tube will not result in oxygen passing by the substrate, as it would be evacuated directly into the pump. Since the active wide range gauge in the vacuum system, located close to the diffusion pump, can be damaged by particles being sucked into the diffusion pump, titanium sponge granules were placed only between the observation port and the substrate, not between the hot-zone and the end of the tube that is connected to the pump system.

The experimental temperature is controlled using a K-type thermocouple located between the syringe and the substrate; the thermometer is an *OMEGA* HH506R.

In both gas systems, the oxygen partial pressure of the inert gas is reduced by passing the gas through an oxygen and moisture trap. In the purging and injection gas line two shut-off valves represent the two sides of a 1.9cm$^3$ gas reservoir. After the reservoir, the purging and injection gas line connects to a stainless steel pipe, which feeds into the vacuum tube furnace and connects to the graphite syringe.

For the experiments under vacuum, a gas reservoir pressure of 70mbar above atmospheric pressure will force the molten and roughly spherical aluminum (alloy) particle through the orifice in the syringe without splattering. If experiments need to be run under inert gas atmosphere, the furnace pressure can be set to 1200mbar, the gas reservoir is then pressurized to approximately 1bar above atmospheric pressure.

## APPENDIX B: FOAMING FURNACE – EXPANDOMETER

Main feature of the expandometer (Figure 9.4) is a vertical tube furnace, in which a slightly tapered nickel super alloy crucible hangs. The bottom diameter of the crucible is with 31mm slightly larger than the 30mm compacts used for foaming. This was chosen to facilitate sample placement. A K-type thermocouple touches the outside of the crucible wall just above its bottom, and records and controls the foaming temperature. The furnace control is a *WATLOW* SD 31. In order to prevent the foams from adhering to the crucible walls or the plunger, both were coated with a thin layer of boron nitride.

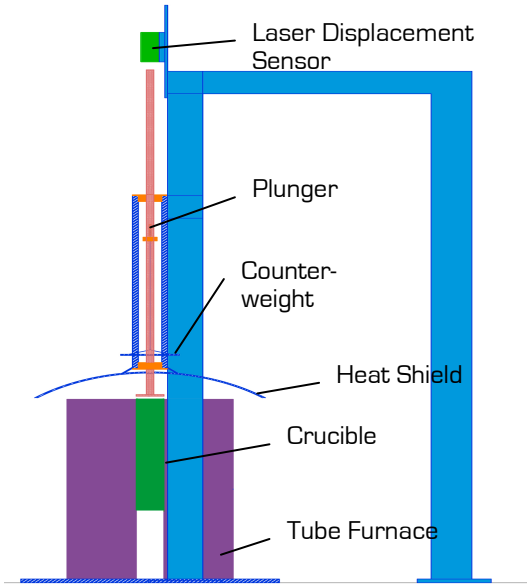


Figure 0.4: Schematic of the expandometer used for foaming experiments.

As the compact starts expanding, the volume growth is almost exclusively constrained to vertical growth. The plunger, which is counterweighed to approximately 96% (ratio of counterweight to weight of plunger), relays the unidirectional growth. The laser displacement sensor at the top of the setup (*WENGLOR* CP24MHT24) measures the distance the plunger travels and an *OMEGA* data acquisition system (model OMB-DAQ-54) records the values at 1Hz. From these measurements, the volume growth can be calculated, correcting for the tapered crucible. The setup featuring the plunger results in a less noisy signal from the displacement sensor, it prevents the typical dome formation at the top of the foam, and enables the system to measure foam collapse. A heat shield over top of the tube furnace and the crucible maintains the furnace temperature more stable and protects the displacement sensor and the plunger's counterweight system from thermal damage.